STUDY OF RELAXATION PHENOMENON AND FUNCTIONAL PROPERTIES IN SOME FERROMAGNETIC SHAPE MEMORY ALLOYS

Thesis submitted for the degree of

Doctor of Philosophy (Science)

in

Physics (Experimental)

by

Sandeep Agarwal

Department of Physics

University of Calcutta

September 2014

To my family

Acknowledgment

The works present here were mostly carried out in the Laboratory for Condensed Matter Physics at S. N. Bose National Centre for Basic Sciences, with financial support in the form of JRF/SRF from the Council of Scientific & Industrial Research, India.

First of all I owe my deepest gratitude to my supervisor Prof. Pratip Kr. Mukhopadhyay for giving me the chance to work in this interesting field of magnetic shape memory alloys and start my thesis work. His constant emphasis on developing system with more robust properties helped me. He helped me with his expert advice and unparalleled guidance from the initial stage of this research. He gave me enough freedom in thinking and choosing my own problems during my research carrier. I am highly obliged to him for his constructive criticism and valuable suggestions, which helped me to present the scientific results in an efficient and effective manner in this thesis.

I sincerely acknowledge Prof. Subham Majumdar from Indian Association for the Cultivation of Science, India, for helpful discussion in the beginning of my Ph.D. and providing us with the samples for measurement. I am thankful to Dr. Dipankar Das and Dr. Souvik Chatterjee from UGC DAE Consortium for Scientific Research, Kolkata, India, for helping us with the SQUID and magnetoresistance measurement. I am also thankful to Prof. Sangam Banerjee of Saha Institute of Nuclear Physics for his valuable insight and help with SQUID measurement. I am thankful to Prof. Subodh Kumar De, from Indian Association for the Cultivation of Science, India and Dr. Amitava Mitra from National Metallurgical Laboratory, India for their valuable suggestions. I am thankful to Prof. Lluís Mañosa and his group at University of Barcelona, Spain for help with calorimetric measurements.

I would like to thank S.N. Bose center for providing the research fellowship during my period of extension and facilities without which it was impossible for me to carry my research. I would like to thank Department of Science and Technology (DST) for providing me financial support during my visit to International Conference of Ferromagnetic Shape Memory Alloys (ICFSMA 2013), in Boise, USA.

I must also thank friends form SNB especially Manotosh and Rajib (*Gadrinath*) for their constant help with instrumentation and programming with labVIEW. I was lucky to have friend like Sandeep Singh who was working on similar materials and his understanding of the system helped me a lot and I am also thankful to him for helping me with Rietveld Analysis. I would like to thank my group-mates (Arun, Syamanta, Tanmoy Ghosh (TG), Injamamul and Dr. BRK) for their support. I am also thankful to my friends Mayukh and Kousik of Saha Institute of Nuclear Physics for helping me with measurement.

I will always be indebted to my friend and seniors Jena, Bipul da, Debraj, Kapil, Prashant and Abhinav (& Arka) and batch mates Abhijit, Debmalya, Tanmoy (TP), Rajiv (CB), Garain, Rishi and Tamal for making my nonacademic life so happening at SNB. I would also like to thank Wasim, Rajshree, Tamisra, Anuradha, Saikat, Basu, Sishir, Soma and Arup for making my stay at center memorable.

I would like to take this opportunity to recall few of my college friends Mukesh (and his MM), Deepak, Chintu, Debarghya, Debasis, Suvankar, Saikat, Piyali and Prajnamita who were always there with me, when I needed them. I would also like to specially thank TG without whom these thesis would not have been possible, who has tolerated constant poking, criticisms and did extra work (though sometimes unwillingly) that I gave him.

Finally my sincerest thanks to my parents, grandparents and my brothers Navin and Abhishek without whom this thesis could never been possible.

Sandeep Agarwal

List of publications

1. **The effect of Al replacement and heat treatment on magnetocaloric properties of Ni_2Mn-Sn ferromagnetic shape memory alloys**
   Sandeep Agarwal and P. K. Mukhopadhyay,
   J. Alloys Compd., **608**, 329(2014)
2. **Crossover of spin glass characteristics as a function of field in an NiMnSnAl alloy**
   Sandeep Agarwal, S. Banerjee and P. K. Mukhopadhyay,
   J. Appl. Phys., **114**, 133904 (2013)
3. **Role of replacement of Sb with Al in the phase transformation of Ni-Mn-Sb alloys**
   Sandeep Agarwal, and P. K. Mukhopadhyay,
   AIP Conference Proceedings, **1536**, 977 (2013).
4. **Effect of low temperature annealing on magneto-caloric effect and spin glass behavior of Ni-Mn-Sn-Al ferromagnetic shape memory alloy**
   Sandeep Agarwal and P. K. Mukhopadhyay,
   Submitted for Publication.
5. **Effect of Sn and Sb element on the magnetism and functional properties of NiMnAl ferromagnetic shape memory alloys**
   Sandeep Agarwal and P. K. Mukhopadhyay,
   Under preparation.
6. **Large conventional magnetocaloric effect in the vicinity of martensitic transformation in NiMnSbAl systems**
   Sandeep Agarwal and P. K. Mukhopadhyay,
   Under preparation.
7. **†Frequency dependent susceptibility study for a ferromagnetic shape memory alloy**
   P. K. Mukhopadhyay, B. Rajini Kanth, and Sandeep Agarwal,
   Bulletin of the American Physical Society, 55 (2010).
8. **†Magnetic properties and magnetocaloric effect in Pt doped Ni-Mn-Ga**
   Sanjay Singh, S. W. D’Souza1, K. Mukherjee, P. Kushwaha, S. R. Barman, Sandeep Agarwal, P. K. Mukhopadhyay, Aparna Chakrabarti and E. V. Sampathkumaran
   Appl. Phys. Lett., **104**, 231909 (2014).

† Not used in present thesis

List of Abbreviations

SMA	Shape memory alloy
MT	Martensitic transition
M_S, M_F, A_S, A_F	Martensitic start, Martensitic finish, Austenitic start and Austenitic finish temperatures
FSMA	Ferromagnetic shape memory alloys
e/a	Valence electron concentration per atom
FM	Ferromagnetic
RKKY	Ruderman-Kittel-Kasuya-Yoshida
AFM	Antiferromagnetic
T_C	Curie temperature
M (T)	Temperature dependent magnetization measurement
MCE	Magnetocaloric effect
MR	Magnetoresistance
EDAX	energy dispersive x-ray analysis
XRD	X-ray diffraction
DSC	differential scanning calorimetric
SEM	Scanning electron microscope
H	Magnetic field
M	Magnetization
$\chi^{/}$	Real part of liner ac susceptibility
$\chi^{//}$	Imaginary part of liner ac susceptibility
GPIB	General Purpose Interface Bus
VSM	Vibrating sample magnetometer
SQUID	Superconducting quantum interference device
ZFC	Zero-field-cooled
FC	Field-cooled
FH	Field- heated
M-H	Magnetic isothermal curves

EB	Exchange bias
ΔS_M	Magnetic entropy change
ΔM	Change in magnetization
RC	Refrigerant capacity
T_N	Neel temperature
χ_3	Third harmonic of ac susceptibility (magnitude)
T_f	Freezing temperature
(H, T)	Magnetic field temperature phase diagram

Table of Content

Chapter 1

Introduction

In this chapter we introduce the topic to the reader and give the motivation for the work undertaken in the thesis. We provide a literature survey for the background.

1.1 Overview

The advancement in science and technology and better understanding of material behavior have enabled development of materials which apart from displaying usual properties (mechanical, thermal, electrical etc.) also show additional functional capabilities (sensing, actuation, electromagnetic shielding etc.). These are called multifunctional materials. A specialized subgroup of these materials exhibiting sensing and actuation capabilities are known as active materials. They can be used for sensing purpose (e.g. thermal, mechanical, magnetic, optical input →voltage output) or as actuator (e.g. thermal, electrical, magnetic, optical input → mechanical output). Some examples of active materials include piezoelectric and electrostrictives (coupling of mechanical with electric fields), piezomagnetics and magnetostrictives (coupling of mechanical with magnetic fields), and shape memory materials (coupling of thermal with mechanical fields). In these materials the external field directly couples to the actuation like in piezoceramics, piezoelectric polymers, magnetostrictive ceramics, shape memory alloys and magnetic shape memory alloys. Faster response time and enhanced actuation stress are the main advantages of these active materials.

1.2 Shape memory effect

Shape Memory Alloys (SMA) is a class of shape memory materials with the ability to recover their shape reversibly when the temperature is increased. An increase in temperature can result in shape recovery even under high applied loads therefore resulting in high actuation energy densities. SMA’s develop the largest strains of the actuator materials available till date and thus these materials have been in the forefront of research ever since their discovery [1]. These materials have been adapted into wide variety of industrial sectors such as aerospace, naval, automotive, biomedical, etc. [2,3]. The irreversible martensitic transformation was first observed back in 1890s by Adolf Martens in Fe-C system. The shape memory effect which occurs as the result of thermally induced reversible transformation of martensite was first observed in 1949 in CuZn and CuAl alloys [2]. A first-order diffusionless structural phase transition from the high temperature austenite phase to the low temperature martensite phase, known as martensitic transition (MT) which occurs via shear lattice distortion, plays the key role in the shape memory effect.

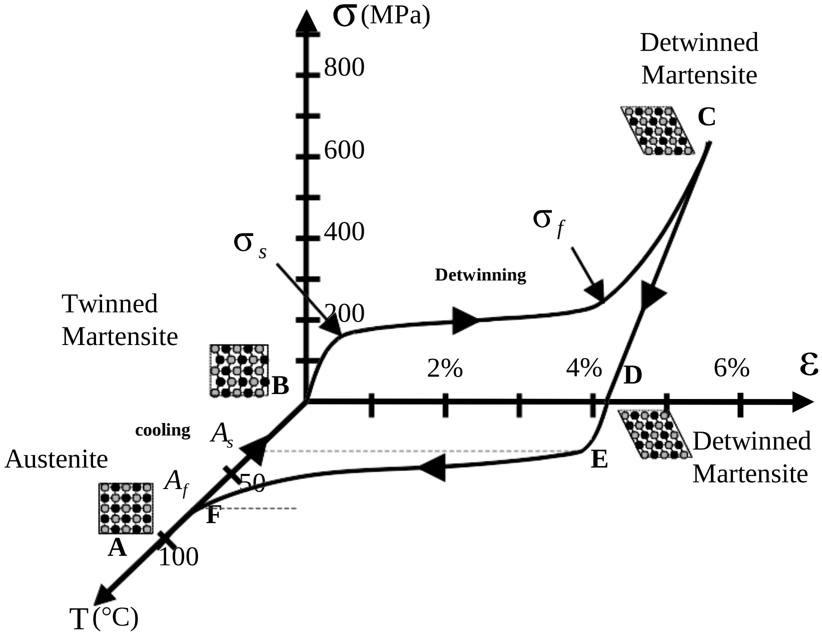

Figure 1.1 Stress-strain-temperature data exhibiting the shape memory effect for a typical NiTi SMA [3].

As the sample is cooled during the forward transformation, austenite or the parent phase with higher symmetry begins to transform to lower symmetric twinned martensite at the martensitic start temperature (M_S) and completes transformation at the martensitic finish temperature (M_F). During heating, the reverse transformation initiates at the austenitic start temperature (A_S) and completed at the austenitic finish temperature (A_F). The crystal in martensitic phase has lower symmetry and is thus degenerate, which results in a certain number of structures which are energetically equivalent but with different crystallographic orientations: these are called variants. These martensitic variants can exist either as a twinned martensite, which is formed by a combination of self-accommodated martensitic variants to minimize the elastic energy, or as a detwinned or reoriented martensite in which a specific variant is dominant. Detwinning can be induced by applying stress; the minimum stress required for detwinning initiation is termed as the detwinning start stress (σ_s) and at sufficiently high stress which results in complete detwinning of martensite is called the detwinning finish stress (σ_f). The detwinning results in macroscopic shape change. Reheating the material will result in transformation back to parent phase and shape recovery even while the load is still applied. The schematic described above has been shown in the Figure 1.1 (figure has been taken form Ref [3]).

The transformation to martensitic phase can also be induced by applying sufficient external stress at a temperature above A_F. The external stress result in formation of fully detwinned martensite created from austenite and complete shape recovery is observed upon unloading to austenite. This effect is known as superelasticity.

1.3 Ferromagnetic shape memory alloy

The discovery of the magnetic shape memory alloys, often referred to as ferromagnetic shape memory alloys (FSMA), has further increased interest in these class of alloys as their shape memory properties can be controlled by magnetic field apart from the thermal and stress control [4,5]. The shape memory effect occurs due to detwinning of martensitic variants by applied stress, which is controlled thermally thus actuation frequency is limited due to rate of heat transfer. In FSMA actuation is achieved additionally by magnetic field thus working frequency is much higher [6].

There exist strong coupling between mechanical and magnetic properties of FSMA, which makes them important in applications like sensors and actuators. The most widely investigated magnetic shape memory materials have been Ni-Mn-Z (where Z = Al, Ga, In, Sn and Sb). Several other types of FSMA has been studied which include Co-Ni-Al [7], Fe-Pt [8], Co-Ni-Ga [9] and Ni-Fe-Ga [10]. These alloys other than Ni-Mn-Z (except for Z= Al) systems exhibit lower functionality as compared to Ni-Mn-Z system but have higher ductility and mechanical properties. However work presented here is focused on Ni-Mn-Z system. We will discuss various properties of FSMA system based on this system.

1.3.1 Magnetic shape memory effect

In FSMA the twin variants have preferred directions of magnetization below the Curie temperature [4,5]. When a magnetic field is applied and if the magnetic anisotropic energy is less than the energy required to move a twin boundary then magnetization within each variant changes and no shape change is observed as shown in the Figure 1.2. However if the magnetic anisotropy is high and the energy required to move twin boundaries is low enough, there will be a rotation of the structural domains in such a way that their easy axes get aligned along the externally applied field. In this case, the rotation of martensitic variants is promoted by the difference in the Zeeman energy between the variants, and thus results in a significant macroscopic shape change as shown in the Figure 1.2 and shape can be recovered once the field is removed [11–13].

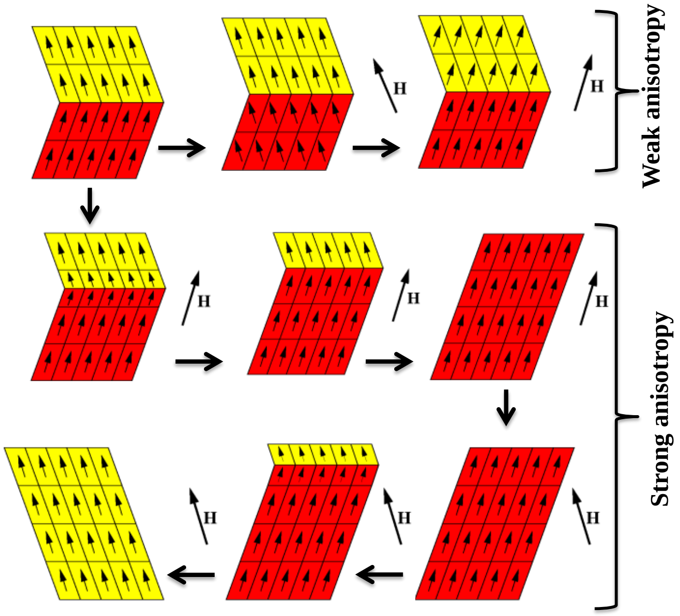

Figure 1.2 Rearrangement of the martensite variants in the magnetic field (H) when magnetocrystalline anisotropy is weak and when it is strong. Favorably oriented variants grow at the expense of unfavorably oriented variants to align the magnetization along applied H [12].

The recovery of shape change upon removal of magnetic field is not complete and it is reversible only for small strain [14,15]. The occurrence of detwinning under applied magnetic field was observed using various experimental techniques [15,16]. The magnetic field induced recoverable strain as high as 10 % has been achieved in FSMA which is two orders of magnitude larger than the magnetic-field-induced strains observed in ordinary magnetostrictive materials, such as Terfenol-D [14]. As actuation in FSMA is driven by the magnetic-field-induced reorientation of martensitic variants, it has much higher operating frequency compared to SMA, but they suffer from low blocking stress level above which magnetic-field-induced strains are completely suppressed [17].

In FSMA a strong coupling exists between the structure and magnetic moments, which modifies the relative stability of austenitic and martensitic phases. The application of field stabilizes phases having higher magnetism. This lead to dependence of MT temperature on the applied field and depending on the whether the martensitic has higher or lower magnetization than the austenitic phase, either the forward or the reverse MT is promoted by application of field. This condition is expressed by Clausius-Clapeyron equation. This leads to magnetic superelasticity in FSMA where large strain is achieved by applying magnetic field that induces MT and on removal of field reverse transition takes place with recovery of strain. Similarly reverse magnetic superelasticity is also observed when field induces austenitic transformation, this is more commonly known as metamagnetic shape memory [18]. The metamagnetic behavior is found in several Ni-Mn-Z alloys, while the Ni-Mn-Ga system shows magnetic superelasticity [19]. The Ni-Mn-In [15] and Ni-Mn-Sn [20] system generally shows metamagnetic shape memory.

1.3.2 Structure of Ni-Mn based alloy

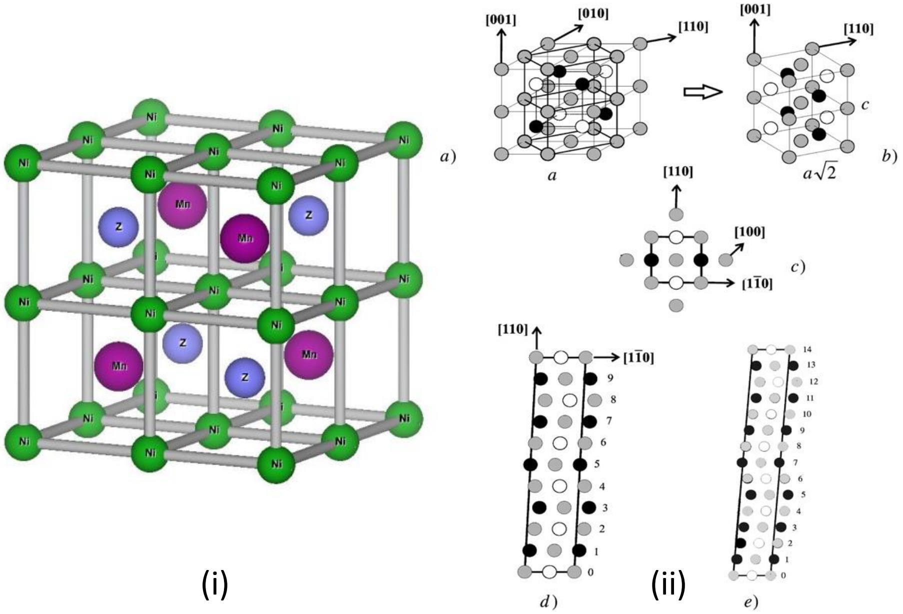

Figure 1.3 (i) The L2 structure for Ni_2MnZ in austenitic phase. (ii) Austenite and martensite structures in case of Ni_2MnGa. Grey: Ni, black: Mn, B white: Z. (a) The $L2_1$ structure showing the relationship with the tetragonal unit cell which is also shown in part (b). (c) The tetragonal unit cell viewed from the top and (d) the 5M (or 10M) and (e) 7M (or 14M) modulated structures obtained by shearing the tetragonal cell [15].

The alloy system we investigated belongs to family of full Heusler alloy. We will refer to it as Heusler alloy further on. Thus we have given a brief overview of crystal structure of the Heusler alloy. In stoichiometric composition Heusler alloys have the general formula X_2YZ, here X (Ni) and Y (Mn) are transition metal elements and Z (Al, Ga, In, Sn and Sb) is an s-p group element. The austenitic phase is in general higher symmetric phase with $L2_1$ structure having space group *Fm-3m*. This structure has four interpenetrating face centered cubic (fcc) sub-lattices. The sub-lattices with Wyckoff coordinates (0, 0, 0) and (1/2, 1/2, 1/2) are occupied by X atoms, while the sub-lattices with coordinates (1/4, 1/4, 1/4) and (3/4, 3/4, 3/4) are occupied by the Y and Z atoms, respectively. The $L2_1$ cell for Ni_2MnZ is shown in Figure 1.3 (i). When the positions (1/4, 1/4, 1/4) and (3/4, 3/4, 3/4) are randomly occupied by Y and Z the system reduces to B2 type structure and when X, Y and Z atoms occupy all the coordinates randomly then the system is reduced to A2 type.

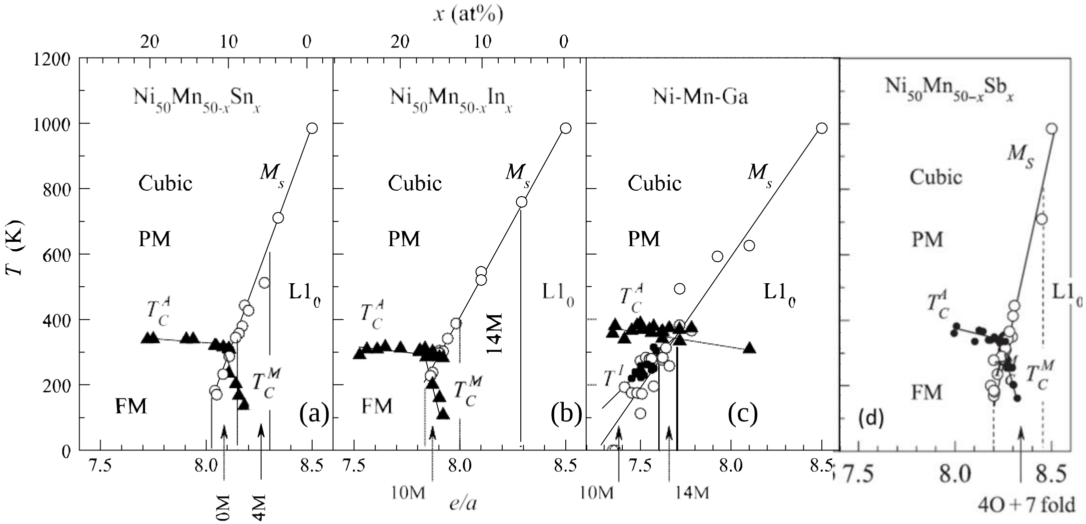

Figure 1.4 The magnetostructural phase diagram of Ni–Mn–Z Heusler alloys with Z as (a) Sn, (b) In, (c) Ga and (d) as Sb. The triangles and the circles correspond to the magnetic and martensitic transformation temperatures respectively. The regions corresponding to the different structures are separated by discontinuous lines. Small solid circles in (c) correspond to the premartensitic transition temperature [15,24].

When temperature is reduced the system undergoes MT to lower symmetric martensitic phase and acquires a number of structures. In general the Ni-Mn-Z system crystallizes in martensitic phase into tetragonal, orthorhombic and monoclinic or into their modulated phases like modulated tetragonal etc. [21–23]. For lower concentration of Z it transforms to the $L1_0$ tetragonal structure, which also happens to be its ground state structure for its parent compound Ni_2Mn_2. Modulated structures are found at higher concentration of Z and are commonly in 5M or 7M modulations. Martensitic structure in general is formed by the diffusionless tetragonal distortion of initial cubic lattice as shown in the Figure 1.3 (ii a) and the tetragonal structure is shown separately in Figure 1.3 (ii b) (part of Figure 1.3 was taken from [15]). From the X-ray it was further confirmed that the martensitic has monoclinic unit cell constructed of several layers of atomic planes along a particular direction. M refers to the modulation and the number refers to the periodicity of shuffling. Examples of 5M (or 10 M) and 7 M (or 14 M) are shown in the Figure 1.3 (ii d) and (ii e), unit cell is viewed form the top.

While the Ni-Mn-Ga system undergoes MT in stoichiometric composition, the systems with Z = Al, In, Sn, and Sb undergo MT at off-stoichiometric compositions depending on the Z atom. In the Figure 1.4 (extracted from Refs. [15,24]) we see the evolution of various martensitic structures and there dependence on the concentration and valence electron concentration per atom e/a. The data for Z as Sn, Sb and In are for $Ni_{50}Mn_{50-x}Z_x$ whereas in Ga system it was taken for all possible compositions. We see that in all the samples at low e/a, system is in 10 M structure and transforms to 14 M to $L1_0$ at higher concentrations for Z = Ga, In and Sn. For Ni-Mn-Sb system we observe that structure changes to mixture of 4O (four fold orthorhombic) and 7 fold orthorhombic at lower e/a and becomes $L1_0$ at higher e/a. 10M modulated phase has also been observed in certain compositions of Sb based alloys instead of 4O [25]. It is also seen that presence of various Z elements affects the width of the various modulated structure. Thus e/a ratio and Z element both play important roles in determining the structure of Ni-Mn-based alloys.

1.3.3 Magnetism in Ni-Mn based alloys

The magnetism in the Ni-Mn-Z system and coupling of it to the martensitic transformation play a key role in properties of these alloys. In austenitic phase the system is predominantly in the ferromagnetic (FM) state. The magnetism in the system is believed to come from the Mn atoms as in case of most of Mn based system [26]. The moment of Mn is close to $4\mu_B$ here and is localized. As seen in the section 1.3.2 the Mn atoms are not in direct contact, the interaction is indirect among the Mn moments and is sensitive to both distance and percentage of X (Mn) and Z elements. The initial analysis of the inelastic neutron scattering by Noda and Ishikawa and Tahuna *et al.* on the Ni_2MnSn, Pd_2MnSn and Cu_2MnAl showed that interaction was long ranged and oscillatory in nature [27,28]. The ferromagnetism arises due to the Ruderman-Kittel-Kasuya-Yoshida (RKKY) exchange interaction, while the origin of antiferromagnetic (AFM) interactions in Heusler alloys with excess Mn is still elusive [29–31]. The study with Monte Carlo simulation shows that the antiferromagnetism is outcome of RKKY interactions between Mn atoms [30]. Alternatively some first principles study propose superexchange interactions arising due to hybridization between Ni 3d and Mn 3d bands as the origin of antiferromagnetic interactions [26,32].

In austenitic phase the interaction among the Mn-Mn in regular Mn site is ferromagnetic and the interaction is weakly antiferromagnetic between the Mn-Mn atoms in Mn site and Mn in the Z site. The antiferromagnetic interaction is sensitive to distance and it is enhanced at shorter distance [33,34]. The structural transformation to martensitic phase shortens the lattice parameter in one dimension so that the Mn-Mn distance becomes less, ($c_{mar} = c_{aus}/\sqrt{2}$) thus the AFM interaction among Mn-Mn atom in Mn site and Mn in the Z site is enhanced. However, in another dimension the Mn-Mn distance is increased ($a_{mar} = \sqrt{2}a_{aus}$), thus preserving the ferromagnetic character. The resulting magnetic state of the martensitic phase has competing FM-AFM interaction leading to observation of properties like spin glass and exchange bias effect [24,35–38].

The magnetic states of the austenitic and martensitic phase are shown as the function of e/a in Figure 1.4, where T_C^A and T_C^M are the Curie temperatures of austenitic and martensitic phase. The T_C (will mean T_C^A unless otherwise mentioned) for each Z shows little variation, though it falls with increasing e/a. The fall occurs because of increase in probability of Mn occupying the Z site, where the Mn interacts antiferromagnetically. Also with increase in e/a the Mn-Mn distance decreases which strengthens the AFM interaction [15]. One also observes that T_C increases as the Z changes form In to Sn to Sb, showing that FM is enhanced. The T_C of martensitic phase falls much more rapidly with increasing e/a (except of Z = Ga), which shows that AFM strengthens as sample composition moves closer to Ni_2Mn_2 which is AFM with Neel temperature of 1200 K.

These systems show a variety of features in thermomagnetization curve depending on measurement protocol. The temperature dependent magnetization measurement M (T) carried out for $Ni_2Mn_{1.36}Sn_{0.32}Al_{0.32}$ sample is shown in Figure 1.5. All Ni-Mn-Z samples show almost similar behavior except for the Ni-Mn-Ga system. The magnetization falls suddenly when sample undergoes MT around 240 K. This sudden change in magnetization gives rise to many interesting properties in the sample like large magnetocaloric effect (MCE) and giant magnetoresistance (MR) at MT.

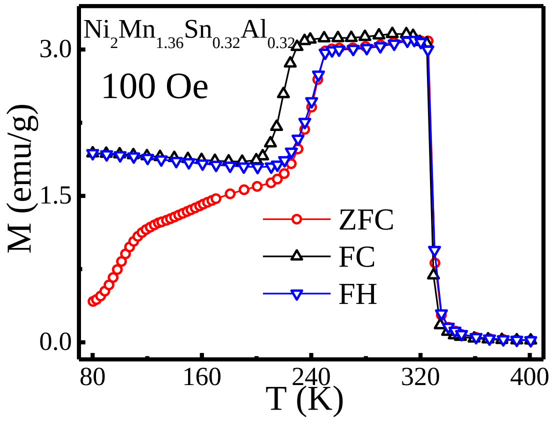

Figure 1.5 Shows thermomagnetization curves measured in zero field cooled (ZFC), field cooled (FC) and field cooled heating (FH) protocols in the dc magnetic field of 100 Oe.

1.3.4 Role of magnetism and ordering on martensitic transformation

The Ni-Mn-Z FSMA alloys in the austenitic phase exist in the $L2_1$ structure. At high temperature the structure has B2 structure which upon cooling transforms to $L2_1$ structure. The transformation to $L2_1$ phase from B2 phase is first order transformation. The B2-$L2_1$ transition takes place at different temperatures for different Z atoms [39–43]. Upon quenching form high temperature (above the B2-$L2_1$ transition temperature), the B2 phase may coexist with $L2_1$ phase as the cooling does not take place at equilibrium. The B2 phase as discussed earlier is disordered phase of $L2_1$ structure where the Mn and Z sites are randomly occupied. Thus more of Mn atoms occupy the Z sites which results in more AFM interaction. The presence of B2 phase thus reduces the overall magnetism of the austenitic phase. The Ni-Mn-Al system has lowest B2-$L2_1$ transition temperature thus leading to formation of B2 predominantly, thus resulting in austenitic phase with higher AFM interaction. V. Sánchez-Alarcos et al. performed systematic aging on Ni-Mn-In and Ni-Mn-Ga samples starting from temperature below B2-$L2_1$ transition temperature of system till high temperature [44,45]. They showed that the MT temperature and T_C are influenced by aging. While the MT temperature changed only for the system in which one of the phases was ferromagnetic, the system which transformed from a paramagnetic phase to another paramagnetic phase did not display such a shift.

The neutron diffraction study showed that with increasing aging temperature the $L2_1$ fraction in the sample increases. As samples become more ordered higher percentage of Mn atom occupies the Mn site, which in turn results in the enhancement of ferromagnetism of the sample. The change in magnetism of the sample influences the Gibbs free energy of the system. Depending on which phase has higher saturation magnetization the transformation temperature shows negative or positive shift. Overall the structure with higher magnetization gets stabilized with increase in ordering.

1.3.5 Influence of various substitution

FSMA displays a wide variety of properties most of which occur in the vicinity of MT. The transformation is very sensitive to change in e/a, which can be as high as 270 K per 0.1 e/a for Sb system (0.1 e/a corresponds to 2 at. % of Sb) [15] and is also sensitive to the composition. Apart from these the magnetizations of both austenitic and martensitic phases are sensitive to both e/a and composition. Thus an alloy with better functional capabilities may have an operating temperature either too low or too high than room temperature at which most of the devices work.

The transformation temperature can be changed by changing composition which leads to change in e/a ratio of the sample resulting in above effect. Usually with increase in e/a ratio the transformation temperature also reduces [15]. Also the substitution of different elements can bring about the change in the lattice parameters of the system which effects the magnetism thus effecting the stability of phases [44,45]. The substitution can also create chemical hydrostatic pressure which can also bring change in the transformation temperature [35]. Various substitutions have been tried with the aim of both enhancing the functional capabilities and to bring the transformation temperature close to room temperature. These substitutions also help in understanding the origin of magnetism and MT in these samples.

In the Ni-Mn-Z system (where Z = Al, Ga, In, Sn and Sb) the Z element has been replaced with element like Ge, B, Si and partially with other Z elements [46–51]. In general the substitution of Z with element having small radii results in increase in transformation temperature even if e/a ratio of the system fall, because in most of cases the chemical pressure effect dominates. Boron was introduced in Ni-Mn-Sn system which occupied interstitial site and led to increase in MT, though it also introduced a foreign Mn_2B phase in the system at higher concentration thus reducing magnetocaloric effect [46].

There are also studies where Ni and Mn have been replaced by ferromagnetic elements like Co and Fe and with elements like Cr and Cu. The addition of strong ferromagnetic (Co and Fe) element in the Ni-Mn-Z system breaks the crystallographic symmetry in these systems thereby acting as the “ferromagnetic activator” which turned the antiferromagnetically exchange coupled Mn moments between the Mn in regular site and in Z site into the ferromagnetically exchange coupled ones [52]. The addition of Co doped samples show large change in magnetization at the MT even at room temperature [18,53]. These samples also shows nearly perfect magnetic field induced shape memory effect and the work output stress in these systems is at least one order of magnitude higher than the conventional Ni-Mn-Ga [18,53–55]. The addition of Co results in the metamagnetic shape memory effect in Ni-Mn-Co-Z (where Z is Al, Ga, In, Sn, and Sb) system [52,55–58]. The replacement of the Cr with Mn in Ni-Mn-Sb resulted in enhancement of the FM interaction and suppression AFM interaction though the replacement also leads to drop in values of MR [59].

1.4 Motivation of the work

The Ni-Mn-Z (where Z = Sn, Sb and In) system of alloys though shows a lot of interesting properties as discussed earlier, its main draw backward is brittleness. The system with Al was proposed as an alternative as the system is more effective for mechanical devices. But Al based system has short coming of its own [60].

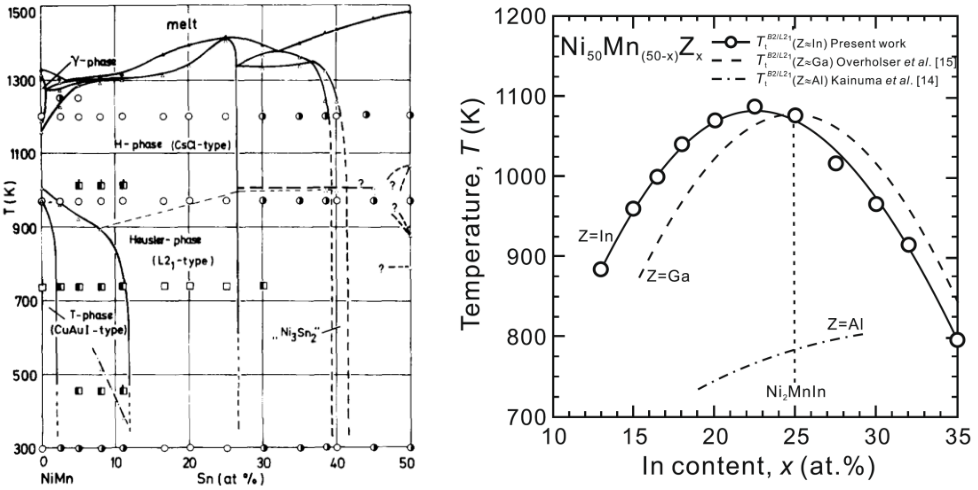

Figure 1.6 (Left) The phase diagram for Ni_2MnSn system showing the B2-L2$_1$ transition temperature (here H-phase is the B2 phase) [39]. (Right) The B2-L2$_1$ transformation determined by the DSC measurements for the Ni_2Mn-In alloys compared with those for the Ni_2Mn-Al and Ni_2Mn-Ga alloys [40].

The Ni-Mn-Al system has a B2 to L2$_1$ ordering temperature in the range of 600 K to 800 K [61]. Thus when Ni_2MnAl system is quenched form high temperature they tend to remain in B2 phase. As said, the main problem with the presence of B2 phase is that it brings more of AFM in the system thus upon structural transformation the change in magnetism is not much. Large values of properties like magnetocaloric effect, magneto-resistance, magnetic field induced stain are usually obtained in the vicinity of structural transformation temperature, where they are driven by large difference in the Zeeman energy of austenitic and martensitic phase [62]. As the change in magnetism is not large the values of these functional properties are much smaller in Ni-Mn-Al system compared to other Ni-Mn-Z (where Z = Sn, Sb and In) [63,64]. It was argued that if more of ordered L2$_1$ phase could be stabilized in the Ni-Mn-Al system then there functional capabilities could be enhanced [64]. Careful and long heat treatments are required at lower (than B2 to L2$_1$ ordering temperature) temperature to stabilize larger fraction of L2$_1$ phase as kinetic of system is very low [64,65].

The presence of Z elements increase the B2-L2$_1$ transition temperature and the system with Z as Sn, In and Ga display much higher B2-L2$_1$ transition temperatures compared to Ni-

Mn-Al system [40,61,66] as shown in the Figure 1.6 (figures were taken from Ref. [39] and [40]). We see from Figure 1.6 that replacement of element like Sn and In with Al can possibly keep the B2-L2$_1$ transition temperature of the system high. Thus obtaining the L2$_1$ phase will become easier even at higher Al content which in turn may lead to better functional capabilities.

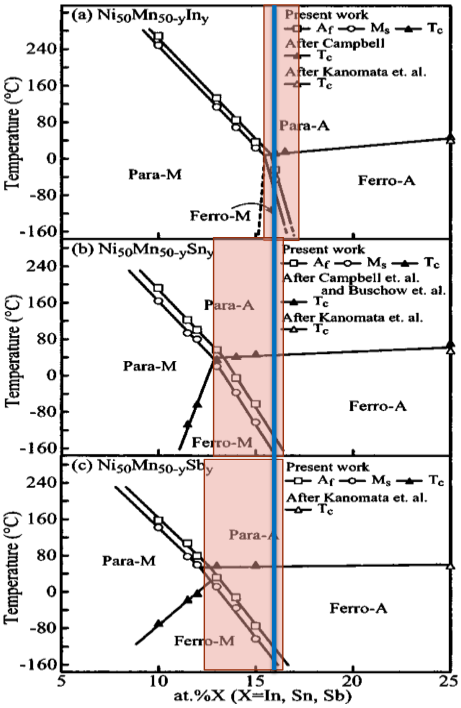

Figure 1.7 Martensitic and magnetic transition temperatures of the (a) $Ni_{50}Mn_{50-y}In_y$, (b) $Ni_{50}Mn_{50-y}Sn_y$ and (c) $Ni_{50}Mn_{50-y}Sb_y$ alloys, where the Para and Ferro mean paramagnetic and ferromagnetic, respectively, and A and M indicate the austenite and martensite phases [67]. The shaded region in red shows the composition for which sample undergoes transition to a magnetic phase and the blue line corresponds to the composition of $Ni_{50}Mn_{34}X_{16}$ ($Ni_2Mn_{1.34}Z_{0.64}$ in our notation).

The Ni-Mn-Z (for Z as Sn, Sb and In) system shows martensitic transformation in the narrow range of composition, in which at least one of the phases has a long range interaction present. The Figure 1.7 which is modification of figure taken form the Ref. [67] shows the shaded region of composition in which at least one phase has long range magnetic interaction. We see that Sn and Sb systems display lowest change in martensitic transformation temperature with change in Z concentration and the region in which sample underwent martensitic transformation to magnetic austenitic or martensitic phase is much broader compared to the Ni_2MnIn system. Based on Figure 1.7 we selected the composition of $Ni_2Mn_{1.34}Z_{0.64}$ (Z is Sn, Sb and In) for the substitution with Al in place of Z as shown with bold line. As mentioned earlier the substitution of element with having smaller radii increases the transformation temperature even when the e/a ratio decreases. With the replacement of Al in the Z position we expect that the transformation will move to higher temperature and thus we selected the system with Z = 0.64 as it has lowest martensitic transformation temperature with both austenitic and martensitic phase being magnetic.

We have prepared three different series of alloys where we substituted Al in the Z position in $Ni_2Mn_{1.34-x}Z_{x,}$ where Z being Sn, Sb and In and x was varied from 0.24 to 0.40 in the step of 0.04. The samples were characterized using the experimental techniques discussed in the Chapter 2. Their detailed characterization and magnetic properties are discussed in details in the Chapter 3. The functional properties of system like magnetocaloric effect and the exchange bias effect were discussed in details in the Chapter 4. The presence of mixed FM/AFM interaction in the martensitic phase of these systems leads to frustration and freezing at low temperature. We have studied the dynamics of these frozen states using ac and dc magnetic measurement techniques and the effect various substitution has on the dynamics of the system was studied in the Chapter 5. The Ni-Mn-Al system showed better functional capabilities when low temperature heat treatment was performed to enhance the $L2_1$ fraction in the sample. As our systems had large percentage of Al we have performed similar heat treatment study on the selected systems at both low and high temperatures. The effect of heat treatment on the magnetism of the system, magnetocaloric effect and freezing at low temperature was studied and are reported in the Chapter 6. Finally we have compared two of the selected system with the composition $Ni_2Mn_{1.36}Sn_{0.40}Al_{0.24}$ and $Ni_2Mn_{1.36}Sb_{0.40}Al_{0.24}$ as they had identical lattice parameters and concentrations of magnetic Mn atoms, and thus tried to look into the origin of magnetism in these systems in Chapter 7.

Chapter 2

Experimental Techniques

In this chapter we shall explore in details the types of instruments used for preparing samples and their characterizations. We shall also explain various experimental techniques developed to characterize the samples and also study their properties. To measure ac susceptibility and study the relaxation phenomenon in the FSMA we setup ac susceptometer. A four probe resistivity setup was made to study the transport properties. Apart from these, a cryostat was made which facilitated the measurements of susceptibility and resistivity from 80 K to 400 K. All the above setup was automated to perform measurement with the help of GPIB interface using Lab-VIEW 10^{TM}. We shall also describe various other existing experimental techniques used to perform measurements like differential scanning calorimeter, X-Ray diffraction, Energy dispersive X-ray analysis, SQUID and magnetoresistance.

2.1 Preparation

The samples were prepared in ingot form by melting the high purity constituent elements in Tri-Arc Furnace under argon atmosphere. The furnace is of Centorr/Vacuum Industries Model 5TA (shown in Figure 2.1). The furnace is capable of reaching 3000° C and more for melting of metallic alloys with the three arcs working together with the passage of total maximum current up to 400 A. The furnace consists of mainly two parts: (i) a hearth with a cup of one electrical polarity and (ii) electrodes with opposite polarity. Elements to be melted are placed in a cup shaped copper hearth and the electrodes are used to strike the arc for melting the material**.**

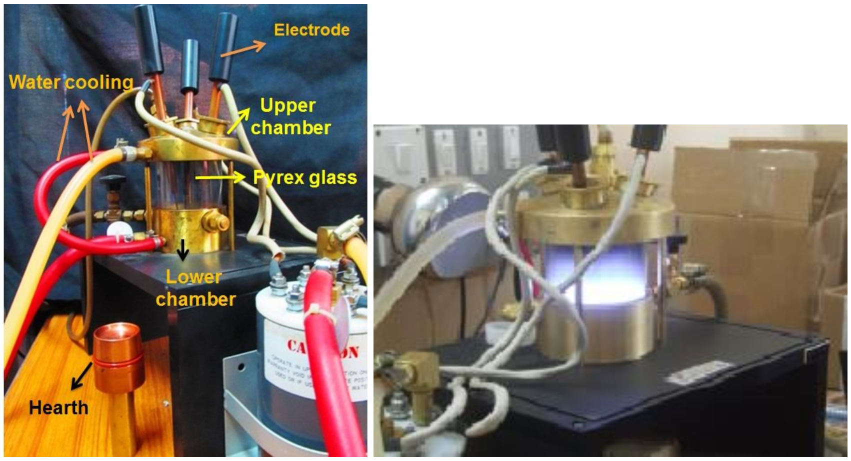

Figure 2.1 Tri-Arc Furnace used in sample preparation (left) and arc in the furnace during sample preparation (right)

The hearth with materials for melting was then inserted into trapped bottom of furnace and clamped into position. The bottom and top of the furnace were water cooled. These two parts were separated by a pyrex glass tube for viewing purpose. The bottom part cooled the hearth and top part cooled the three copper stinger rods which carry equally placed tungsten electrodes. Each rod was mounted into a swivel ball which allowed angular as well as vertical movement. The furnace was then purged by a vacuum pump from Vacuum Techniques Ltd.^{TM}, followed by backfilling with inert gas argon. These processes of purging and backfilling were repeated several times to make sure that no other gas was present in chamber. The argon gas flowing was then continued throughout the melting process till sample and chamber cooled down to room temperature to prevent oxidation. Sample was melted by striking the arc on the sample with the tungsten tip of the rod. The current was initially kept at zero and was gradually increased. After sample had melted the stingers were moved around and above the sample to obtain a uniform and homogeneous melt. Then current was then gradually lowered and then turned off. The sample was turned over after cooling and remelted several times to insure homogeneity. Throughout the process, the current in the furnace was never exceeded a total of 120 A. The sample material had a maximum weight of 2.5 g.

2.2 Annealing

The as-prepared ingots of the samples were cleaned to remove the layer of oxide from surface. Then the samples were ultrasonicated in alcohol bath for cleaning. The samples were then sealed in evacuated quartz tubes. Prior to sealing the tube was purged with vacuum pump and flushed with argon gas several times so that sample did not oxidize during annealing. The samples were then annealed at various temperatures. The initial annealing performed in most samples, was between 1073 K and 1273 K, and then quenched in ice water. The main objective of annealing was twofold 1) the homogenization of the samples, 2) formation of high temperature single phase [68,69]. In order to arrest the high temperature phase the sample was rapidly quenched as mentioned above. The quenched sample was then cut with a low speed diamond saw (IsoMet^{TM}, Buehler, USA) into various shapes and sizes according to the need of the experiments. In few experiments the samples were annealed for second time to study the effect of heat treatment and ordering on the low temperature freezing and other functional properties of the alloy. To do so the small pieces of samples were again sealed in quartz tube following the above mentioned procedure and then quenched or cooled as per experimental needs.

2.3 Characterization

The samples were characterized using various methods. Compositions of the samples were determined using energy dispersive x-ray (EDAX) analysis. Crystal structures of the alloys were determined with X-ray diffraction (XRD) performed on the powdered samples. To measure the first order structural transformation of the samples we did differential scanning calorimetric (DSC) measurements. In this section we shall describe these characterization technique in brief along with the other experimental techniques developed and used.

2.3.1 X-Ray Diffraction

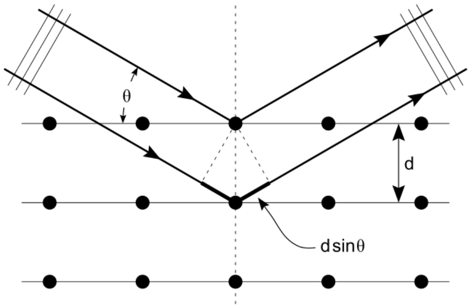

Figure 2.2 X-ray diffraction from lattice planes with spacing d. The diffraction maximum appears at an angle θ whenever the path difference $2d\sin\theta = n\lambda$.

X-Ray Diffraction (XRD), first observed in 1912 in a crystal, is the first step in determining the phase of the alloy. The interaction of X-ray of suitable wavelength with the crystal, results in elastic and inelastic scattering of the radiation. The periodic arrangement of atoms in crystal leads to definite phase relation between radiations scattered elastically from the atom, leading to constructive and destructive interferences, giving rise to diffraction pattern. Although each atom acts as a scattering center, the pattern can be explained by assuming that a plane of atom acts as scattering source. If the planes are separated by a distance d, then the constructive interference takes place only when the angle of incidence (θ) of the incident radiation of wavelength λ is such that it satisfies the relation 2d Sinθ = n λ, where n is integral (the process is shown in the Figure 2.2). This is called Bragg’s law. The distance between planes and the lattice parameter of a crystal can be obtained by using Bragg's law on the diffraction pattern obtained from a diffractometer.

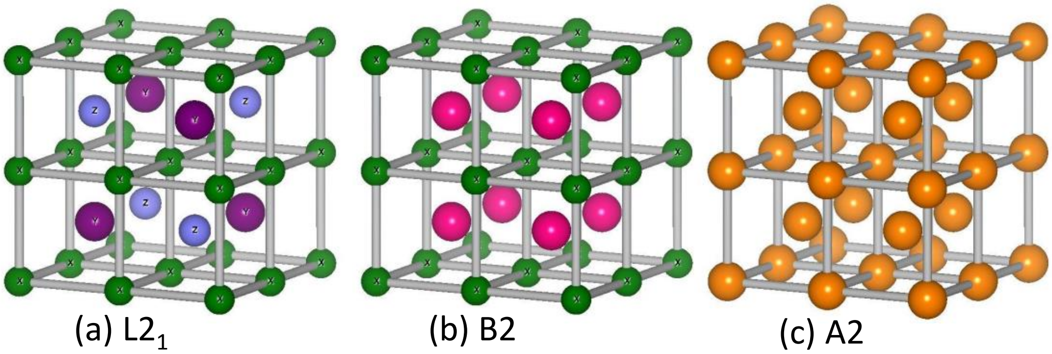

Figure 2.3 Crystal structures of Heusler alloy (a) ordered $L2_1$structures and atomically disordered structures (b) B2 and (c) A2 are also shown.

The X-Ray diffraction measurements were done here with a RIGAKU MiniFlex^{II} diffractometer. The X-Ray tube with Cu target producing Cu K_α (λ=0.154 nm) was used to characterize the samples. The prepared samples were crushed in mortar and pestle to form powder. The powder was kept in sample holder and XRD pattern was obtained with scan rate of 1°/min and step size of 0.02°. The obtained data were analyzed using Fullprof software. Profile fitting was performed on each XRD pattern and then the Rietveld refinement was done [70,71].

As discussed earlier in the section 1.3.2, in fully ordered arrangement Heusler alloy (X_2YZ) crystallize in the fcc $L2_1$ structure in austenitic phase as shown in Figure 2.3 (a). This structure has four interpenetrating face centered cubic (fcc) sub-lattices A (X), B (Z), C (X) and D (Y) atom at (0, 0, 0), (3/4, 3/4, 3/4), (1/2, 1/2, 1/2) and (1/4, 1/4, 1/4) respectively. When the positions (1/4, 1/4, 1/4) and (3/4, 3/4, 3/4) are randomly occupied by Y and Z then the system reduces to a bcc B2 type structure (Figure 2.3 (b)) and when all the atoms (X, Y and Z) occupy all the coordinates randomly then the system is reduced to simple cubic A2 type as shown in Figure 2.3 (c). For $L2_1$ structure the structure amplitudes (F) are given as

(i) h, k, l all odd, $F[1\ 1\ 1] = 4(f_B - f_D)$

(ii) h, k, l all even and $(h + k + l)/2 = 2n + 1$, $F[2\ 0\ 0] = 4\ (2f_A - (f_B + f_D))$

(iii) h, k, l all even and $(h + k + l)/2 = 2n$, $F[2\ 2\ 0] = 4\ (2f_A + f_B + f_D)$

Reflections with $(h + k + l) = 4n$ are the principal reflections, which remain unaffected by the ordering the system [72]. The structure factor amplitude for the case where h, k, l are all odd and $(h + k + l) = 4n + 2$, known as superlattice reflection, is sensitive to ordering and site disorder affects the intensities of these. For a total disorder in site B and D, $L2_1$ structure will reduce to B2 structure (see Figure 2.3 (b)) and superlattice reflection, where h, k, l are all odd (e.g., [1 1 1]) are absent altogether. Furthermore, even then superlattice diffraction lines $(h + k + l) = 4n + 2$ (e.g., [2 0 0]) vanish when there is XYZ disordering (A2 structure). Thus by looking at the diffraction pattern and indexing the peaks properly one can get an idea about the ordering in these systems [73].

2.3.2 Energy dispersive x-ray analysis

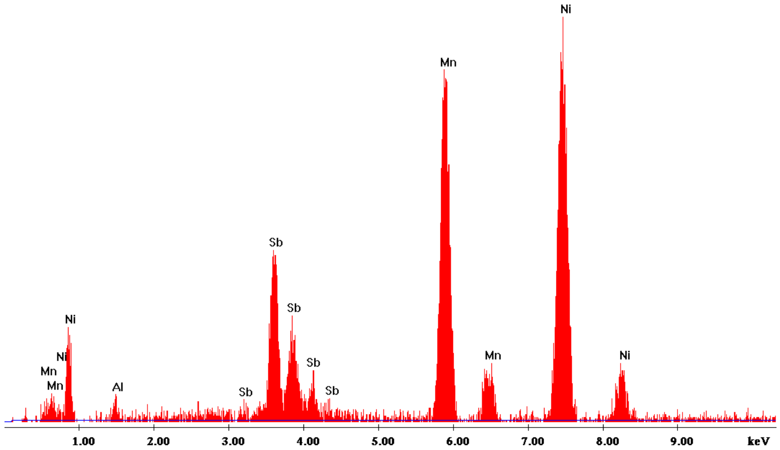

Figure 2.4 EDAX measurement performed on a Ni-Mn-Sb-Al sample.

A Scanning electron microscope (SEM) is widely used in imaging and composition analysis techniques in material science. It works by using a beam of electrons emanating from an electron gun in vacuum and is accelerated by a high potential difference and collimated. The beam is focused onto sample with the help of electrostatic field. Sufficiently high energy electrons interact with an innermost K- level electron of an atom in the material, ejecting it form the shell and creating a vacancy. Another electron in higher energy level fills this vacancy thereby emitting electromagnetic radiation equal to difference of the two energy levels, which is mostly in region of X-ray [74]. For imaging purpose secondary and backscattered electrons are commonly used. Each element emits its own characteristic X-ray, thus by measuring the number of X-ray photons and the energy of X-ray by using energy-dispersive X-ray (EDAX) detector placed inside the SEM chamber one can determine composition of sample nondestructively. A typical EDAX curve for an Ni-Mn-Sb-Al sample is shown in the Figure 2.4.

2.3.3 Differential Scanning calorimetry (DSC)

The martensitic transformation is a first order structural transformation and hence the FSMA system while undergoing reversible transformation releases and absorbs latent heat. The heat of transformation, transformation temperatures and the specific heat capacity of different phases of a material are commonly determined using DSC [75]. It is widely used to study the transformation of FSMAs. There are basically two categories of

DSC, one is called the power compensation DSC and other called the heat flux DSC as shown in the Figure 2.5 [76].

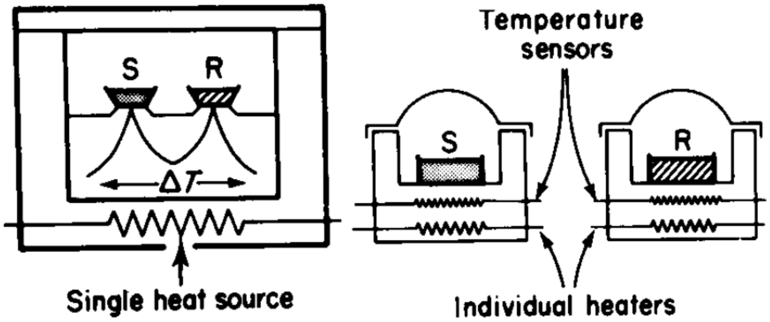

Figure 2.5 (left) Heat flux DSC; (right) power–compensation DSC.

In our measurements we have used a commercially available Thermal Analysis Q-2000™ instrument for DSC measurement, which works on the principle of heat flux DSC. The heat flux DSC uses a single furnace connected by a low resistance heat flow path to both the sample and reference. The temperature difference is measured, which is related to the change in heat capacity of the sample relative to the reference. The value of enthalpy is calculated from the calibration curve. We have used finned Air Cooling System, to allow us to operate from ambient to more than 1000 K, using flowing high purity nitrogen gas as the coolant. The DSC measurement was done down to 100 K, using liquid nitrogen cooling system attachment, with flowing helium gas as the coolant. The instrument had temperature accuracy of ± 0.1K, calorimetric precision (indium metal) of ± 0.05 %, dynamic measurement range > ± 500 mW and a sensitivity of 0.2 μW.

We have also used the purpose built DSC by J. Marcos et al. [77] to measure the entropy change in our sample under application of large magnetic field. This device was an upgraded version of that described in Ref. [77], which enables operation at temperature range 80–450K. Figure 2.6 shows (a) side and (b) top cross sections of the calorimeter. The differentially connected sensors were batteries of thermocouples (Ferrotec TE 9502/ 031/012 M). One of the faces of the sensors was in contact with the calorimetric copper block, and sample and inert reference were directly placed in contact with the opposite faces, tightly kept in place by Teflon tape. The temperature of the calorimeter was monitored by a Pt-100 resistor embedded into the block. The calorimeter was placed on top of a closed aluminum container through which a cryogenic fluid circulates. The fluid temperature and flow were controlled by a Lauda Proline$^{\text{TM}}$ thermal bath. The ensemble of the calorimeter and container was placed into a Dewar flask which was located into the bore (100mm diameter) of a 6T Cryogen-Free Magnet from Cryogenic Ltd. Height and centering were adjusted so that the sample stays in the region where the field produced by the magnet was calibrated and constant. The calorimeter had been calibrated using standard procedures and featured a good sensitivity. It had also been checked that the sensitivity does not depend on magnetic field for fields up to 6T.

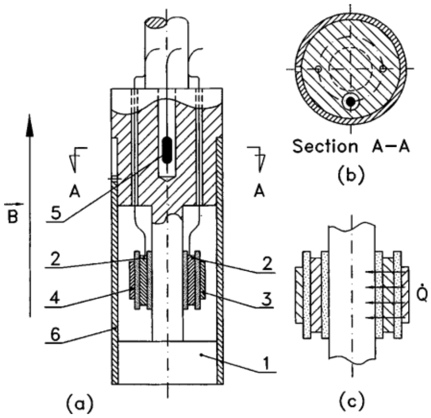

Figure 2.6 (a) Side and (b) top view cross sections of the calorimeter. (1) Copper spool, (2) sensors, (3) sample, (4) reference, (5) carbon-glass resistor, and (6) cover. The magnetic field, B, is along the symmetry axis of the calorimeter; (c) detail showing the heat flow Q for an exothermal transition [77].

2.3.4 AC susceptibility setup and measurement

Magnetic susceptibility measurement is a powerful, nondestructive and established tool for the study of magnetic state of a material. The susceptibility measurement can be performed by either dc magnetometer (χ_{dc}) or an ac susceptometer (χ_{ac}), both techniques give slightly different information about the magnetic character of the samples. The measurement of χ_{dc} requires a dc biasing field. The χ_{ac} measurement can be performed under very small oscillating magnetic field, with or without an external dc biasing field. In the ac measurement, the moment of the sample changes in response to an applied ac field, allowing dynamics of the magnetic system to be studied, this provide a wide variety of information about its magnetic properties like the phase transition and relaxation phenomena. The ability to measure higher harmonics as a function of both temperature and frequency help in distinguishing various kinds of interaction taking place in the system. This technique becomes especially more useful in system where dynamics are slower like in spin glass or superparamagnet.

2.3.4.1 Theory

The magnetic susceptibility, χ, of an isotropic substance is defined as the intensity of magnetization acquired by an infinitely thin bar placed lengthwise in a uniform field of unit magnetic force. Thin bar ensures no demagnetizing force is present. For a sample placed in the uniform magnetic field H with magnetic moment per unit volume M, the magnetic susceptibility is defined as

$$\chi = \frac{\mathrm{M}}{\mathrm{H}}, \tag{2-1}$$

Usually χ is measured using above relation, by applying static magnetic field H and measuring corresponding magnetization M in the sample [78,79]. However this method fails when M is not directly proportional H, the susceptibility is then measured using ac susceptibility technique. In order to measure ac susceptibility, the sample is generally driven with an applied ac magnetic field H_{ac}. The magnetic moment of the sample follows the applied field cycle. As a result, χ is due to the changing moment of the sample as it responds to the ac field and not to the moment itself as in dc technique. The χ in this case is given as

$$\chi_{ac} = \frac{\partial M}{\partial H_{ac}}, \tag{2-2}$$

Thus, the χ_{ac} is actually the slope (dM/dH) of the magnetization curve (M versus H curve) in the limit of small ac fields, and this is why sometimes referred to as a differential susceptibility.

Consider a sample placed in the magnetic field $H_{ext} = H_{dc} + H_{ac}$ having the static component H_{dc} and ac component H_{ac} characterized by the frequency $f = \omega/2\pi$ and the amplitude H_a given by

$$\mathrm{H_{ac}} = \mathrm{H_a} \cos(\omega \mathrm{t}), \tag{2-3}$$

In general, using equation (2-2) the ac susceptibility of a material with magnetization (M) can be expanded in power series of oscillating magnetic field (H) as.

$$M\,(t) \;=\; \sum H_{ac}\,(\chi_n^{/} cos\, n\omega t \;+\; i\,\chi_n^{//}\, sin\, n\omega t) \tag{2-4}$$

The real and imaginary component of susceptibility $\chi_n^{/}$ and $\chi_n^{//}$ are determined directly from *M(t)* through the relationship

$$\begin{aligned} \chi_n^{/} &= \frac{1}{\pi H}\int_0^{2\pi} M(t)\sin(n\omega t)d(\omega t) \\ \chi_n^{//} &= \frac{1}{\pi H}\int_0^{2\pi} M(t)\cos(n\omega t)d(\omega t) \end{aligned} \tag{2-5}$$

Here n=1 denotes the fundamental susceptibility while n= 2, 3, 4… etc are the higher order harmonics associated with nonlinear terms in χ. $\chi_1^{/}$ and $\chi_1^{//}$represent the fundamental real and imaginary components associated with the dispersive magnetic response and adsorptive dissipation associated within the sample respectively [78,79]. For simplicity, we used $\chi^{/}$ and $\chi^{//}$ instead of $\chi_1^{/}$ and $\chi_1^{//}$ in the later parts of the thesis.

2.3.4.2 Set up

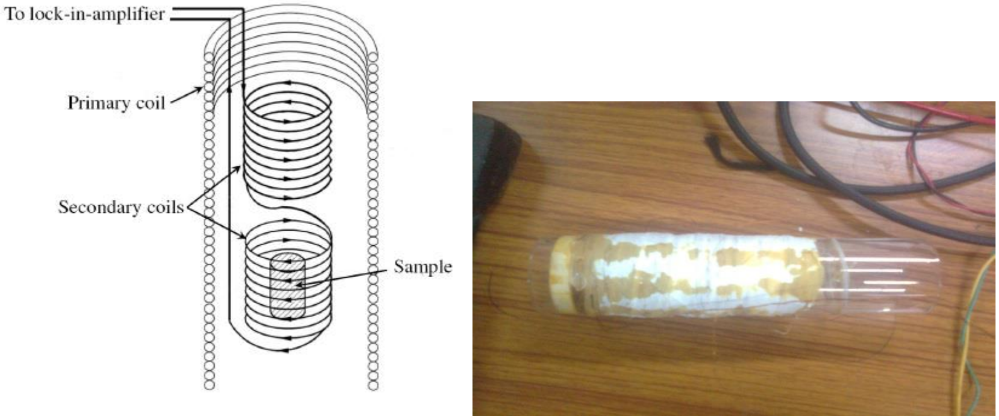

Figure 2.7 The schematic of ac susceptibility primary and secondary coils (left) and the ac susceptibility system used in measurement (right side).

A typical ac-susceptometer for measuring the magnetic susceptibility usually works by using the mutual inductance principle [79]. The sample is excited by an ac field produced by the primary coil, which produces magnetization. This is detected using a system of secondary coils which usually consists of two coils, inductively coupled to primary as shown in the Figure 2.7. The detection coils are connected in differential mode and balanced so that the signal is minimum when no sample is present.

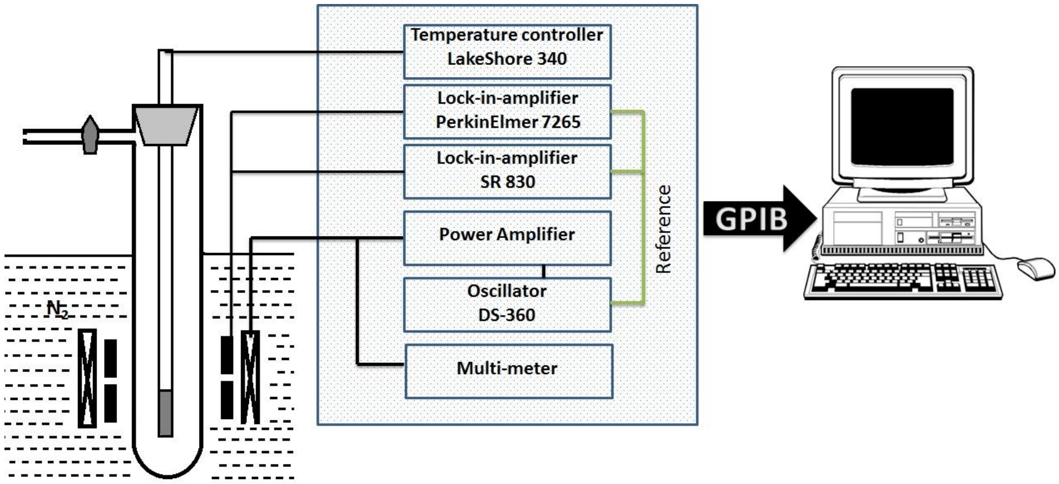

Figure 2.8 Schematic of the experimental setup used for ac susceptibility measurement.

Two coils were made to measure the susceptibility effectively at low and high frequency. Coils were made on a Borosil^{TM} tube as it does not interfere with measurements being non-conducting and very weakly diamagnetic. The coil used in measurement is shown in the Figure 2.7. The secondary coils, which act as detection coils, were wound first in opposition with equal number of turns in identical manner. These two coils were connected in series in differential mode and output across it was fed to a transformer type pre-amplifier Standford Research SR-554^{TM}. The output form pre-amplifier was connected in parallel to Perkin Elmer DSP 7265^{TM} and SR-830^{TM} lock-in-amplifiers. The primary coil was wound above the secondary uniformly in such a way that both detection coils were at its center. Primary coil was driven by ac source consisting of Stanford Research System DS-360^{TM} Ultra Low Distortion Function Generator followed by a power amplifier. The schematic of the setup is given in the Figure 2.8. The details of number of turns of primary and secondary coil for both low and high frequency susceptibility measurement are given in Table 2-1.

Table 2-1 coil specification

Coil	Primary turns	Secondary turns
Low frequency system	1235	1000
High frequency system	1000	400

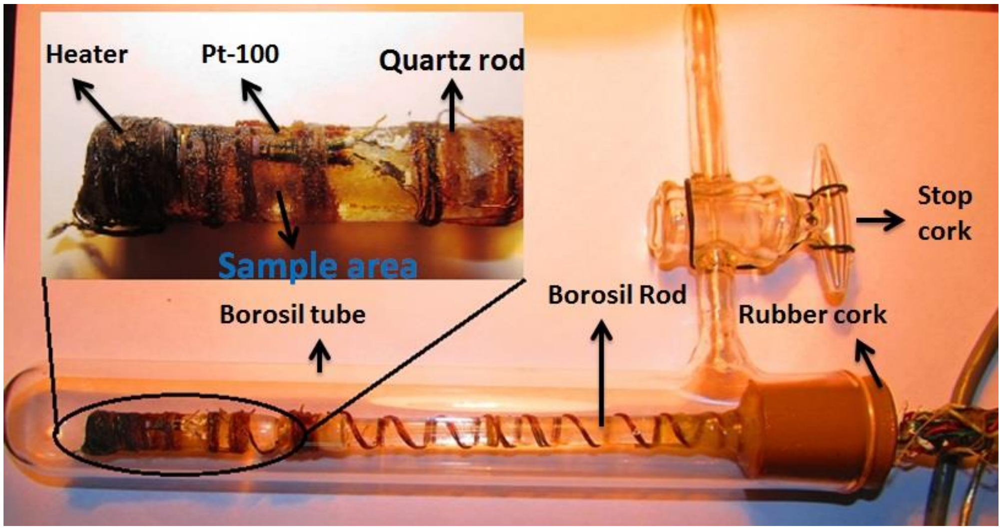

Figure 2.9 Cryostat set up for ac susceptibility measurement in temperature range of 80-400 K. The enlarged region shows the magnified view of the sample area heater and thermometer.

A cryostat was also made to perform measurements within temperatures of 80 K to 400 K. The design and picture of the cryostat is given in Figure 2.9. Sample was kept on sample holder made of quartz (it is also very weakly diamagnetic and is a good thermal conductor). A calibrated Pt-100 thermometer was placed on sample holder such that sample could be placed in contact with it. The quartz holder was attached to a Borosil rod at one end to provide thermal isolation. To heat the sample assembly a heater wire was wound at the other end of the sample holder in anti-parallel arrangement to prevent any magnetic field from generating. A rubber cork was attached on the Borosil rod as shown in the Figure 2.9, wires were taken out to connect the thermometer and heater wires with LakeShore 340$^{\text{TM}}$ temperature controller to measure and control the temperature. The rod assembly was then inserted in a Borosil tube which had a pumping valve to create vacuum using a rotatory vacuum pump. The real and imaginary parts of liner susceptibility were measured by the DSP 7265 lock-in-amplifier and higher harmonics were mostly measured using a SR-830 lock-in-amplifier.

The entire set-up was connected to computer using GPIB and automated using a visual programming language from National Instruments, LabVIEW$^{\text{TM}}$ 2010. Program was designed to make compensation for the off-set voltage in the secondary coil using DSP 7265 lock-in-amplifier. The data were taken at an interval of two seconds and generally at a ramping rate of 1.5 K/minute. The snapshot of the block diagram and the front panel of the program are shown in Figure 2.10.

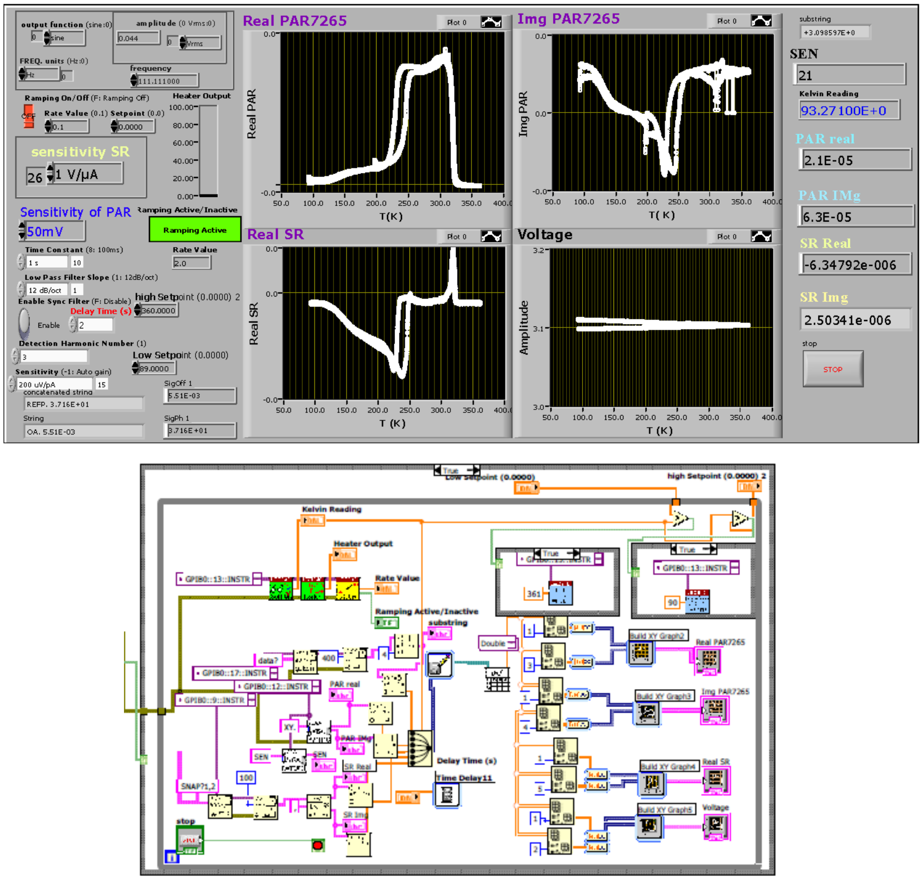
output function (sine:0) 0 sine
amplitude (0 Vrms:0) 0.044 0 Vrms
FREQ. units (Hz:0) Hz 0
frequency 111.111000
Ramping On/Off (F: Ramping Off) OFF
Rate Value (0.1) 0.1
Setpoint (0.0) 0.0000
sensitivity SR 26 1 V/μA
Sensitivity of PAR 50mV
Ramping Active/Inactive: Ramping Active
Time Constant (8: 100ms) 1 s 10
Rate Value 2.0
Low Pass Filter Slope (1: 12dB/oct) 12 dB/oct 1
Enable Sync Filter (F: Disable) Enable
Delay Time (s) 2
high Setpoint (0.0000) 2 360.0000
Detection Harmonic Number (1) 3
Low Setpoint (0.0000) 89.0000
Sensitivity (-1: Auto gain) 200 uV/pA 15
concatenated string REFP. 3.716E+01
String OA. 5.51E-03
SigOff 1 5.51E-03
SigPh 1 3.716E+01
substring +3.098597E+0
SEN 21
Kelvin Reading 93.27100E+0
PAR real 2.1E-05
PAR IMg 6.3E-05
SR Real -6.34792e-006
SR Img 2.50341e-006

Figure 2.10 Top is the front panel of the program use to measure ac susceptibility and bottom is the block diagram of the same.

2.3.4.3 Calibration of the ac susceptibility setup

The coil set up was calibrated before performing measurements. In order to check for the frequency response of the coil, the amplitude of voltage across secondary coil was measured by varying frequency of current in primary coil. The measurements were performed at room temperature and at working temperature of coil i.e. 77 K and are summarized in the Figure 2.11 (a). Measurements on this coil were performed mostly below 5 KHz and from the graph it is clear that the response of the coil was linear in that region at both room temperature and at liquid nitrogen temperature. So coil was well suited to for the measurement below 5 KHz.

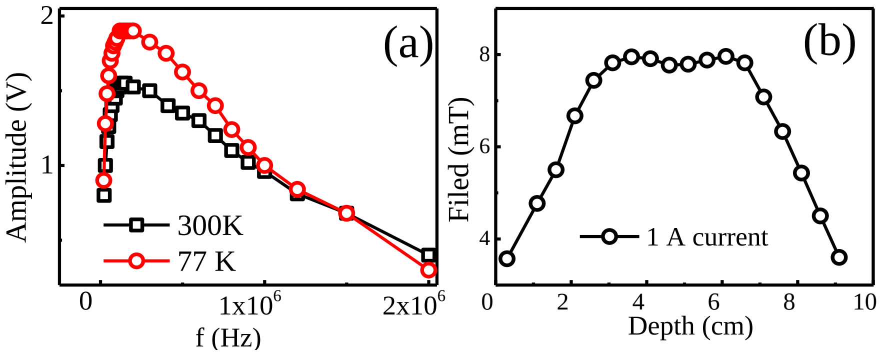

Figure 2.11 (a) Frequency response of voltage measured across the secondary coil of at room temperature and at liquid nitrogen temperature. (b) Magnetic field inside the coil as the function of depth of the coil when the current of 1 A was passed through it at room temperature.

The magnetic field inside the coil was measured as a function of depth of the coil (kept in vertical position). A current of 1 A dc was passed through the primary coil and the resultant magnetic field was measured with a Hall probe as shown in the Figure 2.11 (b). The magnetic field initially increased with increase in the depth and then attained plateau value at depth of 3 cm and then fell again after 7 cm. The secondary coils lied almost in the region of the flat plateau ensuring that magnetic field was uniform in that region. The cryostat was positioned in a manner such that the sample area lied within the lower coil of the secondary system. This arrangement ensured no field gradient was present at the sample.

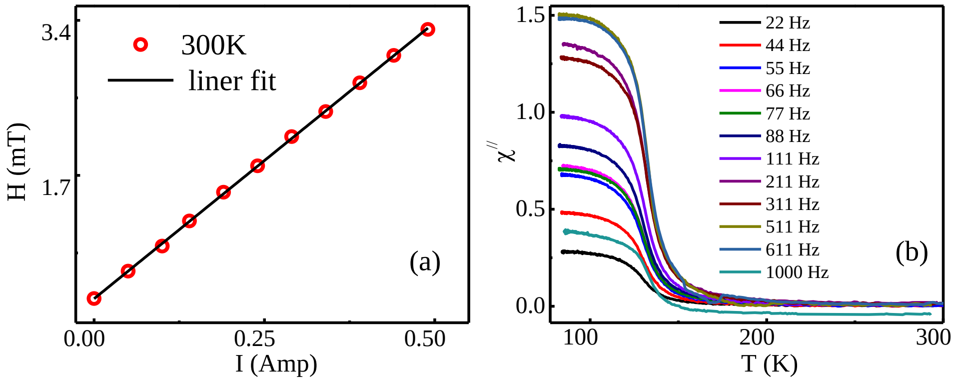

Figure 2.12 (a) Maximum magnetic field inside the coil as the current was varied in the primary coil of ac susceptibility coil. (b) Imaginary part ($\chi^{//}$) of ac susceptibility measured of a standard FM sample at various frequencies.

To further determine the value of the field at which measurement was performed, we measured the maximum field inside the coil by varying current through the primary coil up to 0.5 A dc as shown in the Figure 2.12 (a). The field in the coil increased linearly with the increase in the current. The linear fitting was performed on the data and the field at which most of our measurement was performed was found to be almost 40 Oe.

A standard FM Fe-Ni-Cr sample was placed in the sample holder and measurement was performed on starting from 11 Hz till 2000 Hz, imaginary part ($\chi^{//}$) of ac susceptibility measurement for few frequencies is shown in the Figure 2.12 (b). Similar curves were obtained for the real part of ac susceptibility. The rise in the $\chi^{//}$ as the temperature is lowered is due to paramagnetic to ferromagnetic transition. The T_C at all frequencies was found to agree with the calibrated values.

2.3.5 DC magnetization measurement

The study of magnetic properties of materials helps in the study of electronic behavior in condensed matter. A wide range of materials like alloys of transition metals, the electrons show a highly correlated behavior which results in magnetism, superconductivity, metal–insulator transitions, heavy-fermions etc. These different types of behavior are mainly outcome of the different strengths of Coulomb and exchange interactions among electrons. The study of these interactions requires magnetic measurement at various temperatures and different magnetic fields.

We have used a commercial vibrating sample magnetometer (VSM) and a Quantum Design Magnetic Property Measurement System (MPMS) XL-7^{TM} magnetometer. Their working principles are described below.

2.3.5.1 Vibrating Sample Magnetometer (VSM)

Vibrating Sample Magnetometer (VSM) systems are used to measure the magnetic properties of materials as a function of magnetic field, temperature and time.

A magnetic moment *m* is induced in the sample when it is placed in a uniform magnetic field *H*. In a VSM, a sample is placed within suitably placed sensing coils under constant magnetic field (generated by an electromagnet), and the sample is given a sinusoidal mechanical oscillation with a fixed frequency. A changing magnetic field will produce an electric field given by Faraday’s law of induction, thus inducing a voltage in the sensing coils that is proportional to the magnetic moment of the sample. The schematic of the VSM and detailed configuration near the pick-up coil is given in Figure 2.13 [80,81]. To eliminate errors due to variation in amplitude and frequency of vibration, a nulling technique is employed which uses a vibrating capacitor to generating a reference signal that varies with moment, vibration amplitude and frequency in the same manner as the signal from the pickup coils.

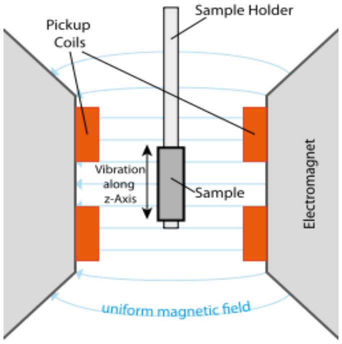

Figure 2.13 Schematic of vibrating sample magnetometer (VSM) [80].

The magnetic measurement of the samples was performed in a Lake Shore Cryotronics make 7400 Series^{TM} VSM. The maximum magnetic field generated in it was 1.56 T. The field produced had homogeneity of ±0.1% over a 5 cm diameter circle. The low temperature measurement was performed using Model 74018^{TM} variable temperature cryostat, which allows measurements from 80 K to 400 K. For the measurements at high temperature Model 74034 high temperature oven was used. It could go form 300 K to 1273 K. Noise level of 1.25 μemu (RMS value) in moment measurement could be achieved.

2.3.5.2 Superconducting Quantum Interference Device (SQUID) Magnetometer

SQUID magnetometers are the most sensitive magnetometers ever made. Its sensitivity is ~ 10^{-14}T, which is at least two orders of magnitude higher than that of a conventional VSM. This extreme sensitivity comes from its ability to measure a single quantum of magnetic flux, called fluxoid and is given by $\Phi = h/2e = 2.0678\ Tm^{-2}$, that is passing through a superconducting ring. It works by measuring the changes across a Josephson junction (Jj) in terms of frequency (rf SQUID) or voltage (dc SQUID). Jj is basically a pair of superconductors separated by a thin layer of insulator. The Cooper pairs are able to tunnel through this barrier and maintain phase coherence in overall superconducting wave function. In dc Jj effect, a current proportional to the phase difference of the wave functions on both sides flow into the junction, even in the absence of externally applied voltage. In ac Jj, the junction can oscillate with a frequency f = 2eΔV/h= 483.6 MHz/μV when a voltage 1μV is applied across the junction.

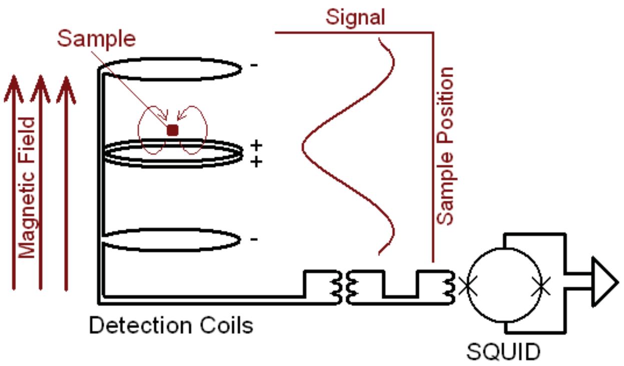

Figure 2.14 A sketch of the SQUID, showing the detection coil and the superconducting quantum interface device.

A schematic is shown in Figure 2.14 for the construction of a magnetometer [82]. A measurement is performed by moving a sample through the superconducting detection coils which are located outside the sample chamber, and at the center of the magnet. The magnetic moment of the sample induces an electric current in the detection coils, the variations in the current in the detection coils produce corresponding variations in the SQUID output voltage which are proportional to the magnetic moment of the sample. Thus a properly calibrated system provides a highly accurate measurement of the sample's magnetic moment.

The detection coil is configured as a second-order gradiometer, it provides a high level of noise immunity compared to the first-order gradiometers. The upper coil is a single turn wound clockwise, the center coil comprises of two turns wound counter-clockwise, and the bottom coil is a single turn wound clockwise. In ideal condition the flux change in the two-turn center coil will be exactly cancelled by the flux change in the single-turn top and bottom coils. The magnetic moment of a sample is measured by moving the sample through the two turns of counter-clockwise portion of detection coils [83].

2.3.6 Resistivity setup and measurement

Resistivity measurement can be used to ascertain a phase transition like martensitic transition which is accompanied with a large change in electron scattering and hence show a large change in resistivity. The alloys usually have low resistance thus the voltage drop across the sample becomes less when low current is passes through the sample. Thus low resistance measurement are subjected to additional error sources, including lead resistance, non-ohmic contacts and thermoelectric effect [84]. The problem of thermoelectric effect can be avoided using the ac resistance measurement technique. The ac resistance measurement, along with phase sensitive detection technique of lock-in amplifier, offers advantage of very high signal to noise ratio making measurement more reliable. To overcome problems due to lead and contact resistances, this four probe arrangement is universally used, as shown in the Figure 2.15 [84].

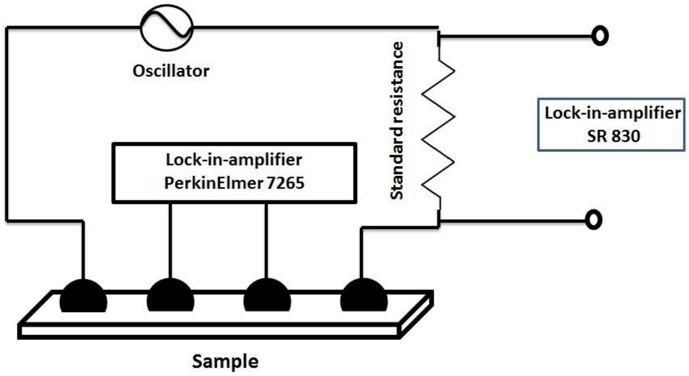

Figure 2.15 Schematic showing the technique used to measure the resistivity of the samples.

The experimental setup is shown in Figure 2.15. The current from ac source, in this case the oscillator of lock-in-amplifier, with a constant resistance in series was forced through outer set of leads. The voltage drop across the sample was then measured through the second set of inner leads called sense leads, using a lock-in-amplifier in phase locked mode. The current flowing through the sense leads was negligible consequently the resistance is determined more accurately. It is also called the Kelvin method. The resistance of sample was given by the ratio of voltage drop across the sense leads to the current passing through the series resistance. To avoid any error due to drift at any moment, the current though series resistance is obtained simultaneously by measuring the voltage drop across the series resistance using another lock lock-in-amplifier. In order to minimize the effect due to non-ohmic contact, the contacts were prepared just before the measurement.

The entire set-up was connected to computer using GPIB and automated using visual programming language from National Instruments LabVIEW 2010. The data were taken at an interval of two seconds and at a ramping rate of 1.5 K/minute. The snapshot of the block diagram and the front panel of the program is shown in Figure 2.16.

The resistance measurements were mostly carried out in a commercially available pulsed tube cryocooler. The magnetoresistance measurements were carried out in commercially available 10 T and 15 T cryogen free magnet systems from Cryogenic Limited.

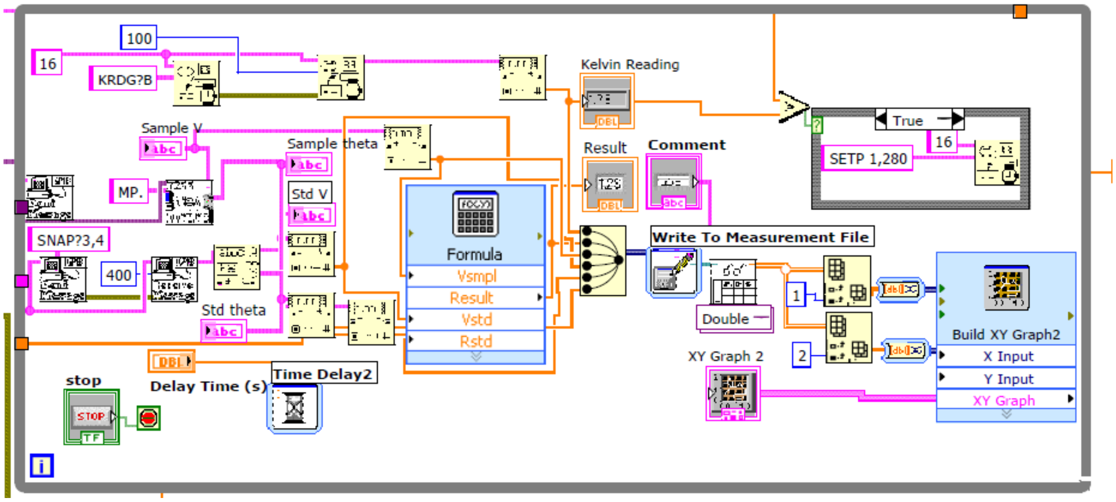

Figure 2.16 Block diagram of the LabVIEW program used to measure of ac resistivity.

Chapter 3

Investigations on Ni-Mn-Z-Al (Z = Sn, Sb and In) system

In this chapter we shall investigate in details the effect of substitution of Al in the Ni-Mn-Z type of systems with Z on the lattice parameter, structural transformation temperature, magnetic transition and magnetization of the system. We have replaced Z gradually with Al in the $Ni_2Mn_{1.34}Z_{0.64}$ *system for Z = Sn, Sb and In. Even after replacing the Z with Al at higher percentage the system still displayed the ferromagnetic shape memory effect. The replacement in general shifted the structural transition temperature towards room temperature. The presence of elements such Sn, Sb and In is expected to stabilize the* $L2_1$ *structure. In Ni-Mn-Sn system the replacement by Al at higher percentage introduced more undesirable B2 phase which leads to deterioration of magnetism in the sample and the transition temperature was found to increase gradually with increasing Al content. In Ni-Mn-Sb system the transition temperature stabilized around room temperature with increasing Al content. The replacement by Al in In system shifted the transition temperature almost close to the magnetic transition temperature thus deteriorating the magnetic property.*

3.1 Ni-Mn-Sn-Al system

3.1.1 X-ray diffraction (XRD)

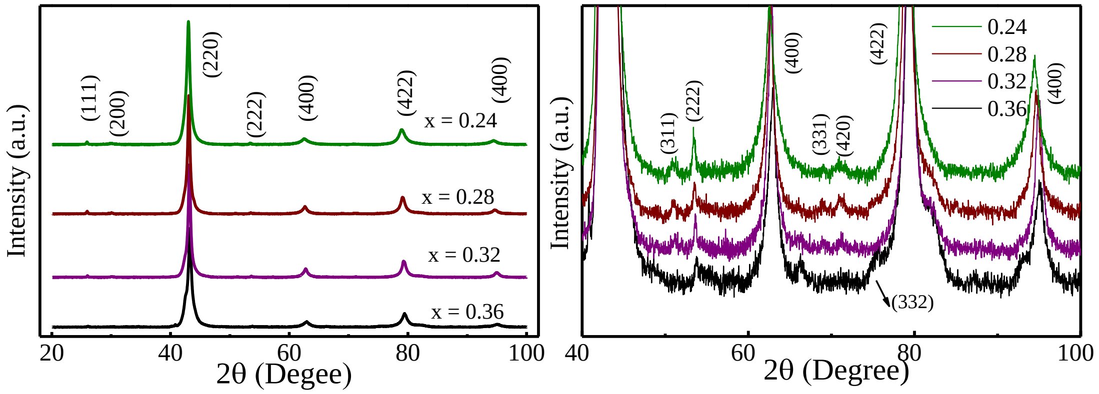

Figure 3.1 X-ray diffraction pattern of $Ni_2Mn_{1.36}Sn_{0.64-x}Al_x$ sample (left) and enlarged view of the peak from 40 to 100 degree (right).

The alloys of composition $Ni_2Mn_{1.36}Sn_{0.64-x}Al_x$ (where x = 0.24, 0.28, 0.32 and 0.36) were prepared by using the Tri-arc furnace as described in section 2.1. To homogenize, samples were sealed in evacuated quartz tubes and annealed at 1273 K for 72 hours and then quenched in ice water as mentioned in section 2.2. EDAX analysis was used to confirm the composition of the alloys.

In Figure 3.1 XRD patterns at 300 K obtained with Cu K_α radiation are shown for the alloys. In the first step of analyzing the XRD result we determined the profile shape function, background and cell parameter using profile matching tool in Fullprof program [71]. With profile fitting we indexed all peaks on the XRD curves. The presence of super lattice peaks [1 1 1] and [3 1 1] along with the principle peak in the sample confirmed that sample was in $L2_1$ structure (space group: *Fm-3m*) [72,73]. All peaks were indexed successfully for systems with x = 0.24, 0.28 and 0.32, showing that no other site disorder was present in the systems whereas in the case of x = 0.36, a small peak corresponding to [3 3 2] was present (shown in magnified view in right side of Figure 3.1). As discussed in Section 2.3.1 peaks with h, k, l all odd or all even, only have non-zero intensity in stoichiometric $L2_1$ structure. This shows that the site disorder was present in x = 0.36 alloys. The pattern showed that all the compositions were in ordered structures in austenitic phase at room temperature, even though a slight site disorder was present in x = 0.36 sample.

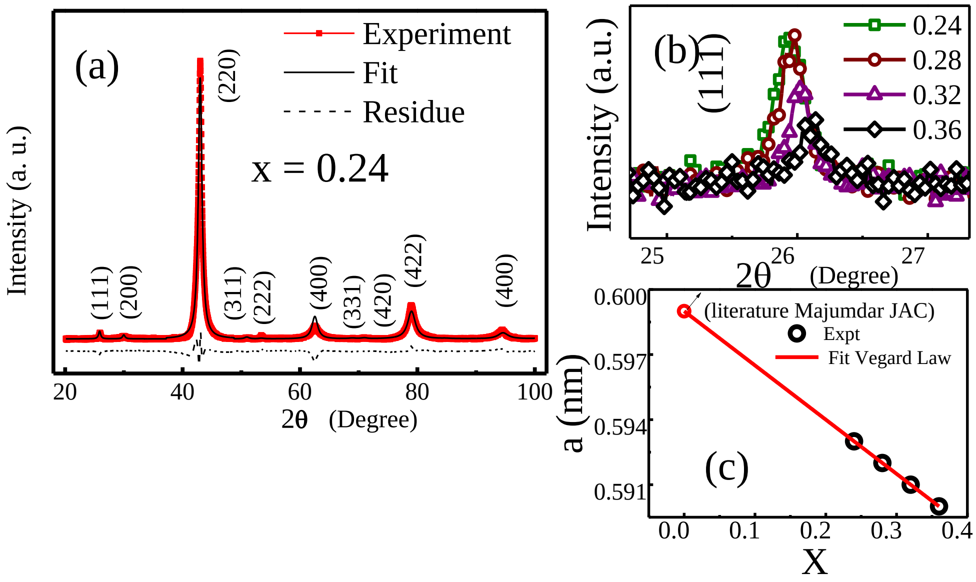

Figure 3.2 a) The XRD pattern for $Ni_2Mn_{1.36}Sn_{0.40}Al_{0.24}$ sample along with the Rietveld refinement curve and residue. b) Shows the magnified view of the 111 peak which corresponds to $L2_1$ ordering in the system. c) Shows the lattice parameter of the system and fitting to the Vegard's law. Red circle data was taken form Ref. [49].

As discussed previously in Chapter 1, the B2 to $L2_1$ ordering temperature is much higher in Ni_2MnSn compared to Ni_2MnAl, thus it is expected that the presence of even small amount of Z will stabilize $L2_1$ phase in Al rich system [35]. The presence of $L2_1$ phase in all samples even after quenching form high temperature confirms this idea. The profile fitted XRD peaks were refined using Fullprof's Rietveld technique. A good fit was obtained as shown in Figure 3.2 (a) for $Ni_2Mn_{1.36}Sn_{0.40}Al_{0.24}$. Similar fittings were obtained for other composition (not shown here). The calculated lattice parameters are shown in Table 3-1 and it can be seen that as Al content increased, the lattice parameters of the austenitic phase decreased, this can be attributed to the fact that ionic radii of Al are smaller than those of Sn [49]. In metallurgy substitution is often examined in terms of an empirical rule called Vegard's law which states that a linear relation exists, at constant temperature, between the lattice parameters of an alloy and concentrations of the constituent elements [85,86]. The lattice parameter was fitted with Vegard's law as shown in the Figure 3.2 (c), excellent fit was obtained thus implying a good substitution.

Degree of $L2_1$ order can be characterized from the ratio of the intensity of superlattice peaks with the intensity of fundamental reflection I [1 1 1]/ I[2 2 0] [87]. The [1 1 1] peak was normalized with respect to the corresponding [2 2 0] as shown in the magnified view in the Figure 3.2 (b). It was found that with increase in Al concentration the [1 1 1] peak corresponding to the $L2_1$ phase remained almost the same for x= 0.24 and 0.28 and then decreased for x= 0.32 and 0.36, relative to [2 2 0] peak corresponding to the B2 and $L2_1$ phase. The result shows that with increase in Al concentration beyond x= 0.28 the system moved to disordered B2 type structure. This is expected for the system was now becoming richer in Al.

3.1.2 DSC

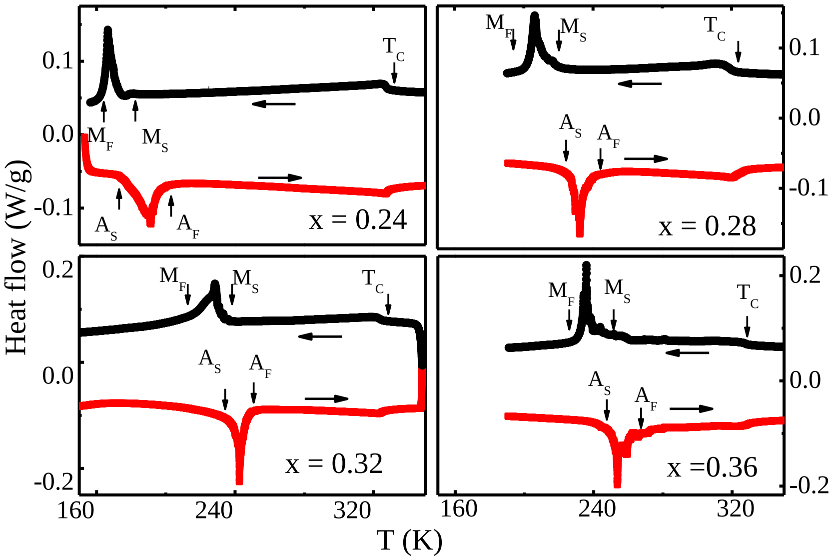

Figure 3.3 DSC curves obtained for $Ni_2Mn_{1.36}Sn_{0.64-x}Al_x$ sample during heating and cooling runs.

Differential scanning calorimeter measurements were carried in order to determine the structural as well magnetic transition temperatures. The obtained DSC thermograms for all compositions are shown in Figure 3.3 for x = 0.24, 0.28, 0.32 and 0.36 samples. The sample showed small change in base line above 300 K in both heating and cooling run with no thermal hysteresis, which is associated with second order magnetic transition from paramagnetic to ferromagnetic austenitic phase. The magnetic transition temperature i.e. Curie temperature T_C was determined from magnetic measurement also.

As the sample was further cooled and heated back large exothermic and endothermic peaks were observed below 300 K during austenitic to martensitic and reverse transformations respectively. The transformation peaks show the typical thermal hysteresis inherent in the first order nature of the martensitic transformation. The transformation temperatures were derived by drawing tangents to the start and end regions of the transformation peaks and the baseline of the heating and cooling curves. Characteristic transition temperatures are defined from the thermogram as M_S: martensitic start, M_F: martensitic finish, A_S: austenitic start, and A_F: austenitic finish temperatures. These are marked in Figure 3.3. The obtained transformation temperatures are given in Table 3-1 and summarized in the Figure 3.4.

It was found that the M_F of the present samples increased as the concentration of x increased whereas T_C remained almost constant. The M_F's of the samples lied between those of $Ni_2Mn_{1.36}Sn_{0.64}$ (110K) [49] and $Ni_2Mn_{1.36}Al_{0.64}$ (~ 415K) [88]. As discussed in the Section 1.3, M_F of Ni_2Mn-Z type of FSMA depends strongly on the e/a ratio and lattice parameter. It decreases with decrease in e/a ratio and increases due to compression of lattice parameter upon substitution of element with smaller radii [49,89,90]. In the present alloy system the M_F increases compared to $Ni_2Mn_{1.36}Sn_{0.64}$ even when the e/a ratio decreased is because of the effect of compression dominated over former.

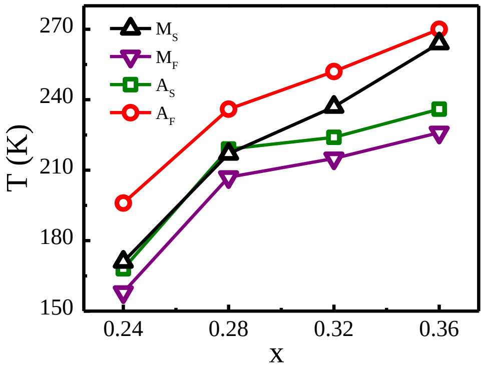

Figure 3.4 Characteristic transition temperatures, martensitic start (M_S), martensitic finish (M_F), austenitic start (A_S) and austenitic finish (A_F) as a function of concentration for $Ni_2Mn_{1.36}Sn_{0.64-x}Al_x$.

3.1.3 AC susceptibility

AC susceptibility measurements were performed at a heating rate of 1.5 K/min in temperature range of 80 K to 400 K. Figure 3.5 shows the χ' of ac susceptibility measurements performed on various samples at frequency of 111 Hz during heating and cooling runs. As the temperature fell below 350 K, the $\chi^{/}$ in all samples showed jumps with no hysteresis, corresponding to the T_C of the austenitic phases. The T_C's obtained are given in Table 3-1 and they agreed with the DSC values within experimental errors. It can be seen that even though the MT temperature shows large variation with increase in Al content T_C remains almost constant. As sample was cooled below 300 K, the martensitic transformation began at M_S and $\chi^{/}$ decreased until it reached the temperature M_F, where the martensitic transformation completed. The $\chi^{/}$ fell with the onset of MT, as discussed earlier, in the Ni_2Mn-Z system interaction between the Mn-Mn atoms, what was predominantly FM in austenitic phase became AFM upon MT because of change in inter-atomic distance. Similarly when reverse transformation occurred, the $\chi^{/}$ started to rise at A_S and increased till A_F where the martensitic to austenitic transformation was completed. The distinct thermomagnetic hysteresis was observed in all samples, this effect was hence associated with structural changes in the system.

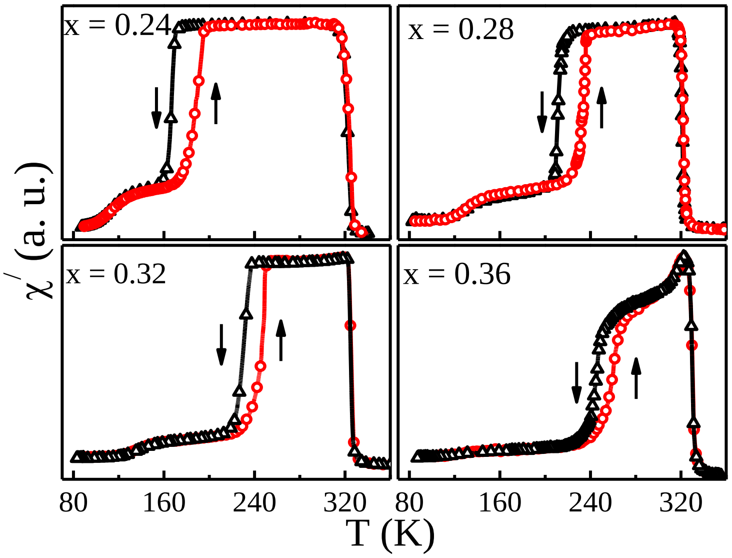

Figure 3.5 Real part ($\chi^{/}$) of ac susceptibility curves measured for $Ni_2Mn_{1.36}Sn_{0.64-x}Al_x$ samples at the frequency of 111 Hz.

As sample was cooled below M_F, the $\chi^{/}$ fell with a step like feature. This fall was investigated in more details in latter chapter and occurred most probably due to freezing of magnetic spins [36,49,91]. The step like anomaly became less prominent for x = 0.36 sample. It was observed that in austenitic phase, below T_C and above A_F, the $\chi^{/}$ fell as temperature was lowered. The ac susceptibility is a dynamic measurement where the response of magnetic material is measured under the influence of oscillating magnetic field. In austenitic phase both FM and AFM interactions were present, but FM interaction dominated over AFM interaction. With lowering of temperature the strength of AFM increased [33] and it pinned the FM region thus the response to driving field decreased, leading to fall in the χ' within the austenitic phase. It was further observed that the fall in χ' increased as the Al content increased. This may happen due to increasing disorder with increasing Al content. The increase in disorder caused larger number of Mn atoms to occupy Sn and Al sites, which interact with Mn in regular Mn site antiferromagnetically. Thus the amount of AFM interaction increases with increase in Al content. As x = 0.36 was more disordered and had higher AFM content, the fall was more pronounced in this case.

3.1.4 DC magnetization

3.1.4.1 Thermomagnetic measurement

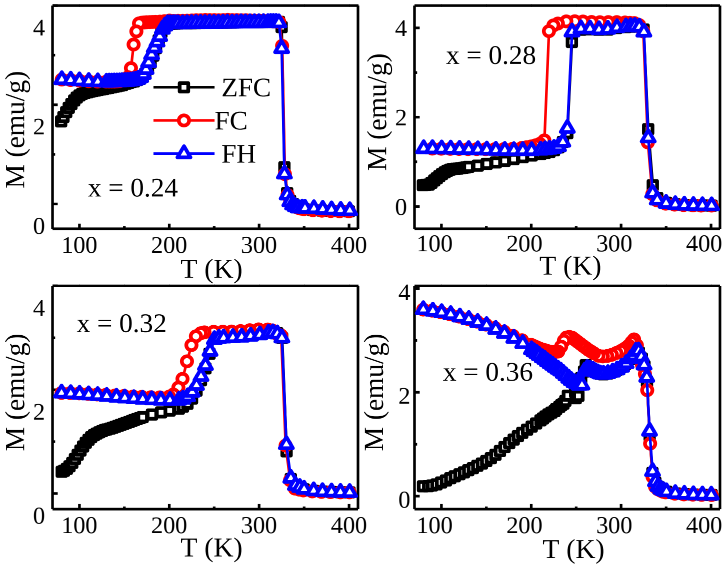

Figure 3.6 Thermomagnetization curve measured in ZFC, FC and FH protocols in VSM in a field of 100 Oe**.**

Temperature dependent magnetization measurements were performed under a constant magnetic field of 100 Oe as shown in the Figure 3.6. In zero-field-cooled (ZFC) protocol measurements were performed till 400 K in heating cycle with a constant dc field, after cooling the sample in zero field to the lowest temperature (80 K) of measurements. The field-cooled (FC) curves were measured in same field from 400 K to 80 K in cooling cycle and field-heated (FH) curve was measured in the warming cycle with the same field. These curves agree with the dynamic ac $\chi^{/}$ measurement of the previous section. In the low temperature region below M_F in the martensitic phase the presence of FM-AFM interaction led to bifurcation in ZFC-FC curve [49,91]. The AFM part pinned the FM matrix in one configuration when sample was heated after cooling in ZFC and in another when it was heated after cooling in presence of field (FH), which gave rise to the irreversibility observed at low temperature.

The bifurcation was also observed in the austenitic phase between ZFC and FC curve below T_C, showing that AFM interaction might exist in the austenitic phase also. The bifurcation increased as Al content increased, showing that antiferromagnetism in the sample increased in austenitic phase with increasing Al.

These measurements can further give information about the strength of competing AFM-FM interaction. It can further be seen from the M (T) curve of the x = 0.36 sample, that the magnetization of the martensitic phase below M_F in FC and FH protocol increased much more rapidly in comparison to other samples, whereas FC and FH curve were almost temperature independent in other samples. This happened because of weaker AFM interaction (even though it has higher AFM content) in x = 0.36 was not able to pin the FM regions, as a result of it the FM regions align in the direction of field with lowering of temperature as in the case of superparamagnet, giving rise to large rise in FC and FH curve at lower temperature [92,93].

Table 3-1 Various parameters obtained are given here. The Curie Temperature (T_C) martensitic start (M_S), martensitic finish (M_F), austenitic start (A_S) and austenitic finish (A_F), lattice parameter (a) in nm and cell volume (v) in nm^3 for $Ni_2Mn_{1.36}Sn_{0.64-x}Al_x$.

x	T_C (K)	M_S (K)	M_F (K)	A_S (K)	A_F (K)	a (nm)	v (nm^3)
0.24	326	171	158	168	196	0.593	0.2085
0.28	324	217	207	219	236	0.592	0.2075
0.32	330	237	215	224	252	0.591	0.2064
0.36	332	264	226	236	270	0.590	0.2054

3.1.4.2 Isothermal magnetic measurements

Magnetic hysteresis curves of the samples were measured upto a maximum field of 1.5 T. The magnetic isothermal curves (M-H) obtained at 300 K are shown in Figure 3.7 (a). The hysteresis curves of all samples displays typical behavior of a soft ferromagnet with narrow loops. Further it can be seen that magnetization did not saturate till the field of 1.5 T, which can possibly be due to the presence of AFM interactions in the austenitic phase. The value of magnetization at 1.5 T field increased slightly when x was changed from 0.24 (1.60 μ_B/ f.u.) to 0.28 (1.61 μ_B/ f.u.) and then fell for 0.32 (1.53 μ_B/ f.u.) and 0.36 (1.50 μ_B/ f.u.) sample. We also see that with increasing Al content the field at which magnetization reached maximum value increased, which can possibly be due to increase in magnetic anisotropy.

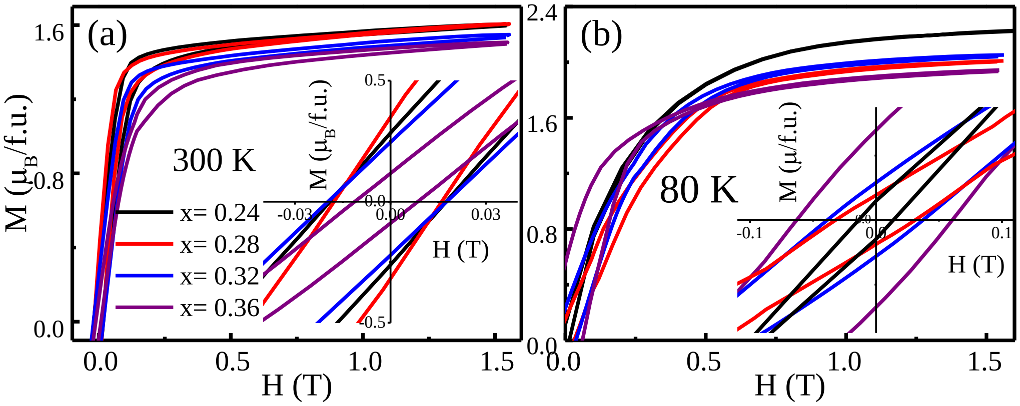

Figure 3.7 Isothermal magnetization measurements up to a maximum field of 1.5 T at (a) 300 K and (b) at 80 K. Insets show magnified view around the zero filed.

The drop in magnetization with increasing Al content can be explained in terms of ordering. As mentioned earlier in Section 3.1.1, with the increase in Al content in the system the amount of B2 phase increased. The amount of B2 phase was almost same for x = 0.24 and 0.28 and increased for x > 0.28 as inferred from XRD data. The B2 phase being disordered phase, with increasing Al content the fraction of AFM in the sample increased leading to drop in magnetization. The value of magnetization increased slightly when x changed from 0.24 to 0.28, which can be attributed to the fact that, though the B2 fraction remains almost same, the lattice parameter of x = 0.24 sample was slightly larger than x = 0.28 sample which might increase the strength of FM interaction in latter. The inset shows the magnified view of hysteresis curves around zero field. It can be seen that coercivity remained almost constant for samples till x = 0.32 and then fell for x = 0.36 sample. At 300 K as we saw in the thermomagnetic curve the bifurcation of ZFC and FC curve became small, except in case of x = 0.36 sample. This shows that in austenitic phase AFM interaction is stronger in x = 0.36 sample as compared to other samples.

The M-H curves were also obtained for the martensitic phase at 80 K and are shown in Figure 3.7 (b). It can be seen that in the martensitic phase sample was magnetically harder than austenitic phase. The magnetization at martensitic phase for x = 0.28 sample was slightly lower than x = 0.32 sample, so overall the magnetization fell as the Al content increased. The inset in Figure 3.7 (b) shows a magnified view at low field. The coercivity increased with Al content, thus the strength of AFM coupling decreased in martensitic phase. Thus we see that though the overall AFM fraction increased, AFM coupling strength decreased with increasing Al content in the martensitic phase. The AFM interaction which was strongest in the austenite phase in x = 0.32, upon MT becomes weakest among all the alloys of series.

3.1.5 Resistivity

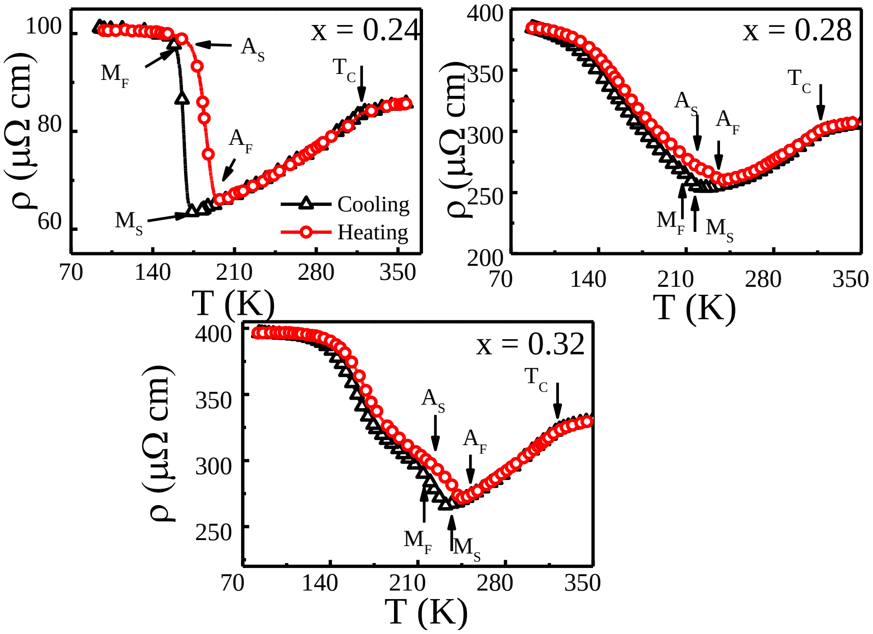

Figure 3.8 Resistivity measurements performed till 80 K in $Ni_2Mn_{1.36}Sn_{0.64-x}Al_x$ systems.

Resistivity measurements provide another tool to detect both structural and magnetic transitions. Temperature dependent resistance measurements were carried on the samples at the rate of 1 K/min in the temperature range of 80 to 400 K and the data are shown in Figure 3.8. The transition temperatures obtained from the DSC are marked in it. Resistance measurement could not be carried out for sample x = 0.36 as sample broke into smaller pieces when it was cooled below room temperature. We tried performing measurement at very slow rate but still sample broke when it was taken to low temperature.

In all samples around 330 K change in slope was observed which corresponded to the para to ferromagnetic transition of the austenitic phase. The steepening of slopes at the T_C can be attributed to the disappearance of electron-magnon scattering [94,95]. As temperature was further lowered the resistivity of x = 0.24 sample exhibited a sharp jump with hysteresis due to forward and reverse MT. The electrical resistivity in FM system is mostly dominated by the temperature dependent factors like lattice and magnetic contributions, caused by the electron-phonon scattering, and due to electron-magnon scattering respectively. In the Heusler compound the AFM interaction undergoes sharp change at phase transition. The antiferromagnet has a magnetic periodicity that can be different from the crystallographic periodicity. This leads to creation of new Brillouin zone boundaries (superzone boundaries) giving rise to gaps on the Fermi surface. The gap at Fermi surface leads to anomalous increase in resistivity as the conduction electron has to now overcome this gap [96]. There is also a temperature independent contribution due to lattice defects and chemical disorder, called residual resistivity. So the resistivity increased as a combined effect of AFM spin-correlations below MT and due to the electron-phonon scattering resulting from the increased interfacial scattering from various orientations of martensitic variants at the twin boundaries and the change in lattice symmetry as these alloys underwent martensitic transformation [59,96–98].

The resistivity of the x = 0.28 and 0.32 alloy did not show sharp rise in resistivity upon MT as in case of x = 0.24 sample. The resistivity of the sample changed largely in the vicinity of the structural transformation. In case of x = 0.28 alloy the resistivity increased below M_F till 110 K and the hysteresis continued till 80 K. Similar behavior was seen for x = 0.32 alloy where resistivity increases beyond M_F till 125 K and the hysteresis continued till 100 K. V K Sharma et. al reported similar behavior in Ni-Mn-Sn sample, but in that case susceptibility measurement showed irreversibility till lowest temperature of measurement whereas in this case susceptibility showed no irreversibility beyond the structural transformation temperature [99,100]. Thus we think that the increase in resistivity beyond MT in x = 0.28 and 0.32 could be occurring due to the increase in electron-magnon scattering. As the temperature was lowered AFM increased which might lead to increase of AFM spin-correlations, enhancing electron scattering. The irreversibility observed below the MT could be due to difference orientations of AFM-FM interfaces during heating and cooling.

3.2 Ni-Mn-Sb-Al System

3.2.1 XRD

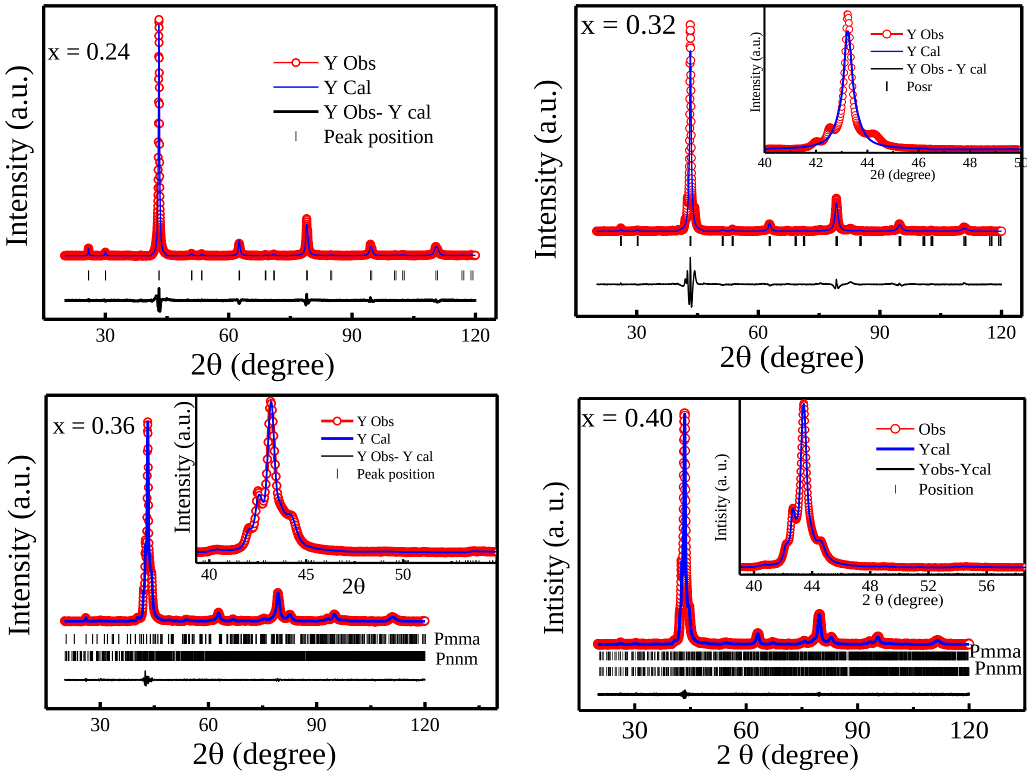

Figure 3.9 XRD patterns (Y Obs) of $Ni_2Mn_{1.36}Sb_{0.64-x}Al_x$ samples along with the, calculated patterns (Y Cal), differences between the observed patterns and calculated patterns (Y Obs – Y Cal) and peak positions fitted (vertical bar). Insets show magnified views of the main peaks.

Samples were prepared using the same procedure as mentioned for Ni-Mn-Sn-Al system, with compositions $Ni_2Mn_{1.36}Sb_{0.64-x}Al_x$ (where x = 0.24, 0.28, 0.32, 0.36 and 0.40).

Annealing was carried out at 1173 K in evacuated quartz tubes and then quenched in ice water [101]. Composition was confirmed using EDAX. The sample x = 0.28 was not homogeneous thus no more measurement were performed on it.

The XRD values obtained at room temperature for x = 0.24, 0.32, 0.36 and 0.40 are shown in Figure 3.9. The data were analyzed using profile matching tool of FullProf program. Observed patterns (Y Obs), calculated patterns (Y Cal), differences between the observed and calculated patterns (Y Obs – Y Cal) and peak position are marked in Figure 3.9 for all samples. The x = 0.24 sample was indexed to $L2_1$ phase at room temperature [100] and the lattice parameters obtained are given in Table 3-2. The superlattice peaks [1 1 1] and [3 1 1] were present showing that presence of Al did not bring significant amount of B2 phase in the system. As the Al content increased towards x = 0.32 X-ray pattern showed additional peak around the principal [2 2 0] satellite peak of $L2_1$ phase, as shows in inset of Figure 3.9. These are weak reflections corresponding to the martensitic phase. This shows that both martensitic and austenitic phases coexist in the sample at 300 K. The curve was fitted with the $L2_1$ structure but the peak corresponding to the martensitic phase was weak and fitting for it could not be performed.

The samples with x = 0.36 and 0.40 were indexed at room temperature to be in martensitic phase. The peaks were fitted with the profile for orthorhombic structure. Initially orthorhombic 4 layered structure (4O), with space group *Pmma*, was considered for fitted but it could not account for all peaks observed [67,102]. All peaks were accounted for when additional orthorhombic group with seven fold modulation, having space group *Pnnm*, was included in the fitting [24,103]. This shows that the martensitic phase was a mixture of two types of orthorhombic structures. The magnified view of the main peak and fitted curve are shown in the inset of the respective Figure 3.9.

All lattice parameters obtained are given in Table 3-2. The cell volumes for the smallest cells are also given. It can be seen that with increase in Al content the $L2_1$ lattice parameters fell. The cell volume fell as the Al content increased, but it increased for the sample with composition x = 0.40.

Table 3-2 The structure type and lattice parameters (nm) along with the lattice volumes for the $Ni_2Mn_{1.36}Sb_{0.64-x}Al_x$ system.

X	Structure	a (nm)	b (nm)	c (nm)	v (nm^3)
0.24	$L2_1$	0.593	0.593	0.593	0.2086
0.28	-	-	-	-	-
0.32	$L2_1$ + martensite	0.592	0.592	0.592	0.2076
0.36	4O + 7 M	0.433	0.558	0.858	0.2073
		0.437	3.877	0.855	1.4490
0.40	4O + 7 M	0.438	0.557	0.858	0.2093
		0.436	3.875	0.854	1.4430

3.2.2 DSC

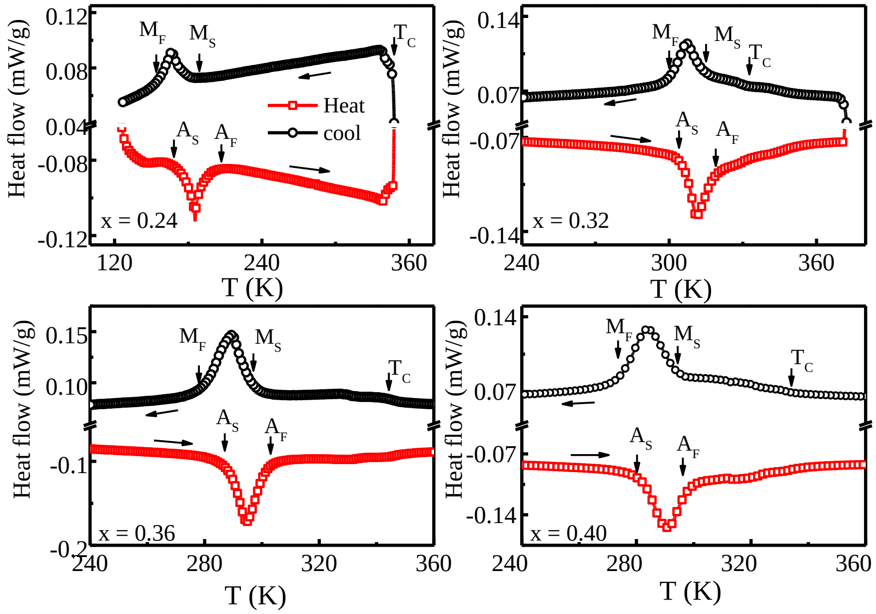

Figure 3.10 DSC curves obtained for $Ni_2Mn_{1.36}Sb_{0.64-x}Al_x$ samples during heating and cooling runs.

Differential scanning calorimetric measurements were performed in the same way as mentioned in the Section 3.1.2 and the obtained curves are shown in the Figure 3.10. All samples showed exothermic and endothermic peaks during cooling and heating cycles confirming that samples underwent structural transformation. The obtained transformation temperatures are given in Table 3-3 and are marked in the Figure 3.10 by vertical arrows. The Curie temperatures (T_C) could not be determined from the DSC curve as the change in slope at magnetic transition was small here. We have also marked T_Cs which were obtained from magnetic measurements.

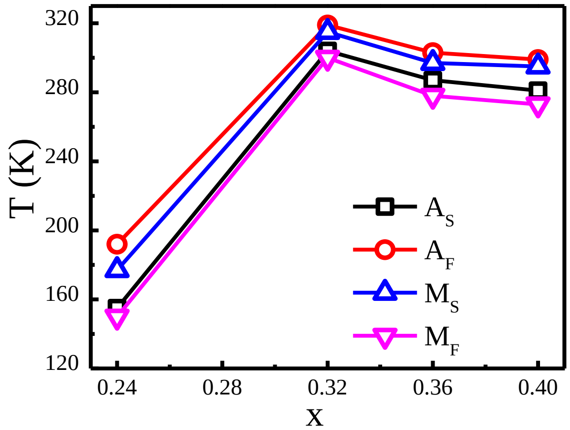

Figure 3.11 The characteristic transition temperature, martensitic start (M_S), martensitic finish (M_F), austenitic start (A_S) and austenitic finish (A_F) as a function of Al concentration for $Ni_2Mn_{1.36}Sb_{0.64-x}Al_x$.

The transformation temperatures obtained are also plotted against the Al content in Figure 3.11. It can be seen that transformation temperatures increased by more than 100 K when Al content increased from 0.24 to 0.32, but these fell slightly with the increasing Al content. This can happen due to competing effect between decreasing e/a ratio (decreases MT temperature) and the cell contraction (increases MT temperature). Initially the decreasing lattice parameter effect dominates over the e/a effect, thus the transformation temperature increased when concentration increased from 0.24 to 0.32. The fall in MT temperature with increasing x content beyond 0.32 was most probably due to domination of the effect of e/a ratio over the effect of cell contraction.

3.2.3 AC susceptibility

Susceptibility measurements were performed on the samples from 370 K to 80 K at a frequency of 111 Hz, the data are shown in the Figure 3.12. The behavior of the x = 0.24 system was similar to the system mentioned in Section 3.1.3. In all samples the $\chi^/$

increased abruptly around 350 K, the T_Cs of the systems, which are given in Table 3-3. It can be seen that unlike Ni-Mn-Sn-Al system the variation in the T_C with concentration is large and random.

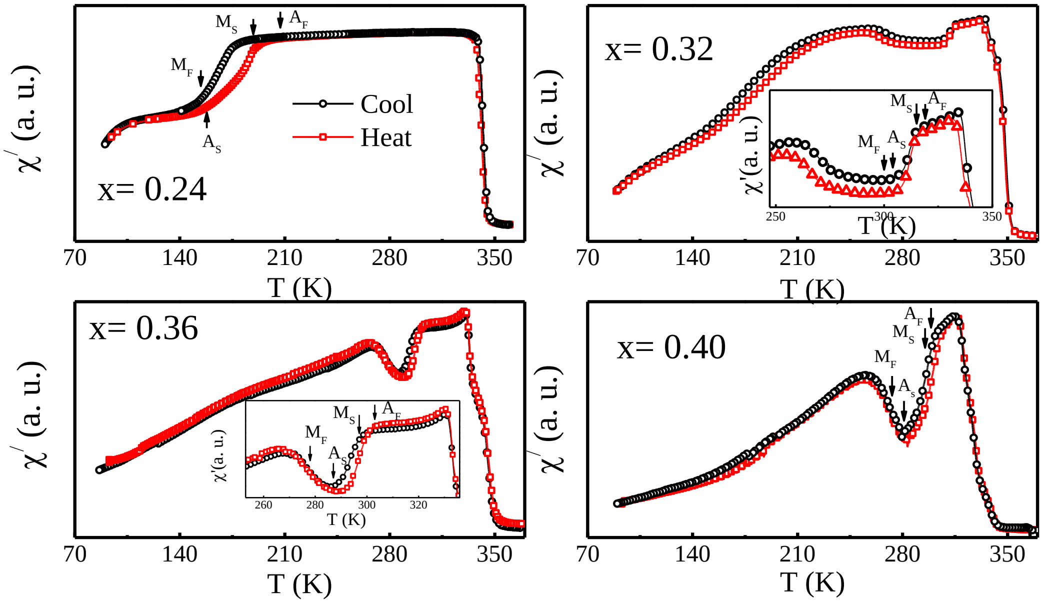

Figure 3.12 Real part ($\chi^{/}$) of ac susceptibility measurement performed at 111 Hz during heating and cooling runs for $Ni_2Mn_{1.36}Sb_{0.64-x}Al_x$. The structural transformation temperatures are marked. Insets in x = 0.32 and 0.36 show magnified views around the transformations.

The transition temperatures obtained from the DSC curves are marked in the Figure 3.12. It can be seen that as temperature was lowered the $\chi^{/}$ dropped at the M_S for all samples. The $\chi^{/}$ rose for samples with x = 0.36 and 0.40 before martensitic transition was complete. Similar behavior has been reported in $Ni_2Mn_{1.64}In_{0.36}$ system [99]. Martensitic and austenitic phases have different lattice parameters and different symmetries. Also the magnetic character of the martensitic phase was different from the austenitic phase as discussed in the Section 1.3.3. So the T_C in both phases are different [15,104]. As the sample was cooled below the M_F, it started to transform to the martensitic phase with lower magnetization resulting in drop in magnetization. As temperature was further lowered, the martensitic phase underwent paramagnetic to ferromagnetic transition, which resulted in increase of the $\chi^{/}$, as with decreasing temperature more of the martensitic phase transformed to ferromagnetic martensitic. This resulted in increase in $\chi^{/}$ before the MT was completed. As samples were further cooled below M_F, $\chi^{/}$ showed peak like feature which was present in all sample except x = 0.24. The peak appeared in both cooling and heating cycles at same temperature, thus ruling out possibility of intermartensitic transformation [105]. Also DSC curve showed no change in the temperature region corresponding to the peak in $\chi^{/}$. Thus the peak appeared most probably due to freezing of magnetic moments or AFM transition. The detail of the origin of peak has been discussed in a latter chapter. While heating the sample the $\chi^{/}$ started to rise at A_S, this happened because austenitic phase was predominantly ferromagnetic in nature, so as sample transformed to austenitic phase the ferromagnetic phase increased, thus $\chi^{/}$ increased.

3.2.4 DC magnetic measurement

3.2.4.1 Temperature dependent dc magnetic measurement

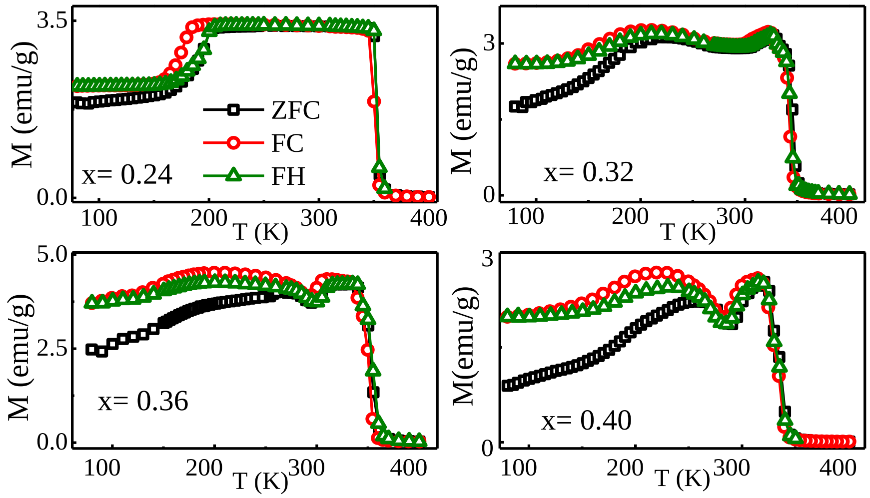

Figure 3.13 M-T curves measured in ZFC, FC and FH protocol in VSM in the field of 100 Oe in $Ni_2Mn_{1.36}Sb_{0.64-x}Al_x$.

DC magnetization measurements were carried out using the same protocol as mentioned in the Section 3.1.4 from 80 K to 400 K in the applied field of 100 Oe as shown in Figure 3.13. The curves obtained have behaviors similar to the $\chi^{/}$ measurements of the corresponding samples. In the low temperature region below M_F samples displayed irreversibility which shows that the various magnetic moments in the sample got pinned down in different configurations depending on how sample was heated or cooled in presence of magnetic field [106].

3.2.4.2 Isothermal magnetic measurements

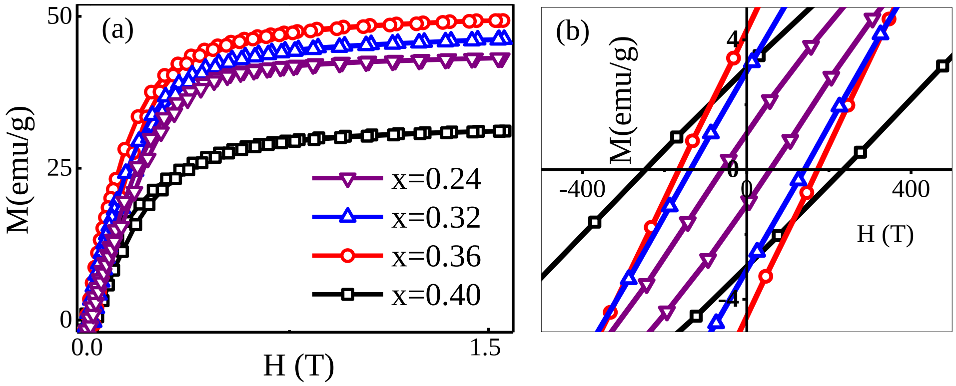

Figure 3.14 (a) Isothermal magnetization measurements for $Ni_2Mn_{1.36}Sb_{0.64-x}Al_x$ till maximum field of 1.5 T at 80 K, (b) magnified view around the zero field.

The Isothermal magnetization measurements were performed on the samples at 80 K, till the field of 1.5 T as shown in the Figure 3.14 (a). We find that magnetization of the martensitic phase at 80 K initially increased when x was changed from 0.24 to 0.36 and then fell for the x = 0.40 sample. The Figure 3.14 (b) shows the magnified view of the hysteresis curves in the low field region. We see that the coercivity in the sample increased as the Al content in the sample increased. This shows that AFM interaction in the sample became weaker with increasing Al content. Similar comparison could not be performed for the austenitic phase as the A_S temperature was close to T_C, thus there was no common temperature at which we could be certain that all samples were fully in austenitic phase.

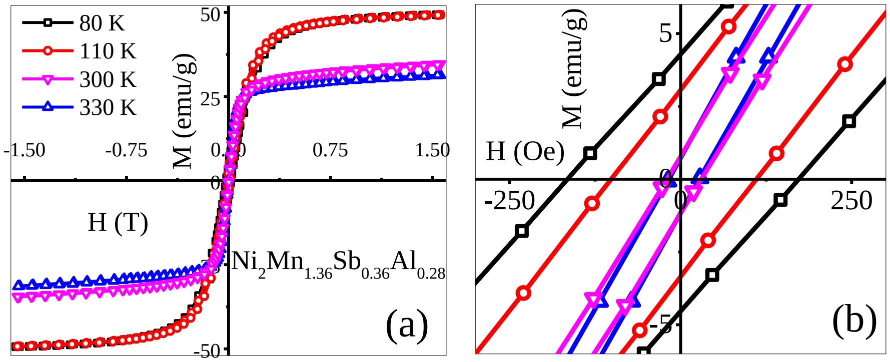

Figure 3.15 (a) Isothermal magnetic curves measured at various temperatures till the field of 1.5 T, (b) magnified view near zero field.

Isothermal M-H curves were also measured at various temperatures for all four samples, the curve obtained for sample with x = 0.36 is shown in the Figure 3.15 (a). Similar curve were also obtained for other compositions but are not shown here. Magnetization of the austenitic phase at high field was lower than the martensitic phase at low temperature. Across the MT the magnetization fell initially for the martensitic phases. Figure 3.15 (b) shows the magnified view in low field regions, we see that martensitic phase is harder magnetically than the austenitic phase.

Table 3-3 Various parameters obtained are given here. The martensitic start (M_S), martensitic finish (M_F), austenitic start (A_S), austenitic finish (A_F) and Curie Temperature (T_C) for $Ni_2Mn_{1.36}Sb_{0.64-x}Al_x$ systems.

x	M_S (K)	M_F (K)	A_S (K)	A_F (K)	T_C (K)
0.24	189	154	158	207	355
0.32	315	300	304	319	348
0.36	297	278	287	303	360
0.40	295	273	281	299	342

3.3 Ni-Mn-In-Al system

3.3.1 XRD and DSC

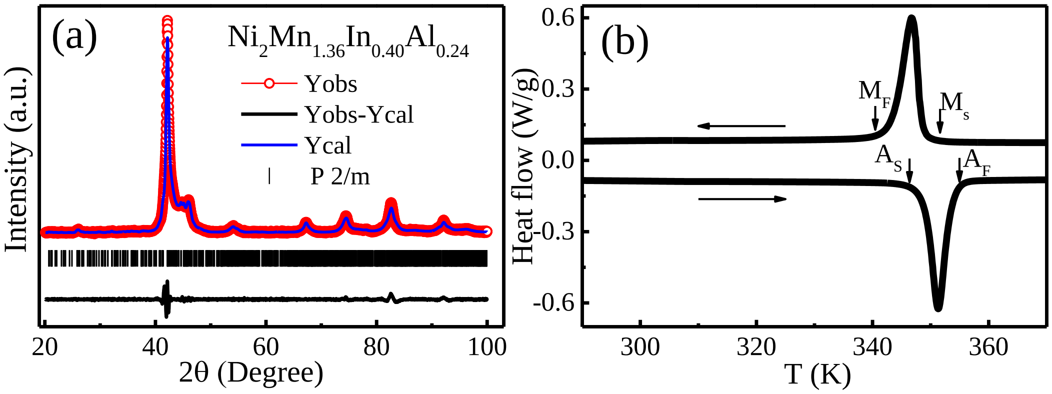

Figure 3.16 (a) XRD pattern obtained at 300 K along with calculated pattern, residue and peak position. (b) DSC curve of the sample in heating and cooling runs.

A sample with composition $Ni_2Mn_{1.36}In_{0.40}Al_{0.24}$ was prepared as mentioned before and annealing was carried out at 1173 K in the evacuated quartz tube and then quenched in ice water. XRD was measured at room temperature on the powdered sample, observed pattern (Y Obs) is shown in the Figure 3.16 (a). The observed pattern was fitted with a pattern for orthorhombic 14 M structure with *P2/m* space group [107,108]. The calculated pattern (Y Cal), difference between the observed pattern and calculated pattern (Y Obs – Y Cal) and peak position are marked in Figure 3.16 (a). The lattice parameters obtained after refinement were a = 0.428 nm, b = 0.580 nm, c = 0.300 nm and β = 93.0°. The values agree with the previous measurements on the In based system [21,109].

Figure 3.16 (b) shows DSC measurement performed on the sample. It was found that the sample had M_S, M_F, A_S and A_F transitions at 350 K, 339 K, 345 K and 356 K respectively and small peaks were observed just above 300 K which came most probably form the intermartensitic transitions in the sample. The peak corresponding to the intermartensitic phase was very small, thus showing very small fraction of sample underwent intermartensitic transition. In a sample with composition $Ni_2Mn_{1.36}In_{0.64}$ the martensitic transformation occurred at 265 K (martensitic start temperature) [110,111], thus showing that the substitution of Al in place of In has resulted in the enhancement of the structural transformation temperatures as in case of Sn and Sb systems.

3.3.2 AC susceptibility

The real part ($\chi^/$) ac susceptibility measurements performed on the sample is shown in Figure 3.17 (a). As temperature was lowered $\chi^/$ increased at 320 K, which was most probably the Curie temperature of intermartensitic phase of the system. Below T_C hysteresis is observed which occurs due to intermartensitic transformation in the system. As the temperature was lowered the peak fell, which shows that upon subsequent martensitic transition the sample transformed to paramagnetic martensitic. To further confirm that above peak occurs due to intermartensitic transformation temperature depended XRD has to be performed. In the low temperature region a large peak is observed in $\chi^/$ measurement. Similar peak has been observed in the ac susceptibility measurement in $Ni_2Mn_{1.40}In_{0.60}$ sample, where it was shown to be outcome of competing FM/AFM interaction and was not of spin glass in nature [112]. There are also reports on the In based system where the appearance of similar peak has been observed and it has been associated with the spin glass freezing [113]. We were not able to determine the intermartensitic transformation temperatures from the $\chi^{/}$ or DSC measurements as change in nature of curve was very small.

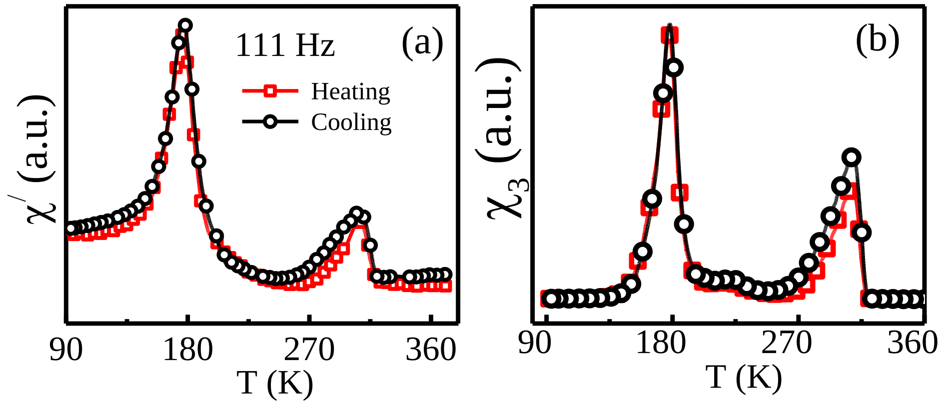

Figure 3.17 a) shows the real part of ac susceptibility measurement performed on the $Ni_2Mn_{1.36}In_{0.40}Al_{0.24}$ sample in heating and cooling cycle at the frequency of 111 Hz. b) shows third harmonic of ac susceptibility obtained during same run.

We have also performed third harmonic measurement of on the sample and its magnitude (χ_3) is shown in the shown the Figure 3.17 (b). We see that the nature of the curve is similar to the $\chi^{/}$. In between 200 K and 240 K a small bump is observed in both heating and cooling curves of χ_3 which can possibly be due to completion of intermartensitic structural transformation.

3.3.3 DC magnetization

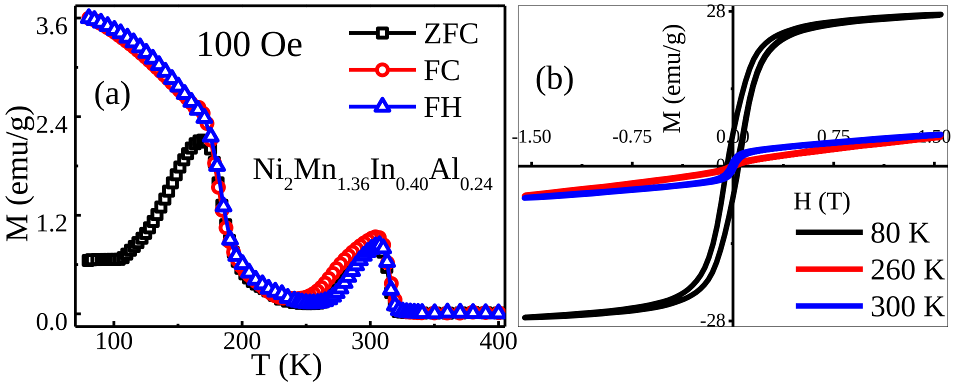

Figure 3.18 (a) ZFC, FC and FH measurement performed on In system as function of temperature in the field of 100 Oe. (b) Isothermal magnetic curve measured at various temperatures till the field of 1.5T.

Thermomagnetization measurements were performed on the sample as shown in the Figure 3.18 (a). The curves are similar to the ac susceptibility measurement. Thermal hysteresis was observed just below T_C of intermartensitic transition which confirms first order nature of transition. The magnetization below the T_C of intermartensitic transition was very small which can possibly be due to small fractions of remnant intermartensitic phase. As temperature was lowered further we see that magnetization fell till 253 K in the FC curve which was most probably the temperature at which intermartensitic phase transformed to martensitic phase completely. Afterwards, it rose in the ZFC and FH curves at around 265 K which was most probably the temperature at which reverse intermartensitic transformation took place. As the sample was warmed up the magnetization began to fall at T_C of intermartensitic phase before the transformation was complete, thus we were not able to determine other two temperatures of intermartensitic phase. Furthermore, as the sample was weekly magnetic around the intermartensitic transformation the proper estimation of transformation temperature is only possible from DSC measurement, but very small peak prevents us from estimating them. In the low temperature region magnetization rose at 230 K which is T_C of the martensitic phase [110,114]. As temperature was further lowered the ZFC-FC curves bifurcated which has been attributed to the mixed FM/AFM interaction and has been discussed in a greater detail in the latter chapters.

Isothermal M-H measurements were performed on the sample at the temperatures of 80 K, 260 K and 300 K as shown in the Figure 3.18 (b). At 80 K sample displayed a typical behavior of ferromagnetic sample, the M-H loop did not saturate even at higher field showing that AFM interaction was also present in the sample. At the temperature of 260 K sample was in the paramagnetic state as seen in the M (T) curve and it displayed behavior typical of it. While at 300 K sample was most probably in intermartensitic phase, with weak FM character and dominating paramagnetic behavior as evident from M-H curve.

3.4 Discussion

We have replaced Al in the three main Ni-Mn-Z based FSMA systems with Z as Sn, Sb and In. We see that the even when Z was replaced with a large percentage of Al, samples still displayed the FSMA properties.

The substitution of Al in Sn based system led to increase in undesirable B2 phase with increase in Al content, while the lattice parameter of the austenitic phase decreased, obeying Vegard’s law of substitution. The substitution also shifted the transformation temperatures towards the room temperature with increasing Al content. The substitution also has profound effect on the magnetism of the austenitic phase of the sample. The magnetization of the sample was found to decrease with increasing Al content. AC susceptibility measurement and dc thermomagnetization measurement showed that with increase in Al content in the sample the AFM interaction also increased. This is expected trend as the B2 phase in the system increased the disorder increased and more and more of Mn atom occupied the Z site leading to increase in the fraction of AFM phase.

The substitution of Al in Sb based system initially shifted the structural transformation temperature towards room temperature, but the effect was levelled off at higher concentration of Al and the transition temperature did not show much shift. The effect of substitution on the lattice parameter and magnetism of the austenitic phase could not be determined due to limitation of XRD setup and the narrow range at which the austenitic phase exists at higher Al concentration.

The substitution of Al in In based system was done only for x = 0.24 of Al. The structural transformation temperatures were found to be above room temperature. The weak magnetic transition in the sample occurs around room temperature most probably due to intermartensitic transformation.

In next chapter we shall look into the functional properties of these systems and also explore the way to overcome the unwanted B2 phase in the Sn based system at higher Al content.

Chapter 4

Functional properties of Ni-Mn-Sn and Ni-Mn-Sb alloy

In this chapter we shall explore the functional capabilities of the systems we have prepared. We shall analyze the effect the substitution has on the properties like magnetocaloric effect and exchange bias effect. The possibilities of developing a single system which can serve multiple purposes are of interest in this chapter. While the magnetocaloric effect holds promise of a cleaner, safer and more compact refrigerant, properties like exchange bias effect hold possibility in applications in many spintronic devices such as spin valves, read heads and nonvolatile memory.

The main force driving the study of Ni-Mn based FSMA is their ability to show multifunctional properties in one system, like large inverse magnetocaloric effect, barocaloric effect and large magnetoresistance to name a few [36,37,115–117]. These properties are the outcomes of strong coupling between crystal structure and magnetism. The system further becomes interesting because of the fact that the temperature at which they display these multifunctional capabilities can be easily varied and controlled by changing the composition, as discussed in the Chapter 1. These systems are also known to display exchange bias effect (EB) in the low temperature region which is outcome of competing AFM/FM interaction [118]. These systems hold promise of being capable of delivering more ecofriendly and energy efficient solid state refrigerant along with possibility of industrial applications in magnetoresistive reading heads and similar elements. We shall explore in details the properties like MCE and EB-effect in the present chapter, while the MR while be discussed in the latter chapter.

4.1 Magnetocaloric effect (MCE)

When the magnetization of any magnetic material is changed isothermally under application of a magnetic field, heat is exchanged with the surroundings. If the change was performed adiabatically, the temperature will change. This is the magnetocaloric effect which provides the basis of the adiabatic demagnetization cooling technique [119,120].

A conventional refrigerator works on vapor compression cycle. It is one of the most common refrigerating techniques available because of its advantages like high efficiency, low toxicity, low cost and simple mechanical embodiments, but it suffers from disadvantage of being non environmental friendly.

Magnetic refrigeration based on the MCE, has recently received increased attention as an alternative to these. Magnetic materials contain two energy reservoirs; the usual phonon excitations connected to lattice degrees of freedom and magnetic excitations connected to spin degrees of freedom [121,122]. In FSMA these two reservoirs are strongly coupled due to enhanced spin lattice coupling whereby a magnetic field can induce a change in magnetic and lattice entropies simultaneously, resulting in a large magnetocaloric effect.

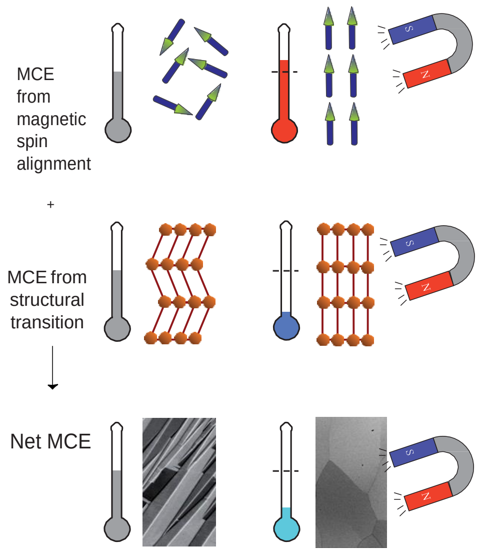

Figure 4.1 Magnetic alignment due adiabatic magnetization results in the sample heating up (top row); whereas simultaneous structural transition to higher magnetic austenitic phase from low-magnetization and twinned martensitic phase leads to a very large cooling effect (middle row). Addition of these opposite contributions results in a net cooling of the sample (bottom row) [122].

In Ni-Mn based FSMA the change in magnetization from lower magnetic martensitic phase to the higher magnetic austenitic phase brings about changes in entropy resulting in heating of the magnetic material. This is shown schematically in the Figure 4.1. On the other hand the structural transformation from a low-magnetization twinned martensitic phase to high magnetization and high symmetry austenitic phase leads to heat absorption which exceeds magnetic heat released by a large amount, giving rise to net cooling effect. As the sample cools when it is magnetized, this is referred as inverse magnetocaloric effect [123].

The MCE can be measured directly as the temperature change $\Delta T_{ad}(T)_{\Delta H}$ of sample when magnetic field is applied adiabatically. Temperature is measured initially in the zero field ($H_I = 0$) on a demagnetized sample and again after application of a field ($H_F = H$). The difference in temperature gives the value of temperature change for a given field change ($\Delta H = H_I - H_F$). The MCE can also be measured indirectly as $\Delta T_{ad}(T)_{\Delta H}$ or as isothermal magnetic entropy change $\Delta S_M(T)_{\Delta H}$ from the heat capacity measurement as a function of temperature and field or form the isothermal magnetic measurements performed at different temperatures as a function of field. $\Delta T_{ad}(T)_{\Delta H}$ and $\Delta S_M(T)_{\Delta H}$ are both measure of MCE and are related to total entropy of the system as shown in the Figure 4.2 (a). It is thus possible to calculate one from another with certain given parameters [124,125].

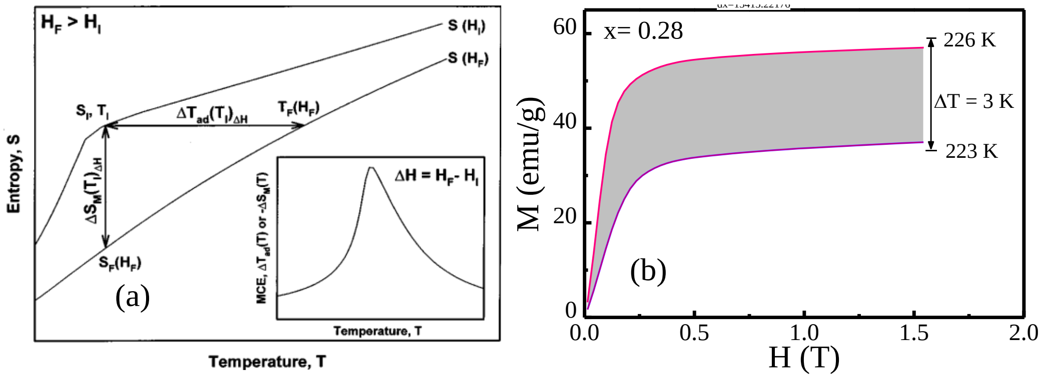

Figure 4.2 a) Magnetocaloric effect as the adiabatic temperature rise, $\Delta T_{ad}(T_I)\Delta H$, and the magnetic entropy change, $\Delta S_M(T_I)\Delta H$ shown for a given initial temperature T_I and a given magnetic-field change $\Delta H = H_F - H_I$ in a ferromagnetic material. The inset displays MCE typical for a ferromagnet as a function of temperature [124]. b) Magnetization (M) vs. magnetic field (H) curves at constant temperatures T (223 K) and T+ΔT (226 K) measured for $Ni_2Mn_{1.36}Sn_{0.36}\,Al_{0.28}$ across martensitic transition. The area between the two curves divided by the temperature difference ΔT estimates the isothermal magnetic ΔS_M at (T + ½ ΔT) according to equation (4-3).

The modified Maxwell relation for the magnetic system is given as [119,124]

$$\left(\frac{\partial S_M\,(T,H)}{\partial H}\right)_T = \left(\frac{\partial M\,(T,H)}{\partial T}\right)_H, \tag{4-1}$$

which shows the relation between magnetization (M), magnetic-field strength (H) and absolute temperature (T). For isothermal-isobaric process this yields

$$\Delta S_M = \int_0^H \left(\frac{\partial M}{\partial T}\right)_H dH. \tag{4-2}$$

For magnetizations measured isothermally at discrete temperature intervals, the above equation can be approximately written as

$$\Delta S_M\left(T + \frac{\Delta T}{2}\right) \approx \frac{1}{\Delta T}\left[\int_0^H M(T + \Delta T)\,dH - \int_0^H M(T)\,dH\right], \tag{4-3}$$

thus ΔS_M can be calculated for any T by numerically integrating the experimentally measured magnetizations as the function of temperature and magnetic field. The use of above equation is equivalent to evaluating the area enclosed between two magnetic isotherms measured at close temperature interval, as shown in Figure 4.2 (b), and after dividing by the temperature change.

In Heusler alloys the first order phase transition in general shows a magnetic irreversibility because of the presence of mixed magnetic phase. Since Maxwell relation can be used only under equilibrium conditions, estimation of ΔS_M from isothermal M-H curves can thus result in erroneous estimate. It is thus important that one performs direct measurements to properly estimate the MCE in the FSMA.

We have performed direct measurement of entropy change in one of the systems using a purpose-built high sensitivity differential scanning calorimeter, under zero and applied magnetic field, as described in section 2.3.3 and Ref. [77]. The entropy change calculated from the calorimetric measurement as a function of temperature in the constant magnetic field provides the complete characterization of MCE in solid magnetic materials. The entropy of the transformation has been calculated from the measured calorimetric curves at constant field, after a proper baseline correction, using the following expression

$$S(H,T) = \int_{T_0}^{T} \frac{1}{T}\left(\frac{dQ}{dT}\right) dT, \qquad (4\text{-}4)$$

where *dQ/dT = (dQ/dt)/(dT/dt),*with *dQ/dt* being a measure of heat flux and T_0 is the martensite start and austenite start temperatures for cooling and heating runs, respectively [126–128]. The entropy change accounting for MCE, when the magnetic field increases from 0 to H at a constant temperature is then given by

$$\Delta S_M(\mathrm{T,H}) = \mathrm{S(T,H)} - \mathrm{S(T,H} = 0). \qquad (4\text{-}5)$$

4.1.1 MCE in Ni-Mn-Sn-Al system

The Ni-Mn-Sn system shows giant magnetocaloric effect. The parent composition of $Ni_2Mn_{1.36}Sn_{0.64}$ sample showed maximum value ΔS_M of 5 J $Kg^{-1}K^{-1}$ in the field of 2 T [129]. When the Sn in the system was replaced with Ge, it was found that MCE in the system could be tuned [130].There are also study of the effect of the replacement of the Ni and Mn in the system with Fe, Cu and Co [131–133]. The substitution of Co in Mn position offered the highest MCE in the system with the value of ΔS_M of 22.9 J $Kg^{-1}K^{-1}$ in the field of 2 T [133]. We here study the effect of Al replacement on the MCE in the Ni-Mn-Sn system.

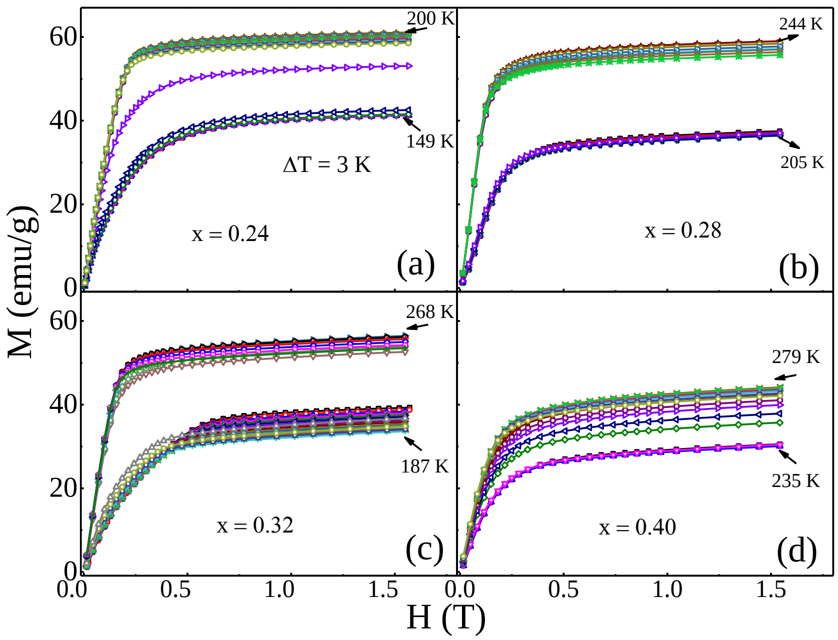

Figure 4.3 M-H curves at the temperature interval of 3K in the heating sequence for the samples $Ni_2Mn_{1.36}Sn_{0.64-x}Al_x$. To make comparison of different samples easier, we have kept the M and H scale same in all the graphs and marked lowest and highest temperatures of measurement.

The isothermal magnetizations (M-H) were measured at various temperatures around MT up to a field of 1.5 T, as shown in the Figure 4.3. These measurements were performed in the heating sequence, starting from temperatures below austenitic start temperatures. To avoid influence of any austenitic phase, samples were cooled in zero field below their martensitic finish temperatures. It was found that in all cases the samples magnetization increased abruptly around MT as the samples were heated. This happened because sample transformed from the weak magnetic martensitic phase to predominantly ferromagnetic austenitic phase. It can be seen from the Figure 4.3 that as the Al content in sample increased the magnetization of high temperature phase (austenitic) fell, which is in agreement with the previous measurements performed in the Chapter 3. Further it can be seen that with increase in the Al the change in magnetization (ΔM) across MT also decreased and occurred less abruptly, presumably due to disorder driven broadening of the first order phase transition [98,134].

The MCE in the Ni-Mn based Heusler alloys originates from two main contributions: (i) the coupling controlled by high uniaxial magnetic anisotropy of the martensitic phase, which takes place at mesoscopic length scale of martensite variants and magnetic domains, and (ii) the intrinsic microscopic coupling related to the change of magnetic moment induced by the change of symmetry which occurs at the transition [15,135]. The change in anisotropy and large ΔM across martensitic transition results in a large magnetocaloric effect in this system.

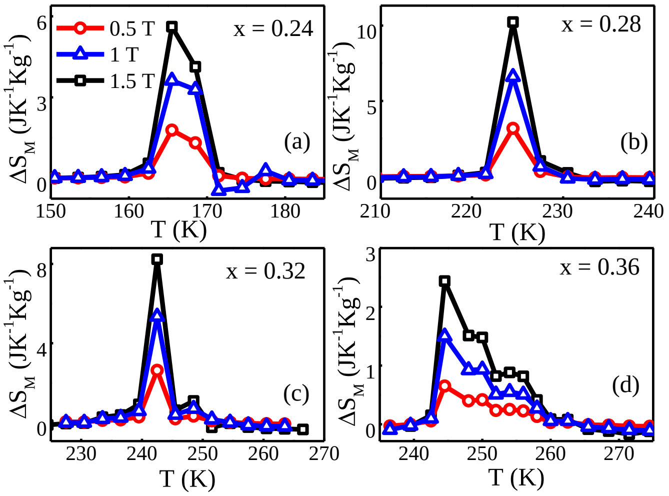

Figure 4.4 Shows the ΔS_M evaluated for 0.5 T, 1 T and 1.5 T for the various values of x in $Ni_2Mn_{1.36}Sn_{0.64-x}Al_x$.

The value of ΔS_M was obtained, using equation (4-3) on the magnetization data and are shown in Figure 4.4. The ΔS_M was evaluated for 0.5 T, 1 T and 1.5 T for various values of x in $Ni_2Mn_{1.36}Sn_{0.64-x}Al_x$.The low field ΔS_M measurements showed that in all samples magnetic anisotropy changed, occurring due to twin formation and reorientation process across the MT leading to inverse MCE. As the field increased the inverse MCE also increased in all samples. The increase in MCE at higher field stemmed from the Zeeman energy resulting due to difference in saturation magnetization of the transforming phase.

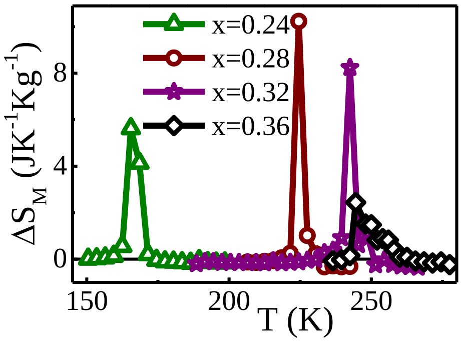

Figure 4.5 Entropy changes due to application of field of 1.5 T in $Ni_2Mn_{1.36}Sn_{0.64-x}$ Al_x samples.

The Figure 4.5 shows ΔS_M in the field of 1.5 T for all four systems. The maximum value of MCE was found to be 5.6, 10.2, 8.2 and 2.4 J kg^{-1} K^{-1} respectively, for x= 0.24 to 0.36 samples. So substitution of Al not only enhanced the MCE initially, but also moved the maximum value of ΔS_M towards room temperature. Another important parameter to evaluate the magnetocaloric material is its refrigerant capacity (RC). RC is the amount of heat transferred in a single thermodynamic cycle from the cold end at T_1 to the hot end at T_2 and it is calculated by integrating ΔS_M–T curve over the full width at half maxima using the relation $RC = \int_{T_1}^{T_2} \Delta S_M (T)_H \, dT$. Obtained values of RC for the field of 1.5 T are 25.2, 24.6, 20.5 and 12.9 J kg^{-1} respectively, for x= 0.24 to 0.36. It can be seen that even though the maximum of ΔS_M increased first and then dropped, the RC decreased with increase in x. It has been shown that a large adiabatic temperature change is obtained in these materials when the ΔM is large across the structural transformation [1]. The ΔM was found to be 19.5 emu/g, 20 emu/g, 15.5 emu/g and 14 emu/g for x= 0.24 to 0.36 samples, following trend similar to the ΔS_M. The reason for the drop in MCE across transformation with the increase in Al content is probably due to the amount of antiferromagnetic B2 increasing into the system at the expense of ferromagnetic $L2_1$, as inferred from the XRD and magnetization measurement in the Section 3.1.

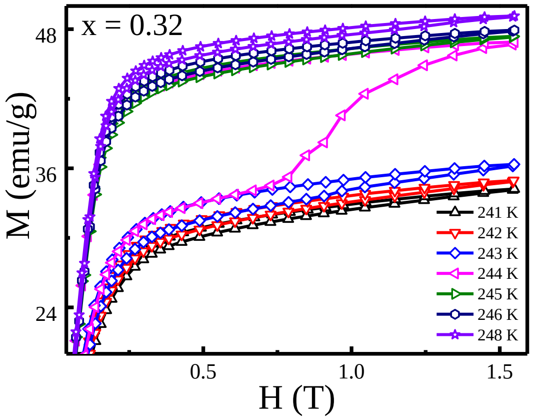

Figure 4.6 M-H measurement performed at the temperature interval of 1 K around MT to observe field induced austenitic transformation in $Ni_2Mn_{1.36}Sn_{0.32}Al_{0.32}$.

We observed in Figure 4.3 that magnetization changed abruptly at MT. It was steeper in case of x = 0.28 and 0.32 system, where the changes were 20 emu/g and 15.5 emu/g respectively in the temperature window of 3 K. There is a possibility that at intermediate temperatures, the system may undergo metamagnetic transformation, from lower magnetic martensitic phase to higher magnetic austenitic phase [55,136,137]. Thus we performed M-H measurement for x = 0.32 sample at a temperature interval of 1K in both magnetizing and demagnetizing cycles as shown in Figure 4.6. We see that as the temperature increased beyond 241 K the hysteresis increased in the samples becoming maximum for M-H at 244 K where sample underwent metamagnetic transition to austenitic phase. After that hysteresis again decreased as temperature was further increased. Such phase coexistence led to large hysteresis at transformation which may lead to overestimation of ΔS_M when Maxwell relation is used [104,138–140]. However, there are also reports where the MCE measured from magnetization measurement agrees with calorimetric measurements [123,126,127]. The large sudden jump in ΔS_M at the transition can also come from overestimation of entropy change form magnetization data. Thus to cross-check the ΔS_M estimated from the magnetization measurement we performed calorimetric measurement to estimate ΔS_M directly in x = 0.32 sample.

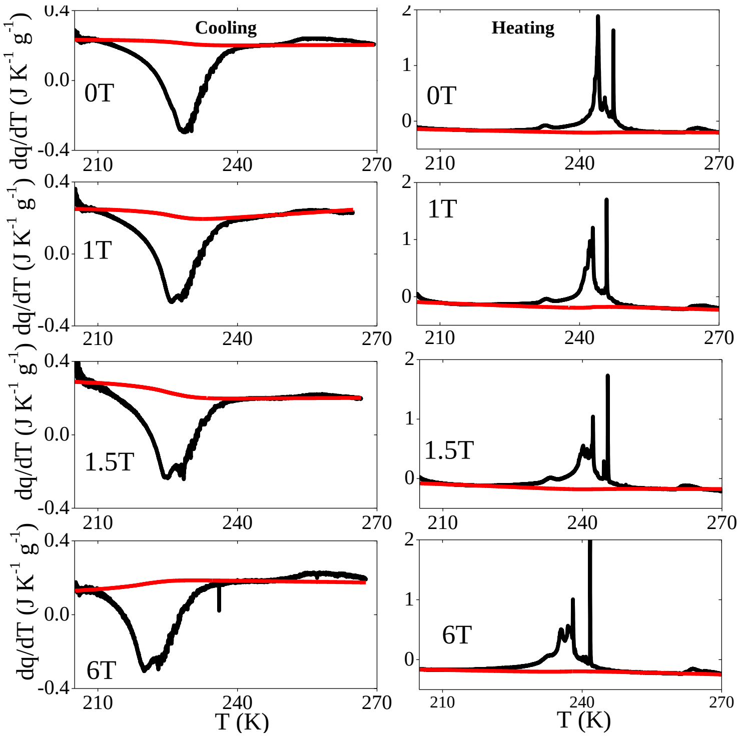

Figure 4.7 Calorimetric curves recorded on cooling (left panels) and heating (right panels) runs at selected values of the magnetic field in $Ni_2Mn_{1.36}Sn_{0.32}Al_{0.32}$.

Isofield calorimetric measurements were performed on the sample in the zero field and fields of 1, 1.5 and 6 T in both heating and cooling runs in the vicinity of structural transformations. The sample was first brought to a low temperature where the sample was fully in martensite phase, and a magnetic field was applied. The field was kept constant, while the temperature was swept at a rate 0.45 K/min. Upon completion of the thermal cycle, the field was increased and the sample was thermally cycled again through the martensitic transition. The thermal curves obtained from these measurements are shown in Figure 4.7, where negative values correspond to the exothermal forward martensitic transition and positive values to the endothermal reverse transition.

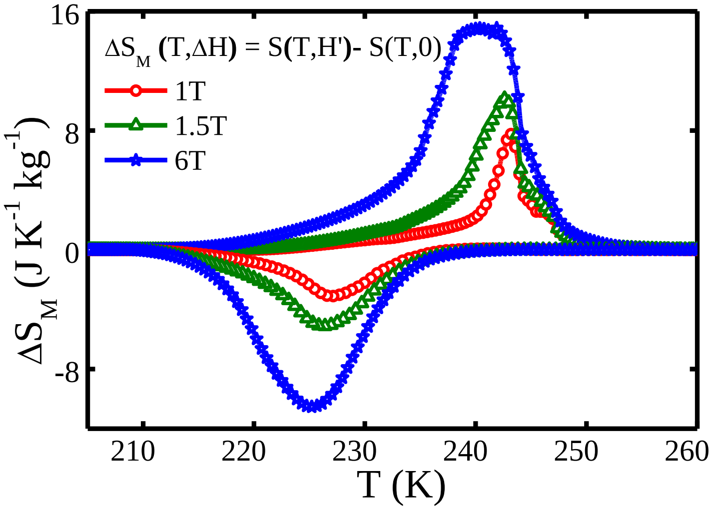

Figure 4.8 Magnetic field induced entropy change (magnetocaloric effect) as a function of temperature for selected values of the magnetic field (1, 1.5 and 6 T) in $Ni_2Mn_{1.36}Sn_{0.32}Al_{0.32}$.

The magnetic field induced entropy change (magnetocaloric effect) was computed as mentioned in details in the beginning of section 4.1. Results obtained from cooling and heating isofield runs are shown in Figure 4.8 for different values of the applied fields. The inverse nature of the MCE is consistent with the magnetic field stabilizing the austenitic phase. We observe that with increase in magnetic field the width of the ΔS_M vs T peak increased in both heating and cooling runs and at higher field the peak developed into a plateau like feature. The increased width shows that the refrigerant capacity of the sample increased as the field increased. The maximum value of entropy change obtained for the field of 1.5 T was found to be 10.1 J $kg^{-1}K^{-1}$ whereas that measured form the isothermal magnetic measurement is 8.2 J $kg^{-1}K^{-1}$. Almost similar values of ΔS_M obtained using direct calorimetric measurements and magnetic measurements rule out the possibility of over estimation of the entropy change. As the system studied are similar and MCE occurs in almost same temperature range, it is expected that the value of ΔS_M evaluated form the isothermal magnetization measurements for other samples also are not at all overestimated.

4.1.2 Ni-Mn-Sb-Al

The Ni-Mn-Sb system also displayed MCE though the value was much smaller in comparison to Ni-Mn-Sn counterpart. The maximum value of 19.1 $JKg^{-1}K^{-1}$ has being observed in $Ni_{50}Mn_{38}Sb_{12}$ system at 5 T field change [25,141]. Recent work on doping showed that it was possible to manipulate this property and enhance the MCE. It was found that MCE in Co doped system can be as high as 34 $JKg^{-1}K^{-1}$ in $Ni_{45}Co_5Mn_{38}Sb_{12}$ in 5 T field [142]. We thus investigate the effect Al replacement has on the MCE in the Ni-Mn-Sb system.

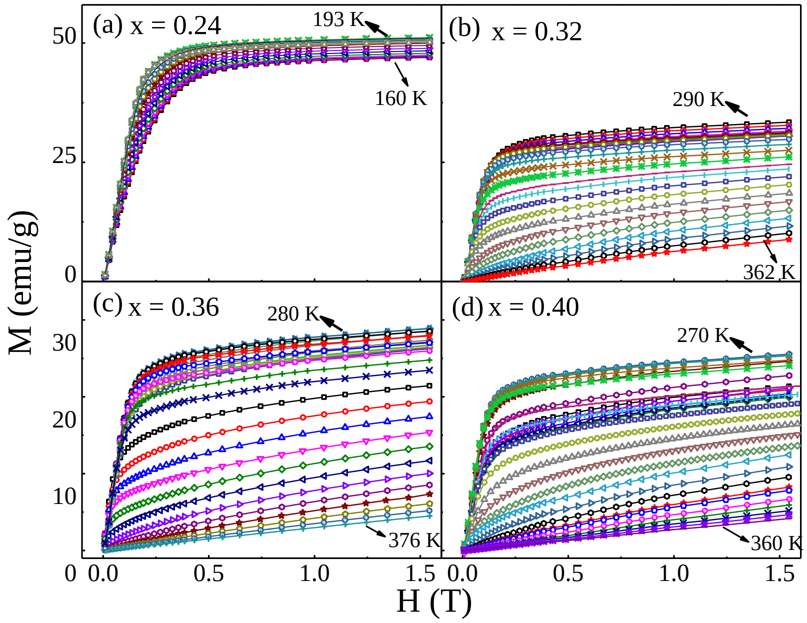

Figure 4.9 a) shows M-H measurement performed at an interval of 3 K in the vicinity of MT. b) to d) show similar curves up to a field of 1.5 T in vicinity of martensitic and FM transitions in Sb system.

The M-H measurements were performed as mentioned in section 4.1.1 for $Ni_2Mn_{1.36}Sb_{0.64-x}Al_x$ system. Figure 4.9 (a) shows M-H measurements performed on x = 0.24 sample in the vicinity of MT. The MT and magnetic transitions for x = 0.32 to 0.40 occurred in close temperature interval as discussed in section 3.2.4.1. Thus it is expected that sample will show both conventional and inverse MCE. While the inverse MCE is associated with MT, the conventional MCE comes to existence because of ferro to para transition at Curie temperature of the system. The M-H loops were measured for x = 0.32 to 0.40 as shown in Figure 4.9 (b-d), starting form temperature below the austenitic start temperature and was continued till the system transformed to the paramagnetic phase. The magnetization for x = 0.32 to 0.40, initially increased owing to MT and then fell due to approaching T_C.

The ΔS_M calculated form the magnetization data is shown in the Figure 4.10. The sample with composition x = 0.24 shows inverse MCE and the maximum ΔS_M was 0.36 $JKg^{-1}K^{-1}$ while the conventional MCE was not evaluated for the present system. Unlike Ni-Mn-Sn-Al system the ΔS_M peak in present samples are much wider, but height is much smaller. The RC for the x = 0.24 sample was found to be 6.8 JKg^{-1}, which is much lower compared to Ni-Mn-Sn based system. The maximum values of inverse and conventional ΔS_M along with their respective RCs were evaluated as mentioned in the above section. The values are given in Table 4-1. The MCE in x = 0.32, 0.36 and 0.34 occur within 280 K to 370 K and the RC values of inverse and conventional MCE showed opposite trends. While the value of RC for inverse MCE increased, the same decreased for conventional MCE with increase in Al content. As x increased the A_F temperature of the sample also fell, thus MT transformation occurred at lower temperature (Table 3-3). Below T_C magnetism of the austenitic phase increased thus lower the transition temperature more was the change across MT leading to larger RC for inverse MCE in the sample. On the other hand the further the MT transition took place from the T_C the slower was the change in magnetization across T_C. Thus the conventional RC for the sample fell with increasing x. The conventional RC of 34.3 JKg^{-1} was obtained for x = 0.32 which was even larger than the highest RC of Ni-Mn-Sn-Al system at same field. Thus we see that even though the inverse magnetocaloric effect in Ni-Mn-Sn-Al was larger than the Ni-Mn-Sb-Al system, the conventional MCE in Ni-Mn-Sb-Al system gave better cooling power. Furthermore since the MCE effect occurred in large temperature interval in Ni-Mn-Sb-Al system and also as the change of magnetization across the MT was much smaller, the possibility of hysteresis loss and errors due to metamagnetic transition were thus reduced.

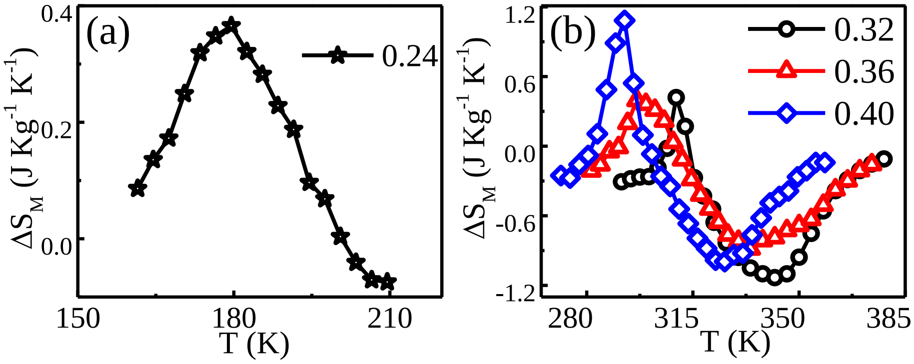

Figure 4.10 Temperature dependence of entropy change in $Ni_2Mn_{1.36}Sb_{0.64-x}$ Al_x is shown in (a), across MT calculated form the isothermal magnetic data for x = 0.24 system, and b) shows entropy changes across MT and Curie temperatures for the rest of the systems.

Table 4-1 Maximum value of entropy change (ΔS_M) and the refrigerant capacity (RC) for inverse and conventional MCE are given here.

	Inverse MCE		Conventional MCE	
x	**ΔS_M (J Kg^{-1} K^{-1})**	**RC (J Kg^{-1})**	**ΔS_M (J Kg^{-1} K^{-1})**	**RC (J Kg^{-1})**
0.24	0.36	6.8	-	-
0.32	0.42	1.3	-1.13	-34.3
0.36	0.39	3.9	-0.88	-29.8
0.40	1.08	7.6	-0.99	-24.6

4.2 Exchange Bias effect

When materials with FM-AFM interfaces are cooled through the Neel temperature, T_N of the AFM (with the T_C of the FM larger than T_N) anisotropy (exchange bias) is induced in the FM. Exchange bias is one of the phenomena associated with the exchange anisotropy created at the interface between an AFM and an FM material. When the sample is exposed to a static magnetic field at a temperature $>T_N$ and cooled through T_N down to a low temperature ($<<T_N$), the FM moments adjacent to AFM moments are coupled to the uncompensated AFM moments. This coupling gives rise to a displacement, H_E, of the magnetic hysteresis loop, which is typical manifestation of exchange bias (EB) effect. The value of H_E depend on the relative orientation of the FM moment and the magnetic

moment of one the magnetic sublattice of the AFM phase [118,143]. The EB effect was first observed in 1956 by Meiklejohn and Bean [144] at low temperature in Co/CoO core–shell nanoparticles.

The possible applications of the EB phenomenon are in spintronic devices such as spin valves, read heads and nonvolatile memory. The EB effect has been observed in magnetic nanoparticles [144], spin glass [145] and polycrystalline materials [146]. The presence of AFM-FM interface in the Ni-Mn based FSMA in the martensite phase would result in EB behavior which has been observed in Ni-Mn-Sb, Ni-Mn-Sn and Ni-Mn-In system [118]. Exchange bias as large as 2520 Oe has been observed in Ni-Mn-Al-Si system [147]. Thus we were also motivated to do similar studies in our system.

We have also performed the EB measurement on selected compositions. The M-H loops were measured using two different protocols. First the sample was cooled to lowest temperature of measurement under zero applied magnetic field and magnetic hysteresis curve was measured, and then the sample was again heated to room temperature and was cooled under applied magnetic field to lowest temperature of measurement (FC) and magnetic hysteresis curve was again measured.

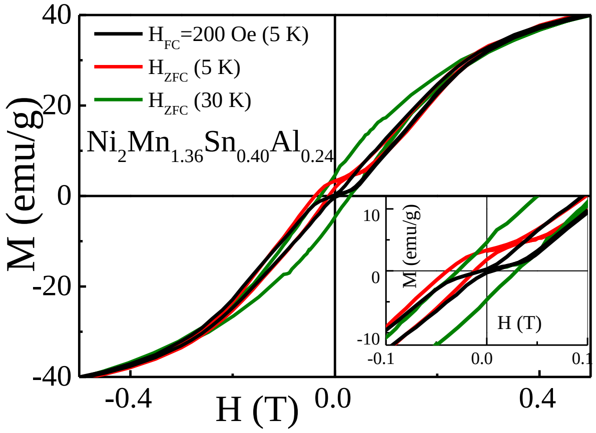

Figure 4.11 The M-H curves measured after FC at 200 Oe and ZFC at different temperatures. Inset shows the expanded region near zero field.

Figure 4.11 shows the isothermal magnetic hysteresis measurements performed at 5 K after ZFC (inset shown only from −0.1 T to 0.1 T for clarity) on $Ni_2Mn_{1.36}Sn_{0.64-x}Al_x$ for x = 0.24. The ZFC M-H curve showed symmetric double shifted loop which was observed before in off-stoichiometric Ni-Mn-Sn samples [148]. The double shifted loop vanished when M-H measurement was performed at 30 K after ZFC. Double shifted loops were observed in a system that had AFM-FM interface. When the sample was zero field cooled, the AFM region got divided into two types of regions which were locally oriented in opposite directions. The AFM regions pinned various FM regions in opposite ways, giving rise to double shifted loops [110,145,148]. This interaction also led to shift in hysteresis loop along the field axis when sample was field cooled giving rise to EB effect. In order to confirm EB-effect M-H was performed at 5 K after field cooling at 200 Oe, in fields ranging from +1 T to -1 T, which were much above the saturation field. The sample showed EB-effect in which M-H curves were asymmetric and loops shifted both horizontally and vertically. The horizontal shift (H_E) which gave EB-field, was found to be about 250 Oe. Here $H_E=-(H_1+H_2)/2$, H_1 and H_2 being the left and right coercive fields respectively. The vertical shift in the M-H curve also implied that double shifted loop and EB arose due to the presence of glassy magnetic phase [36].

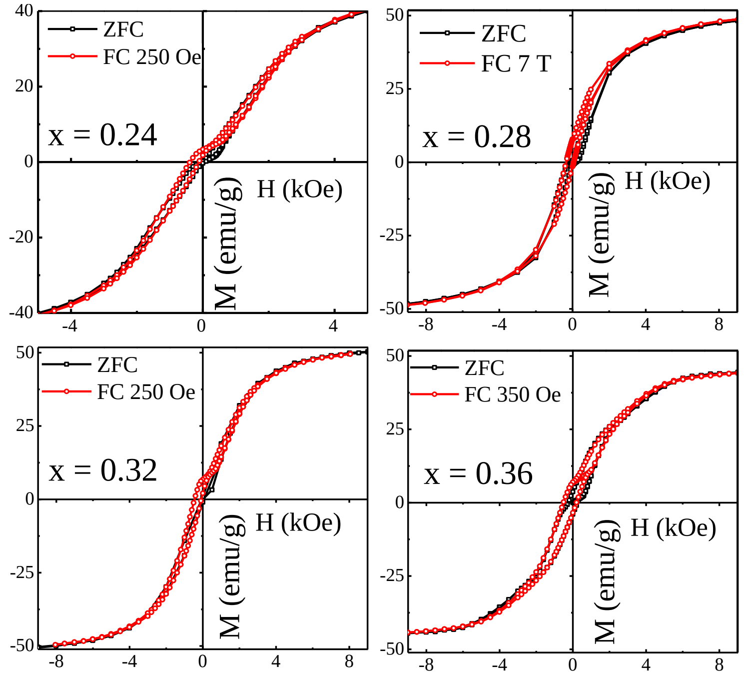

Figure 4.12 Shows the M-H curve measured after FC at different field for different samples ($Ni_2Mn_{1.36}Sn_{0.64-x}Al_x$) and ZFC at temperature of 5 K

Similar measurements were also performed on the $Ni_2Mn_{1.36}Sn_{0.64-x}Al_x$ for x = 0.28, 0.32 and 0.36 and are shown in the Figure 4.12 along with x = 0.24 sample for a comparison.

It was found that all samples displayed the double shifted loops while sample with x = 0.36 showed the smallest such loop. As mentioned in the Section 3.1.4.2, the AFM interaction in the martensitic phase became weaker as the Al content increased thus we observed weak double shifted loop in the x = 0.36 sample. The H_E in the sample was found to be 250 Oe, 140 Oe, 270 Oe and 150 Oe respectively for x = 0.24, 0.28, 0.32 and 0.36 when samples were cooled under different applied field.

4.3 Discussion

In the present chapter we have shown that the substitution of Al in the Ni-Mn-Z system offers us a way to control the functional properties of the system.

We have shown that a large value of ΔS_M can be obtained in a relatively low field (1.5 T) which can be supplied by an Nd–Fe–B permanent magnet. This makes a practical proposition. Furthermore the Ni-Mn-Z based systems reported here are much cheaper than the Ga based systems [149,150], while retaining the tunability of MT of the system through composition change. We also showed that the measurement of ΔS_M using indirect method of magnetization measurement agrees with more direct method of calorimetric measurements in our samples thus showing that there was no over estimation of the ΔS_M.

While the $Ni_2Mn_{1.36}Sn_{0.64}$ sample showed maximum value ΔS_M of 5 J $Kg^{-1}K^{-1}$ in the field of 2 T replacement of Al for the Sn enhanced the maximum value ΔS_M to 10.2 J $Kg^{-1}K^{-1}$ in the composition of $Ni_2Mn_{1.36}Sn_{0.36}Al_{0.28}$ at the field of 1.5 T. Thus substitution provides us with way to enhance the MCE in these samples. The Sb based system with Al replacement did not display the large inverse MCE as observed in Sn based systems but nevertheless the conventional MCE observed in the system was found to have better RC value than the Sn based system. Thus both systems display excellent MCE in them. The system also displayed the EB effect which may find application in the future spintronic devices. Further EB measurement confirms that the AFM interaction was weakest in the martensitic phase of $Ni_2Mn_{1.36}Sn_{0.24}Al_{0.40}$ sample as inferred from the magnetization measurement at 80 K.

Chapter 5

Dynamic magnetization measurements

In this chapter we shall investigate the dynamics of the low temperature martensitic phase where the presence of the competing long range FM-AFM interactions creates a frustration. As the temperature of the system is lowered spins freeze in random directions giving rise to a frozen spin system. We shall study dynamic response of the frozen system with time varying and static magnetic fields. Dynamic response study gives information about the type of freezing process and the interactions taking place among various magnetic spins. These also give idea about the size of locally correlated magnetic spins or clusters. The dynamics of the glassy system can also be analyzed by studying the magnetic field temperature (H, T) phase diagram using static magnetic field. The (H, T) diagram may not give a full picture about the nature of spin glass present in a system, as the usual experiments are hardly performed under thermodynamic equilibrium; nevertheless it reflects what kind of dynamics involved in the freezing or defreezing process.

Magnetic state of the martensitic phase in Ni-Mn-Z type of systems usually consists of competing FM and AFM interactions. Furthermore AFM interaction is promoted in the martensitic phase as temperature is lowered [33]. The competing FM and AFM interactions form a mixture of competitive bonds that may create frustration in system and with lowering of temperature freezing may be promoted, thus these systems shows various type of freezing [35].

The dynamics of the martensitic phase of Ni-Mn based FSMA has been studied here in systems with different compositions. The nature of freezing varies from system to system and composition, and has been interpreted as spin glass freezing [38,151], blocking of magnetic clusters [113] and superspin glass freezing [152,153]. These studies are only a few and any comprehensive study on how the dynamics of the system is influenced by the change in the composition of system is lacking. Such study can help in better understanding of the interaction in these systems. With above goal in mind we have performed detailed ac and dc dynamics studies of the systems we have developed.

5.1 Relaxation study via ac susceptibility

The dynamics of relaxing systems like spin glass and super-paramagnetic system is generally analyzed using linear and nonlinear parts of ac susceptibility and dependence of freezing temperature on time scale of measurement, where time scale is inverse of the frequency of measurement ($t= 1/f$). In general the ac susceptibility of a material with magnetization (m) can be expanded in the power series of oscillating magnetic field (h) as $m = m_o + \chi_1 h + \chi_2 h^2 + \chi_3 h^3 + \chi_4 h^4 \ldots$, where m_o is the spontaneous magnetization, χ_1 the linear susceptibility, χ_2, χ_3, $\chi_4 \ldots$ are the higher order non-linear susceptibilities. The χ_1 term has further been expressed as $\chi_1 = \chi^{/} + i\chi^{//}$ where $\chi^{/}$ and $\chi^{//}$ are real and imaginary parts of susceptibility. In cases where time inversion symmetry breaking field is absent, i.e. $M(H) = - M(-H)$ the terms corresponding to even power of h (χ_2, χ_4) are zero. In the study of nonlinearity only the magnitude of the χ_3 term is presented here and higher harmonics are ignored. It has been shown that the details obtained by the neutron depolarizing experiment about the magnetic nature of cluster can be correlated by studying the higher harmonics ac susceptibility [154].

To evaluate the magnetic state of the relaxing system, linear frequency dependent ac susceptibility is analyzed. The frequency dependent shift of freezing temperature (T_f) provides an important criterion in distinguishing spin glass freezing and superparamagnetic blocking. The value of parameter Φ is defined as,

$$\Phi = \frac{\Delta T_f}{T_f \, \Delta \log f}, \tag{5-1}$$

where f is the frequency at which measurement was performed. Here Φ is the relative shift of the T_f for per decade change in f. It was experimentally found to be a small number, nevertheless some distinct ranges could be found. For magnetically dilute alloys, the range is below 0.01, for alloys of Mn with another transition metal, it comes to higher values like 0.025, and for concentrated alloys and insulating glasses it can range up to 0.08. On the other hand, it can go up to 0.3 for superparamagnets [11,12].

The frequency dependent shift of freezing temperature, especially for system with non-interacting particles, is also analyzed in terms of Arrhenius law for thermal activation involving constant energy barrier given by [157],

$$f = f_0 \, e^{-\frac{E_a}{K_B T_f}}, \tag{5-2}$$

where f_0 is characteristic frequency and E_a is the activation energy. In most spin glass systems, where interaction exists, such an analysis results in unphysical value of both f_0 and E_a. Thus it offers a way to distinguish spin glass from the superparamagnetic system. Usually f_0 has a value in range of 10^8 to 10^{13}, for a system of non-interacting superparamagnetic particles [158].

In case of an interacting system the fitting with equation (5-2) gives unphysical values, which hints at cooperative dynamics due to inter-cluster interaction. The Vogel-Fulcher law, $\tau = \tau_0 \mathrm{Exp}\,[E_a/k_B(T-T_0)]$, where T_0 and τ_0 ($\tau = 1/f$) being characteristics temperature and time respectively, which describes the viscosity of the super cooled liquid is often used in analysis of interacting system [159,160]. It gives better and more physical values of the fitting parameter.

The dynamics of spin glass system shows freezing and it is expected to obey the standard critical slowing down relation given by theory of dynamical scaling near the phase transition [156,157], defined as,

$$\tau = \tau^{*}\left(\frac{T_f}{T_0} - 1\right)^{-z\upsilon}, \tag{5-3}$$

where T_0 is freezing temperature as frequency and field tends to zero, while z is the critical exponent of the correlation length ξ given as (T_f/T_0 -1), υ is dynamical exponent and τ^* is macroscopic relaxation time related to spin glass or cluster glass. The value of $z\upsilon$ lies within 4 - 12 for spin glass system, whereas τ^* is of the order of 10^{-12}-10^{-14} s [161]. For ordinary phase transition τ usually is very small (hardly reaches macroscopic time scale) and $z\upsilon$ is around 2 [157].

In our analysis of the system we have mostly used the relative shift of the T_f for per decade change in *f*, along with Arrhenius law and dynamical scaling law near phase transition. Though other laws described above in brief can give us ideas regarding the nature of spin glass system, it was observed that power law can better account for the experimental observation [162].

5.1.1 Ni-Mn-Sn-Al

Frequency dependent susceptibility measurements were performed in the range from 11 Hz to 1 kHz at low temperature in the martensitic phase within 80 to 200 K for $Ni_2Mn_{1.36}Sn_{0.64-x}Al_x$ systems. The real ($\chi^{/}$) and imaginary ($\chi^{//}$) parts of linear susceptibility are shown in Figure 5.1 for various x as indicated in figure. It can be seen that the $\chi^{/}$ fell as the temperature was lowered, whereas the $\chi^{//}$ showed a broad peak. The frequency dependent susceptibility could not be performed for the x = 0.36 sample as signal was low and noisy, and peak could not be determined in the $\chi^{//}$ curve. In all the samples as the frequency of measurement was increased, the $\chi^{/}$ and $\chi^{//}$ curves and the peaks in the $\chi^{//}$ curves shifted to higher temperatures. The freezing temperature T_f was defined as a temperature at which the $\chi^{//}$ showed a maximum and its dependence on measuring frequency, is an indication of existence of glassy magnetic phase in the system. The T_f*'s* obtained for the different x are collectively shown in the Figure 5.2 (d).

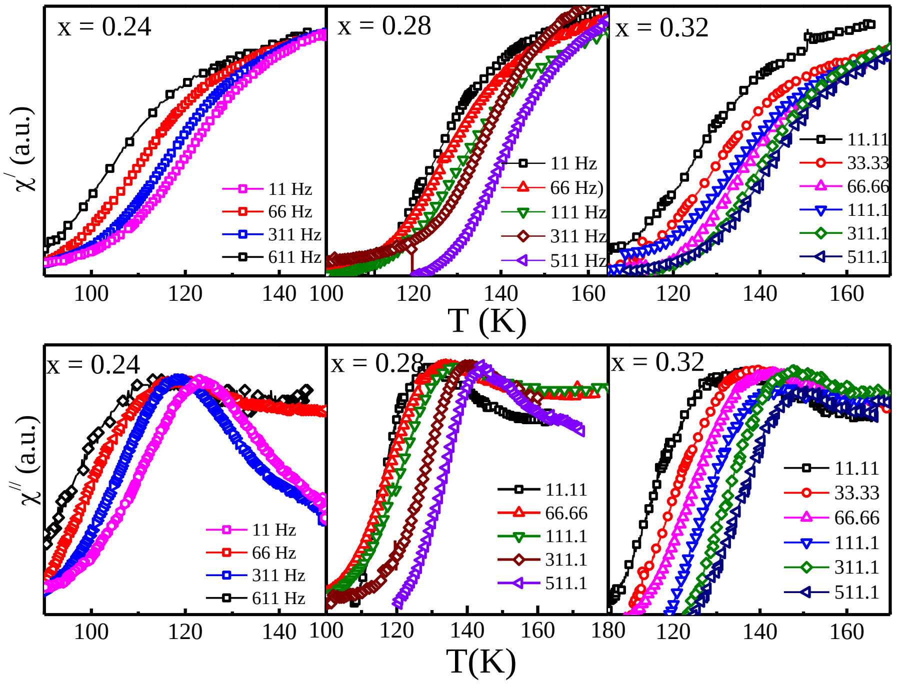

Figure 5.1 The frequency dependent real ($\chi^{/}$) and imaginary ($\chi^{//}$) parts of ac susceptibility for various Ni$_2$Mn$_{1.36}$Sn$_{0.64\text{-}x}$Al$_x$ are shown.

The parameter Φ obtained by fitting T_f to equation (5-1) was found to be 0.094, 0.0794 and 0.0569 for x = 0.24, 0.28 and 0.32 respectively. It can be seen that as the Al content increased the parameter Φ fell. The value of Φ was on the rather higher side for x = 0.24 sample and raised the suspicion on the system being on the borderline of a superparamagnet. This was even more possible, for it was known that the high values could come from ferromagnetic clustering [155]. However, there were other checks for it. We tried to fit the M-H loop at 30K with Langevin function [163], but the fit ended with an unphysical negative value of susceptibility, thus the existence of superparamagnet was unlikely in the x = 0.24 sample. Such a high value of Φ had been observed in the system with similar compositions [38,151]. Next, the data were fitted to the Arrhenius law. The fitted parameters E_a and f_0 are given in Table 5-1. These unphysical values imply that the interaction among the clusters was strong enough to affect the dynamics of the system. It can further be noted that as the x concentration increased in the system the values of the E_a and f_0 also increased.

To obtain characteristic time scale of activation near T_f, we analyzed the result using equation (5-3). The result is shown in Figure 5.2 (a-c). The values obtained for τ^* and $z\nu$ are given in the Table 5-1. As mentioned earlier the value of $z\nu$ was within 4 - 12 for spin glass system, whereas τ^* was of the order of 10^{-12}-10^{-14} s. Such a large value of τ^*, coupled with the largish value of Φ would imply a slow dynamics in the system, due to the presence of a small internal retarding field, similar to reported previously in the context of an assembly of interacting particle system [164]. This in all probability implied that system might be in cluster spin glass state in low temperature region. It can be further be seen that as the x increased the value of τ^* decreased. This implies that with the increased in the Al content the size of the cluster decreased, thus its characteristics relaxation time decreased.

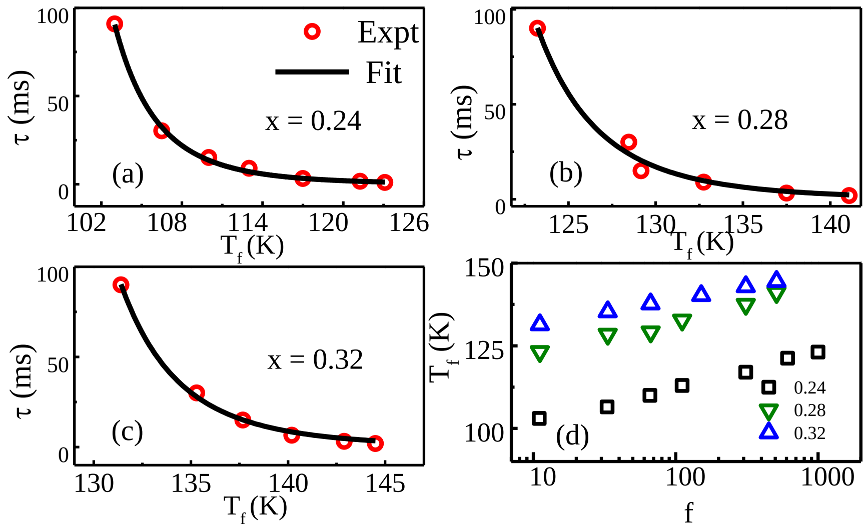

Figure 5.2 Red circles in (a-c) show the peak temperature (T_f) obtained for different frequencies ($\tau = 1/f$) and the black lines are the curves fitted with dynamic scaling law, d) shows the T_f as the function of frequency for different x in $Ni_2Mn_{1.36}Sn_{0.64-x}Al_x$.

The magnetization measurement in the Section 3.1.4, shows that with increase in Al content overall magnetization of martensitic phase fell, showing that the FM interaction weakened. Further the coercive field increased with increasing Al, thus the strength of AFM interaction also decreased. The weaker FM and AFM interaction may thus lead to formation of smaller clusters. The AFM interaction was weakest in case of x = 0.36 samples and it is also evident form the magnetization measurements as discussed in Section 3.1.4. Thus this system did not show spin glass type of freezing.

Table 5-1 The freezing parameters obtained are given. The parameter Φ defined by equation (5-1), f_0 prefactor and E_a activation energy defined by equation (5-2), and τ^* is macroscopic relaxation time and zυ is exponent of equation (5-3).

x	*Φ*	f_0 *(Hz)*	E_a/k_B *(K)*	*τ* (s)*	*zυ*
0.24	.0941	3.0 X 10^{13}	2970	1.2 X 10^{-5}	5.5
0.28	.0794	5.2 X 10^{12}	3250	7.5 X 10^{-6}	5.8
0.32	.0569	6.7 X 10^{19}	5700	1.8 X 10^{-6}	5.7

5.1.2 Ni-Mn-Sb-Al

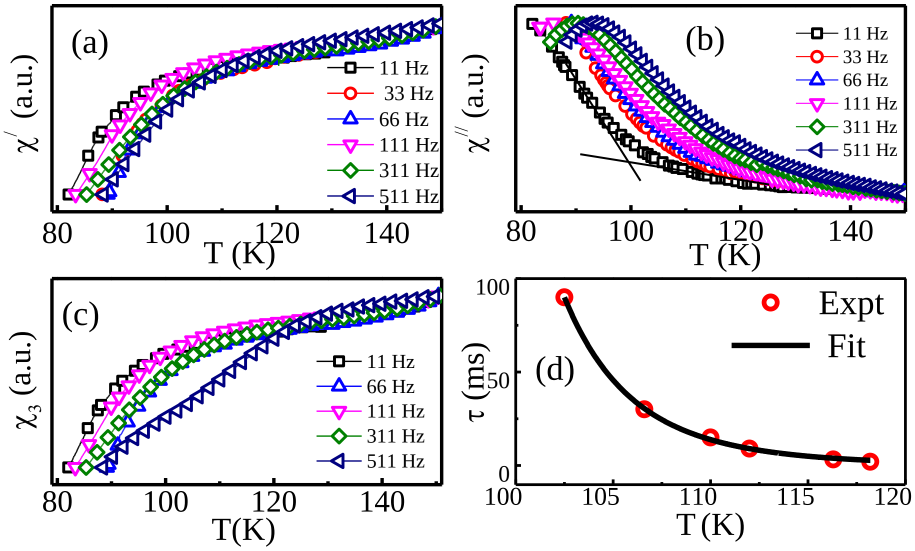

Figure 5.3 a) and b) shows $\chi^{/}$ and $\chi^{//}$ measured for $Ni_2Mn_{1.34}Sb_{0.40}Al_{0.24}$ samples. c) Shows χ_3 of ac susceptibility and d) shows the T_f obtained for different *f* (*τ = 1/f*) and the black line is the curve fitted with equation (5-3).

The real ($\chi^{/}$) and imaginary ($\chi^{//}$) parts of the frequency dependent susceptibility measured for the sample with composition $Ni_2Mn_{1.34}Sb_{0.40}Al_{0.24}$ are shown in Figure 5.3 (a) and (b) respectively. The natures of curves are similar to the $Ni_2Mn_{1.34}Sn_{0.40}Al_{0.24}$, but the system did not freeze completely at 80 K, as the fall in $\chi^{/}$ had not reached the minimum. The $\chi^{//}$ rose for lower frequency till 80 K and peak like feature appeared at higher frequency. Both $\chi^{/}$ and $\chi^{//}$ shifted to higher temperature as the measurement frequency was increased. The shift in temperature with increasing frequency was determined from the intersection of the tangents drawn on low and high temperature side of the $\chi^{//}$ curve as shown in the Figure 5.3 (b). The shift obtained this way agreed with the shift of the peak at the higher frequencies in the $\chi^{//}$curve (as peaks were observed only at higher frequencies). The obtained temperatures are shown in the Figure 5.3 (d). The parameter Φ obtained using equation (5-1) was 0.0378, which was within the range of metallic spin glass. Fitting with equation (5-2) gave the values of f_0 and E_a as 5.7 x 10^{14} and 3300 K respectively. The τ^* and $z\nu$ values obtained from the equation (5-3) of dynamic scaling law are given in the Table 5-2. The frequency dependence of the third harmonic (χ_3) of ac susceptibility is also shown in Figure 5.3 (c). The curves were similar to the $\chi^{/}$ and shifted to higher temperature with increase in frequencies. Also the nature of the curves is different from the lower frequencies, this can happen, as at different frequencies we probe regions of different correlation lengths. This shows that the interaction among clusters of various sizes was different [158,165].

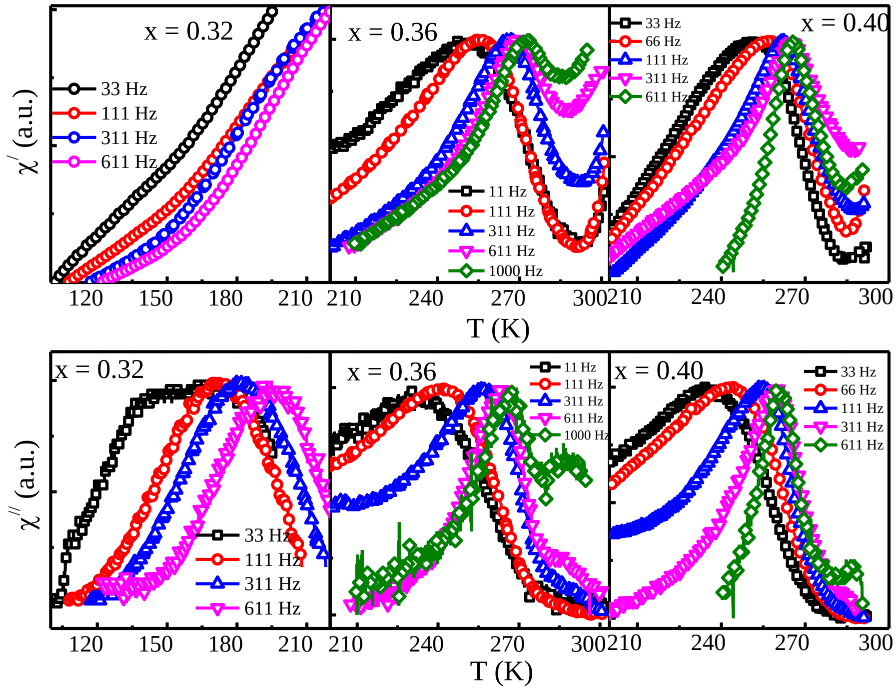

Figure 5.4 The $\chi^{/}$ and $\chi^{//}$ susceptibility measured at different frequencies for $Ni_2Mn_{1.34}Sb_{0.64-x}Al_x$ with x = 0.32, 0.36 and 0.40.

The $\chi^{/}$ and $\chi^{//}$ part of frequency dependent susceptibility for alloy with x = 0.32, 0.36 and 0.40 are shown in the Figure 5.4. In case of Sb alloy with x = 0.32, the $\chi^{/}$ fell as the temperature fell, whereas a broad peak was observed at the lower frequencies in the $\chi^{//}$

part and both curves showed shifts to higher temperature with increasing frequency. As the peak in $\chi^{//}$ was broad at lower frequencies we could not identify the T_f. The frequency dependent shift shows that the sample might be in glassy magnetic phase.

For the samples with x = 0.36 and 0.40 both $\chi^{/}$ and $\chi^{//}$ curves showed peaks and shifted to higher temperature with increasing frequencies. The shifts in T_f (temperature where $\chi^{//}$ showed peak) were obtained and were analyzed as in case of x = 0.24 sample using the equations (5-1), (5-2), and (5-3). The various parameters obtained by fitting are given in Table 5-2. It can be seen that parameters in all systems indicate the presence of spin glass type freezing. The freezing temperature was unusually high. Usually in FSMA spin glass freezing has mostly been reported at temperature below 200 K. Spin glass type freezing near room temperature has been reported in the Pr-based bulk metallic glass [166].

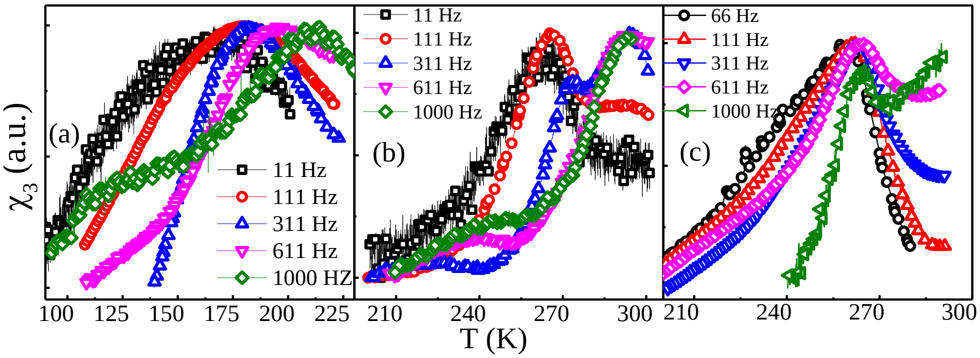

Figure 5.5 The χ_3 measured at different frequencies for alloys $Ni_2Mn_{1.34}Sb_{0.64-x}Al_x$ with x = 0.32, 0.36 and 0.40 shown in (a), (b) and (c) respectively.

In order to confirm if the observed freezing occurred due to spin glass we performed measurements of χ_3 of ac susceptibility and the results are shown in Figure 5.5. χ_3 showed a peak as in the case of $\chi^{//}$ and the peak in χ_3 for the x = 0.32 sample showed large shift with the increasing frequency. The shifts in case of alloy with x = 0.36 and 0.40 were very small. The presence of positive peak indicates that the spin glass was not present in the sample as spin glass shows a negative divergence at T_f [165]. The peak in the χ_3 on the other hand can be due to FM or AFM transition where the χ_3 displayed a positive divergence. Further the shift of the peak temperature with the changing frequency is an indication that the system did not freeze as spin glass.

Table 5-2 The freezing parameters for various systems are given here. The parameter Φ is defined from equation (5-1), f_0 is prefactor and E_a is activation energy as defined from equation (5-2), τ^* is macroscopic relaxation time and zυ is exponent of (5-3).

x	*Φ*	f_0 (s^{-1})	E_a/K_B (K)	τ^*	$z\nu$
0.24	0.0378	5.7 x 10^{14}	3300	3.1 x 10^{-5}	7.4
0.32	-	-	-	-	-
0.36	0.0770	3.4 x 10^{19}	10000	3.7 x 10^{-7}	5.5
0.40	0.0867	4.1 x 10^{15}	7634	1.0 x 10^{-5}	4.0

5.1.3 Ni-Mn-In-Al

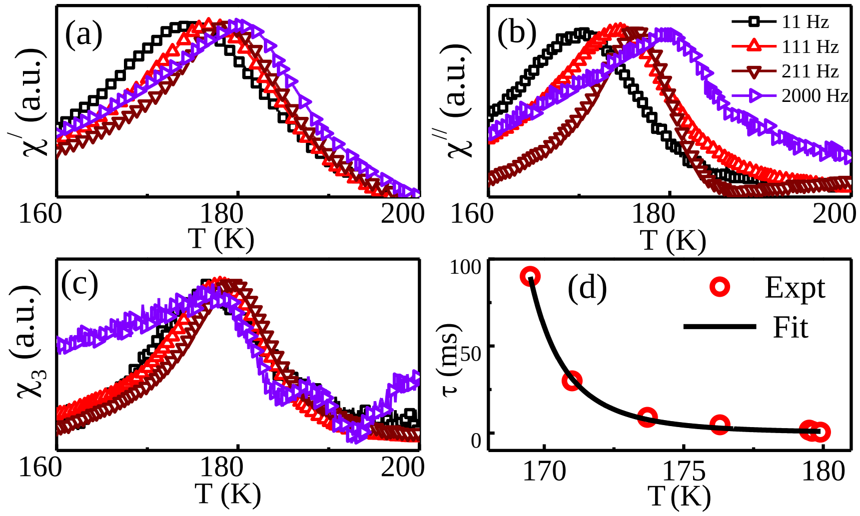

Figure 5.6 a) and b) shows $\chi^{/}$ and $\chi^{//}$ susceptibility measured for the sample with composition $Ni_2Mn_{1.34}In_{0.40}Al_{0.24}$, c) Shows χ_3 and d) shows the peak temperature (T_f) obtained for different f ($\tau = 1/f$) and the black line is the curve fitted with equation (5-3).

We have seen earlier in the Section 3.3 that the system with composition $Ni_2Mn_{1.34}In_{0.40}Al_{0.24}$ transformed to paramagnetic martensitic phase around 250 K and as the temperature was lowered magnetization rose at T_C of the martensitic phase. In the ac susceptibility curve, we saw that peak appeared blow T_C of the martensitic phase. Such peak has been observed before in the Ni-Mn-In system and there are contradictory reports on the nature of peak [112,113]. We shall in this section look into the nature of the peak in details using linear and nonlinear ac susceptibility measurement technique.

To check for the presence of spin glass phase we measured frequency dependent ac susceptibility. The frequency dependent $\chi^{/}$ and $\chi^{//}$ (Figure 5.6 (a) and (b)) showed shifts of peaks with increasing frequency. The T_f was defined as the peak temperature observed in the $\chi^{//}$. Analysis of the shift in T_f was performed using the equation (5-1) and (5-3) as done in the earlier cases. The fitting gave a value of Φ as 0.0299 which lies in the range of simple spin glass. The analysis of peak temperature with scaling law was performed as shown in the Figure 5.6 (d) and it gave values of $z\nu$ as 4.01 and τ^* as 7.2 X 10^{-8} showing that system most probably underwent spin glass transition and the contribution of frequency dependence was coming from the cluster rather than individual spins [164].

Frequency dependence of χ_3 was performed and is shown in Figure 5.6 (c). The shift of χ_3 with frequency was very small as compared to Sb based system. The absence of negative divergence in the χ_3 shows that the system did not freeze in spin glass. The appearance of the peak could be probably due to AFM transition below T_C of martensitic phase. The frequency dependence could possibly come due to progressive blocking of the magnetic clusters.

5.2 Relaxation study via dc magnetization

The influence of a magnetic field on the "spin glass transition" has received considerable attention but similar study of spin glass transition in Ni-Mn based Heusler alloys received little attention. The magnetic field temperature phase diagram (H, T) of the spin glass in the presence of an applied magnetic field (H) and temperature (T) was studied for the selected composition. The (H, T) diagram helped us to determine the effect various Z elements have on the magnetic field temperature phase diagram of $Ni_2Mn_{1.36}Z_{0.64-x}Al_x$ (x = 0.24 and Z = Sn, Sn, In) and the evolution of the dynamics in the system.

The (H, T) phase diagram was derived by de Almeida and Thouless (AT) [167]. They discovered a field-dependent instability line corresponding to the irreversibility in the mean-field model of an Ising spin-glass which occurs with infinite-range random interaction and behaves near the freezing temperature as

$$H(T) \propto \left(1 - \frac{T^*(H)}{T\,(0)}\right)^{\gamma}, \tag{5-4}$$

where H was the measurement field, T* was defined as temperature where irreversibility occurs and T(0) was limiting temperature at zero field. This lines occur for exponent γ =

3/2, and was interpreted as phase transition line by Thulouse [168]. Gabay and Toulouse extended the calculation to include isotropic spin glass (Heisenberg spins) and derived another line which marks the freezing of transverse degrees along the so called Gabay and Toulouse (GT) line which was given by same expression in equation (5-4) but for the exponent $\gamma = 1/2$ [169].

The above lines were based on the hypothesis of thermodynamic equilibrium which is far from reachable in usual experiments but nevertheless such lines give important ideas about different dynamics of the spin glass freezing process [35,161,170]. Moreover it has been shown that such lines also exist for the other similar relaxing systems like superparamagnet and can be derived from a purely dynamical treatment too [171–173].

5.2.1 Ni-Mn-Sn-Al

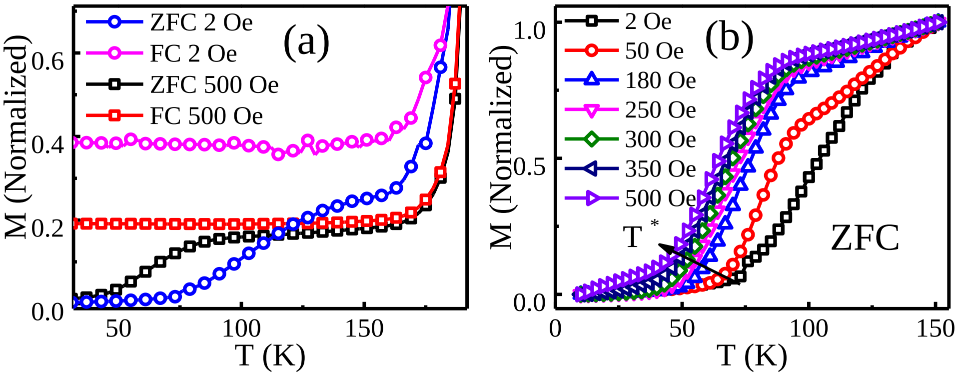

Figure 5.7 a) Normalized zero field cooled (ZFC) and field cooled (FC) magnetization measurements shown only for fields of 2 and 500 Oe. b) Normalized ZFC measurements shown for selected fields up to 500 Oe on $Ni_2Mn_{1.36}Sn_{0.40}Al_{0.24}$ sample.

To investigate the (H, T) phase diagram, ZFC measurements were performed under fields varying from 2 Oe to 2 kOe in the sample of composition $Ni_2Mn_{1.36}Sn_{0.40}Al_{0.24}$. The ZFC curves obtained for two selected fields are shown in Figure 5.7 (a) (for the sake of clarity). In usual practice T^* is defined as the temperature at which the ZFC and FC curves bifurcate. In the present sample we observed that before the point of bifurcation was reached the samples underwent structural transformations in both low and high fields as shown in the Figure 5.7 (a). Thus the value of T^* was taken as the temperature at which magnetization started to rise in ZFC curve as temperature was increased, as shown in Figure 5.7 (b). The exchange bias study in the sample with similar composition had shown that T^* was the temperature above which exchange bias was not observed [38]. Thus T^* marked a transition temperature below which antiferromagnetic interaction became strong enough to pin the spins and caused exchange bias effect and spin freezing. We see that as the measurement field was increased the ZFC curves shifted to lower temperatures, as shown in Figure 5.7 (b). The value of T^* was obtained for the fields of 2 to 2000 Oe as shown in the resultant (H, T) phase diagram in Figure 5.8 (b). As the field was increased T^* fell rapidly until 300 Oe, above which change in T^* was very small. It can be seen that the initial fast variation of T* at low field was stuck above 300 Oe. We fitted data till 300 Oe with the equation (5-4) as shown in Figure 5.8 (b), the fit was excellent with γ =1/2. The variation of $\gamma = 3/2$ and $\gamma = 1/2$ reflects different dynamics occurring in the spin glass system during freezing process. The transverse components of the spin froze along the $\gamma = 1/2$ and the longitudinal spin component froze along the $\gamma = 3/2$ line. This implies that in our system as the temperature increased the transverse component of the spin glass relaxed first. Thus we see that as the temperature was increased in the low field region the weakening of AFM interaction led to relaxation of spins along the transverse direction. In addition, the sharp knee was an indication that above the 300 Oe field, the barrier of the bias field was overcome and it was no longer under thermal control. This also seems to imply that the applied field matched the internal field in the ferromagnetic region, and above that, the unlocked domains could move in response to the applied field.

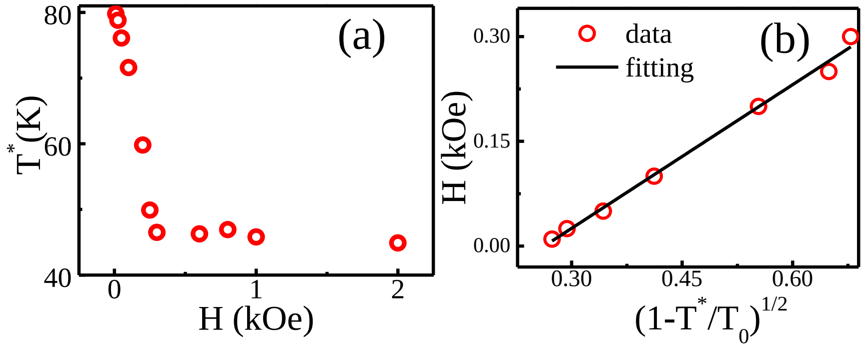

Figure 5.8 a) (H, T) phase diagram, T^* is the freezing temperature at a given field, b) fitting to Heisenberg model, up to 300 Oe as a function of reduced temperature for Sn system.

The internal field occurring due to pinning of FM regions by AFM regions can be estimated form the exchange bias measurement as mentioned in the Section 4.2. The exchange bias field for the present sample was found to be 250 Oe at 5 K, which almost matched with the breakdown field of 300 Oe. These further strengthen the assumption that the breakdown of GT line was caused due to external field domination over the internal field that caused the pinning effect. As the internal field was overcome the spins no longer relaxed alone the transverse line thus giving rise to breakdown.

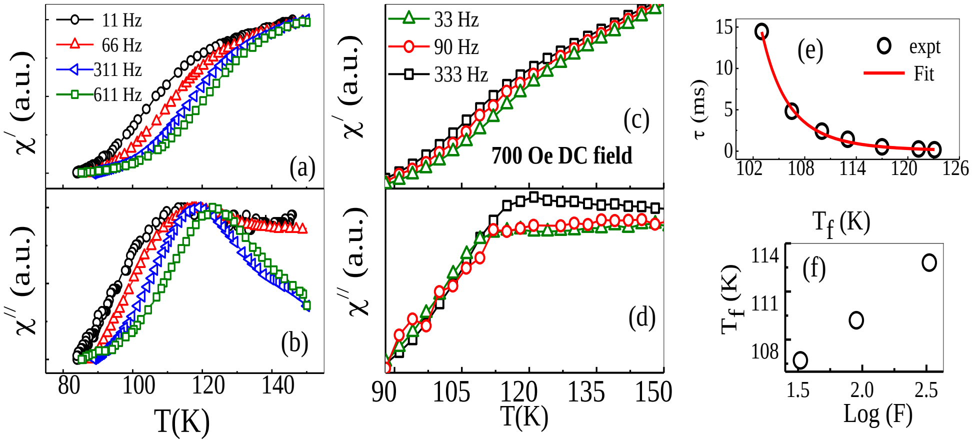

Figure 5.9 Frequency dependent (a) $\chi^{/}$ and (b) $\chi^{//}$ as a function of temperature in zero dc field; (c) and (d) $\chi^{/}$ and $\chi^{//}$ at 700 Oe dc field; (e) experimental date fitted with dynamical scaling law and (f) shift of T_f with frequency at dc field of 700 Oe.

The relaxations of the sample in zero applied dc field was studied in the section 5.1.1. The real ($\chi^{/}$) and imaginary ($\chi^{//}$) parts of susceptibility are shown in Figure 5.9 (a) and (b) respectively. As mentioned earlier the data were fitted to the Arrhenius law given by (5-2). The fitted parameters E_a and f_0 were found to be 2970 K and 3 X $10^{13}s^{-1}$ respectively. These unphysical values imply that system may be in the spin glass type of state. The data were also fitted with dynamical scaling using equation (5-3), near the phase transition as shown in the Figure 5.9 (e). The values obtained for τ^{*} and $z\nu$ were 2×10^{-6} s and 5.5 respectively which showed that system was most probably in cluster spin glass state in zero field.

To further study the nature of irreversibility and the cause of the breakdown (at field > 300 Oe) in the (H, T) phase diagram, we performed ac susceptibility measurements with a dc bias field of 700 Oe (FC) in the SQUID magnetometer and the results are shown in Figure 5.9 (c) and (d). In this case, the extent of responses of both $\chi^{/}$ and $\chi^{//}$ becomes less spread out than before. Additionally we note a striking feature that the peaks of $\chi^{//}$ were now lost in the higher temperature side. It is no more possible to find T_f from the peak, so we need to find it from the first fall of $\chi^{//}$. A plot of this temperature as a function of log(*f*), shown in Figure 5.9 (f), finds a linear dependence and fit to the Arrhenius law gives E_a and ω_0 as 4430 K and 2.37×10^{20} s^{-1} respectively, again unphysical values. The simple spin glass models therefore no longer described the system above the region of breakdown region. We conjecture that under external field, the system turned over from one kind of irreversibility to another [146].

5.2.2 Ni-Mn-Sb-Al

We performed similar measurements on a Sb based system with composition of $Ni_2Mn_{1.36}Sb_{0.40}Al_{0.24}$. The ZFC curves were measured as earlier mentioned, in the fields of 50, 100, 500, 1000 and 2000 Oe as shown in the Figure 5.10 (a). The behaviors of ZFC curves were similar to Sn based system. The curves moved to lower temperature as the measurement field was increased. The T^* was obtained from the ZFC curve as mentioned earlier. The (H, T) phase diagram of the sample is shown in the Figure 5.10 (b). As in the earlier case we observe that the system displayed breakdown at 500 Oe. We expect the breakdown might have occurred at lower field, as the measurements were not performed at the field intermediate of 100 Oe and 500 Oe. It is expected that the at lower field the system would behave in a manner similar to Sn based system, but since only two data points were available at low field we were not able to determine the dynamics of the system.

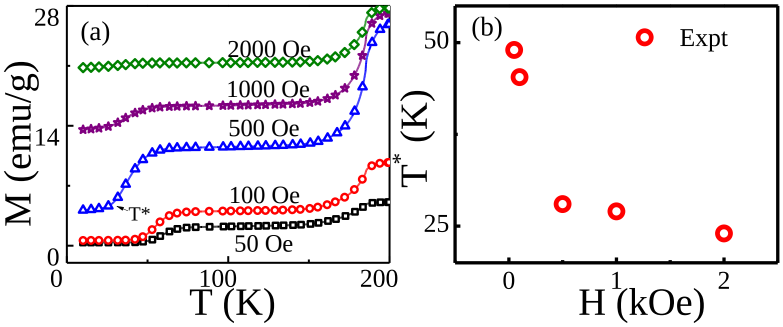

Figure 5.10 ZFC) and FC measurements for $Ni_2Mn_{1.36}Sb_{0.40}Al_{0.24}$,$T^*$ is marked in the curve. b) (H, T) phase diagram as derived from the points in figure (a)

The (H, T) phase diagram of $Ni_2Mn_{1.36}Sb_{0.40}Al_{0.24}$ system and the similarity with the $Ni_2Mn_{1.36}Sn_{0.40}Al_{0.24}$ system show that the breakdown observed in this system at the T^* is not unique to a single system. Moreover T* marks the temperature above which exchange bias was not observed and it was also found that the breakdown occurred at a field slightly greater than the internal exchange bias field of $Ni_2Mn_{1.36}Sn_{0.40}Al_{0.24}$ at 5K, thus showing that internal field played a pivotal role in the breakdown.

5.2.3 Ni-Mn-In-Al

The Sn and Sb systems show reentrant type spin glass behavior as discussed previously. The $Ni_2Mn_{1.36}In_{0.40}Al_{0.24}$ system on the other hand showed freezing behavior where system froze form the paramagnetic system to spin glass. Also the ac susceptibility and dc magnetization measurements in the Section 3.3 showed that the structural transformation occurred at room temperature far above the freezing temperature. Thus unlike the Sn and Sb systems, we were able to determine the temperature at which bifurcation in ZFC-FC curves occurred.

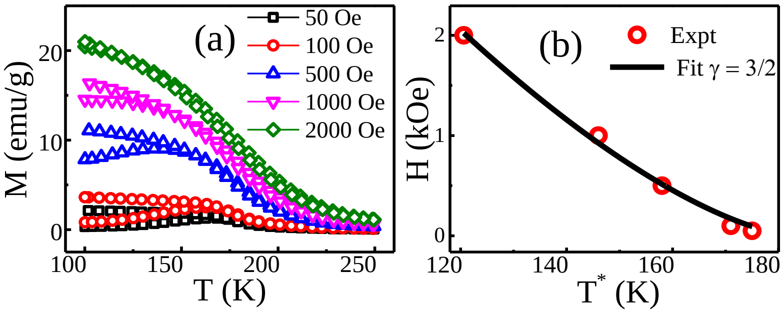

Figure 5.11 a) ZFC and FC measurements on $Ni_2Mn_{1.36}In_{0.40}Al_{0.24}$ sample, T* is temperature where ZFC-FC curve bifurcated. b) (H, T) phase diagram, the line is fitting with equation (5-4) giving $\gamma = 3/2$.

Figure 5.11 (a) shows the ZFC-FC curves measured in the presence of fields of 50, 100, 500, 1000 and 2000 Oe for $Ni_2Mn_{1.36}In_{0.40}Al_{0.24}$ sample. It can be seen that as the measurement field increased the curves shifted to lower temperatures and so did the point at which the ZFC-FC curve bifurcated. We had defined T* in this case as the temperature at which the ZFC-FC curve bifurcated. The (H, T) phase diagram for the system obtained is shown in Figure 5.11 (b). The experimental points were fitted with the equation (5-4) and the value of γ was found to be 3/2, indicating that bifurcation in the system occurred along the AT- line. This shows that at the bifurcation temperature only the component of spin parallel to direction of field relaxed. Recent study on the Ni-Mn-Co-In system also showed similar freezing along the $\gamma = 3/2$ line [174].

5.3 Discussion

The dynamics of the systems was studied below M_F temperature, where the system showed freezing. Analysis of linear ac susceptibility data gave the parameters showing that systems most probably froze in the spin glass state. Further measurements showed that the contribution to the freezing phenomenon was coming from the clusters rather than individual spins. It was also observed that the cluster size showed dependence on the concentration of Al for Sn based system and cluster size decreased with increase in Al content. The systematic dependence on Al concentration was not present in Sb based system.

The freezing in the Sn based system mostly occurred at temperatures below 150 K. Upon replacement of Sn with Sb the freezing temperature shifted almost close to room temperature for higher Al content.

The nonlinear third harmonic measurements in the Sb and In based system did not show the typical signature of the spin glass. Thus the drop in the ac susceptibility in the Sn and Sb based systems and the peaks in the Sb and In based systems most probably came from progressive blocking of the magnetic clusters rather than due to spin glass.

The dynamical study with dc magnetization measurement was carried on the samples with composition of $Ni_2Mn_{1.36}Z_{0.40}Al_{0.24}$, for Z as Sn, Sb and In. The Sn and Sb based system showed similar behavior where the (H, T) phase diagram of the system broke down above the certain field (most probably internal exchange bias field).

The Sn based system was found to defreeze along the transverse line in the low field below the breakdown point. The ac susceptibility measurement showed that above and below the breakdown the system had different dynamics. The (H, T) phase diagram of In based system did not display any breakdown even at higher field. It was found that unlike the Sn based system the moments in these cases relaxed alone the longitudinal line.

Chapter 6

Effect of heat treatments

We performed heat treatments at both low and high temperature on some selected alloy systems and studied how magnetism and magnetocaloric effect evolves in them. Such heat treatments offer us a way to enhance the magnetocaloric effect in the system and tune them to give maximum output. Heat treatment changed the magnetism of both austenitic and martensitic phases, which was outcome of change in ordering. We also studied the effect of low temperature heat treatment on spin glass effect. Analysis of spin glass freezing with linear and non-linear ac susceptibilities helped us to determine how the magnetic cluster and the regions that contribute to freezing in these systems evolve with annealing.

The structural transformation and the magnetism of Ni-Mn based ferromagnetic shape memory alloys are usually controlled by changing composition, employing different heat treatment procedures and using different preparation techniques [15,44,45,175–177]. Recently studies of effect of post quenching heat treatment on the functional properties like magnetocaloric effect, exchange bias effect and magnetoresistance had been performed [87,175–181]. The changes brought about by the post quenching heat treatment in bulk were thought to occur becaus**e** of the change in ordering in the system. As the system orders differently, FM and AFM interactions are modified leading to the above changes [44,45,87,175–178,182]. The secondary heat treatment thus offers a way to control the transformation temperatures and also enhance properties like MCE in the sample. The MT being diffusionless transformation the relative atomic order in austenitic phase is also present in martensitic phase. Thus probing the magnetic character of the martensitic phase will help us to better understand the austenite phase.

The problem with Ni_2Mn-Al system is that upon direct quenching from high temperatures the austenitic phase becomes a mixture of B2 and $L2_1$ phases [61]. The disadvantage of the presence of B2 phase is that it is antiferromagnetic, reducing the overall ferromagnetism in the austenite phase. This reduces change in magnetization during the MT, crucially affecting the effective magnetocaloric property of the system. Careful and long heat treatments are required at lower (than quench) temperature to stabilize larger fraction of $L2_1$ phase as kinetic of system is very low at lower temperatures [61]. Study of magnetocaloric property in $Ni_2Mn_{1.36}Sn_{0.64-x}Al_x$ system in section 4.1.1 showed gradual replacement of Al led to increase in magnetization and magnetocaloric property initially, but then it decreased at higher Al content. The decrease in MCE was attributed to the fact that the increased amount of antiferromagnetic B2 in the system was at the expense of ferromagnetic $L2_1$ as the Al content was increased.

To see the actual improvement in our systems, post annealing heat treatment was performed to increase $L2_1$ fraction, as was performed in case of Ni_2Mn-Al sample [64]. Study of the magnetism of austenitic phase was performed to find the change bought about in the ordering of the system. Study of the spin glass transition with ac frequency dependent susceptibility showed how the various spin glass parameters varied due to post quenching heat treatment and how relaxation phenomena evolved as the ordering in system change. The nonlinear ac susceptibility further helped in determining the origin of frequency dependence at low temperature. Unlike scanning electron microscope which gives us an idea about the grain size, ac susceptibility measurement gives an indication about the size of magnetic clusters and interaction taking place among them. Previous studies of similar systems with dc magnetization predicted growth of ferromagnetic structure with increasing in annealing temperature but these were not conclusive [178]. In the present study we attempt to investigate the evolution of magnetic clusters with a more direct measurement technique.

We studied heat treatment effect in samples of compositions $Ni_2Mn_{1.36}Sn_{0.28}Al_{0.36}$ and $Ni_2Mn_{1.36}Sn_{0.32}Al_{0.32}$. These alloys were selected because both the systems have higher content of disordered B2 phase as shown in the section 3.1, thus making them suitable for the present study. Systematic low temperature post quenching heat treatment was performed on the $Ni_2Mn_{1.36}Sn_{0.32}Al_{0.32}$ sample and effect on properties like magnetism, MCE and freezing at low temperature was studied. In another case, secondary heat treatment at higher temperature was performed on $Ni_2Mn_{1.36}Sn_{0.28}Al_{0.36}$ sample and effects on the magnetism and MCE were studied. The present study helps us in understanding how the ordering in Ni-Mn-Z system influences various properties in the system and ways to tune them to obtain maximum possible output.

6.1 Effect of low temperature heat treatment

Low temperature heat treatment was performed on a $Ni_2Mn_{1.36}Sn_{0.32}Al_{0.32}$ sample. The post quenching heat treatment was performed by sealing the quenched sample in quartz tube and annealing them at the temperature of 450 K, 550 K and 650 K followed by slow cooling in furnace at the rate of 20 K/hr. We shall refer to these post quenched annealed (PQA) samples as A-450, A-550 and A-650 respectively. The results of X-ray diffraction and DSC measurements performed on quenched sample were given in section 3.1, which confirm that sample was mostly in $L2_1$ phase at room temperature and underwent first order reversible structural transformations as a function of temperature.

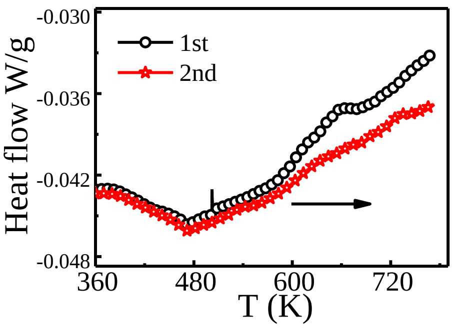

Figure 6.1 DSC thermograph measured during first and second heatings in quenched $Ni_2Mn_{1.36}Sn_{0.32}Al_{0.32}$.

The Ni–Mn–Z alloys upon quenching from high temperature did not directly solidify to the $L2_1$ phase on cooling through equilibrium phase diagram as discussed previously in section 1.3.4. The $L2_1$ structure was reached through a second-order B2–$L2_1$ transition taking place at different temperatures depending on composition. The disorder-order transition temperature, from the B2 to the $L2_1$ phase, was determined using DSC and was defined as temperature at which an exothermic peak was observed in the quenched sample, on the first heating curve [44,182]. The quenching of the samples from high temperature resulted in stabilization of the disordered B2 phase. At first heating the Mn and Z atoms which occupied Mn and Z site randomly, now order and occupy their respective sites in the $L2_1$ structure, this process is a first order (irreversible) transformation thus it is accompanied by an additional heat release which is observed as exothermic peak. When the measurement was repeated the peak corresponding to disorder-order transition disappeared as the Mn and Z now occupied their sites, thus no further transformation occurred. The B2 to $L2_1$ transition temperature was found to be 650 K from DSC thermograph as shown in the Figure 6.1. The disappearance of peak in second run confirms that peak observed was due to B2 to $L2_1$ transition.

The magnetization measurements were performed till fields of 1.5 T on the PQA samples at 300 K as shown in Figure 6.2 (a). The magnetization fell slightly for the sample annealed at 450 K and then increased as the annealing temperature was increased. The drop in magnetization for A-450 sample may be attributed to increase in disorder in the $L2_1$ phase. Recent work by V. Sanchez-Alarcos et al. and Chen et al. has shown that low temperature annealing increased disorder in the system even though the annealing was performed below the order-disorder transition temperature [44,87]. With the increase in disorder larger number of Mn atoms occupied X site, with which the weak AFM interaction increased at the expense of stronger FM interaction in the austenitic phase resulting in drop in the magnetization of austenitic phase of A-450 sample.

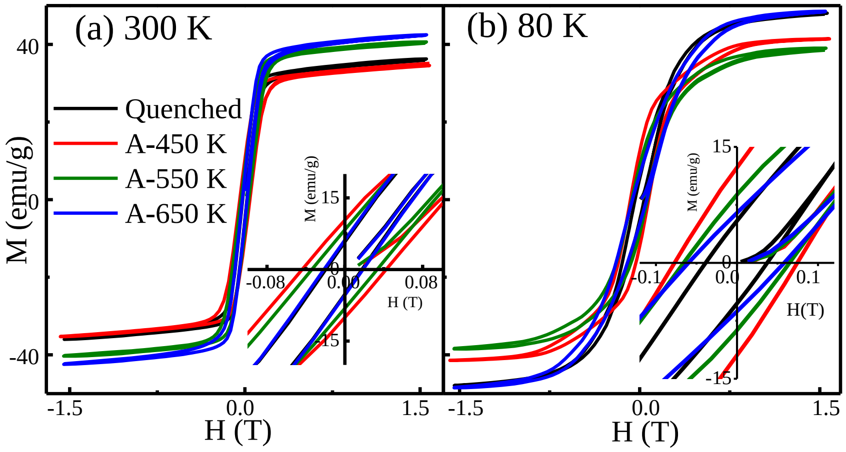

Figure 6.2 MH curves measured for the samples at a) 300 K and at b) 80 K. The insets show the expanded regions near zero field.

The inset in Figure 6.2 (a) shows the magnified view of magnetization, it can be seen that the coercivity increased for sample annealed at 450 K and then decreased towards the coercive value of quenched sample as annealing temperature was increased. The increase in the coercive field of A-450 in austenitic phase can be due to increasing AFM which is still weaker compared to FM thus the anisotropy of AFM interaction cannot pin the FM regions, but nevertheless the presence of AFM hinders of FM regions. As the field was increased the FM rotation irreversibly dragged along more and more of AFM regions, which increased coercivity. As annealing temperature was increased the ordering in sample increased leading to increase in FM at expense of AFM which resulted in increase in the magnetism of the samples and decrease of coercivity as FM had a small amount of AFM hindering its growth. The magnetization measurements were also performed at 80 K in the martensitic phase and are shown in the Figure 6.2 (b). We find that the coercivity had almost similar trend as austenitic phase. The magnetization of the martensitic phase initially decreased for A-450 sample and then increased for A-550 and A-650 sample.

Figure 6.3 shows $\chi^{/}$ measurements performed on all samples in heating and cooling runs at a frequency of 111 Hz. The nature of curves are similar in all cases, they underwent FM and structural transformations as in case of quenched sample. The $\chi^{/}$ fell slightly for A-450 sample for $M_S < T < T_C$ but did not change much for quenched, A-550 and A-650 samples. The fall in A-450 sample because of increase in the AFM interaction as a result of increase in disorder due to low temperature annealing as discussed above. As the temperature is lowered strength of AFM most probably increases more compared to FM interaction leading to above fall in A-450 sample in given temperature range.

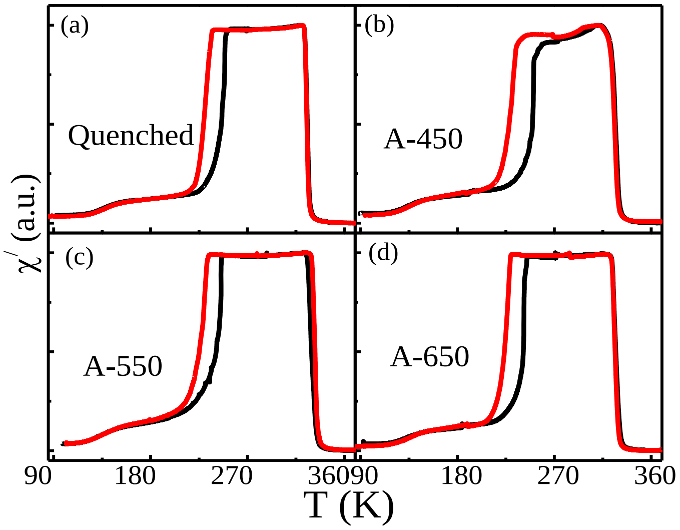

Figure 6.3 Shows ($\chi^{/}$) real part of ac susceptibility measurement performed at 111 Hz for $Ni_2Mn_{1.36}Sn_{0.32}Al_{0.32}$ sample annealed at different temperatures.

Figure 6.4 (a-d) shows the thermo-magnetization curves for quenched, A-450, A-550 and A-650 samples respectively in the field of 100 Oe till 80 K in ZFC, FC and FH sequence. Around 330 K the austenitic phase in systems underwent ferromagnetic transitions, at the Curie temperatures. At lower temperatures (around 250 K) the systems underwent structural transformations resulting in a drop in magnetization**.** The presence of competing AFM/FM interactions in the martensitic phases resulted in splitting of ZFC and FH below martensitic finish temperatures. It can be further seen from the thermomagnetic curves that the drop in magnetization across the MT initially fell for the A-450 sample and gradually increased for the A-550 and A-650 samples. These results agree with the M-H measurements and $\chi^{/}$ measurements.

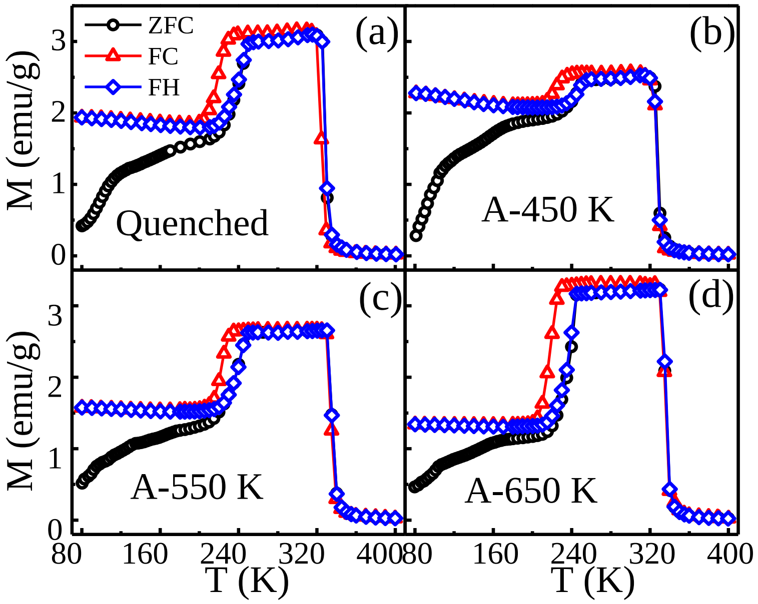

Figure 6.4 ZFC, FC, and FH at the field of 100 Oe as the function of temperature till 80 K for quenched sample and annealed samples.

The M_S (martensitic start temperature) of the samples were obtained from Figure 6.3 and are shown in Figure 6.5. It fell as the annealing temperature increased. A major factor that affects the M_S is the change in e/a ratio. However as we annealed the same sample at different temperatures the e/a ratio remained unaltered here. Thus change in M_S came from other factors such as change in stress distribution at phase boundary, change in atomic ordering, grain size, etc. [182]. The stress relief at grain boundary led to fall in the transition temperature. On the other hand change in ordering caused change in the magnetization of the austenitic phase, an increase in magnetization causes austenitic phase with higher magnetism to stabilize. Thus austenitic phase with higher magnetism was more stable at lower temperature leading to fall in M_S [44,45,87,175–178,182]. The scanning electron microscope results showed that average grain size remains unaltered upon annealing (not shown here). The slight fall in M_S, despite fall in magnetism for A-450 sample may be because of dominating effect of stress relief, the subsequent falls in A- 550 and A-650 are outcome of combined effect of increase in magnetism of austenitic phase and stress relief in the system.

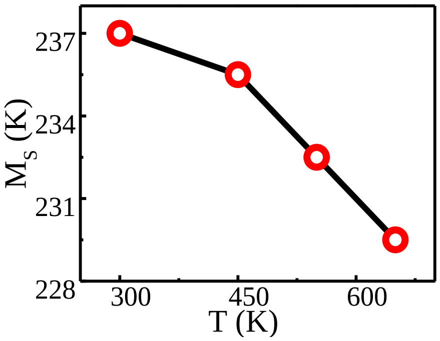

Figure 6.5 M_S as a function of annealing temperature. Line is guide to eye.

The value of ΔS_M was calculated from the isothermal magnetization curve using a modified Maxwell relation, as mentioned in section 4.1. As before the M-H measurements were performed in heating sequence, starting from a temperature that was below M_F, till the temperature at which transformation was completed. These measurements were performed up to a field of 1.5 T at a temperature interval of 3 K. The M-H curve is shown in Figure 6.6 (a) for A-650 sample, similar curves were obtained for other samples. The values obtained for ΔS_M are plotted in Figure 6.6 (b). The maximum of ΔS_M obtained for the quenched, A-450 K, A-550 K and A-650 K samples are 8.2, 3.5, 6.1 and 6.8 $Jkg^{-1}K^{-1}$ respectively. The RCs of the samples were also calculated and gave values of 20.4, 16.0, 15.9 and 24.5 Jkg^{-1} in the same sequence as before. The maximum of ΔS_M fell initially with annealing temperature but then rose with increase in annealing temperature. Though ΔS_M was lower than quenched samples, the RC increased slightly for sample annealed at higher temperatures.

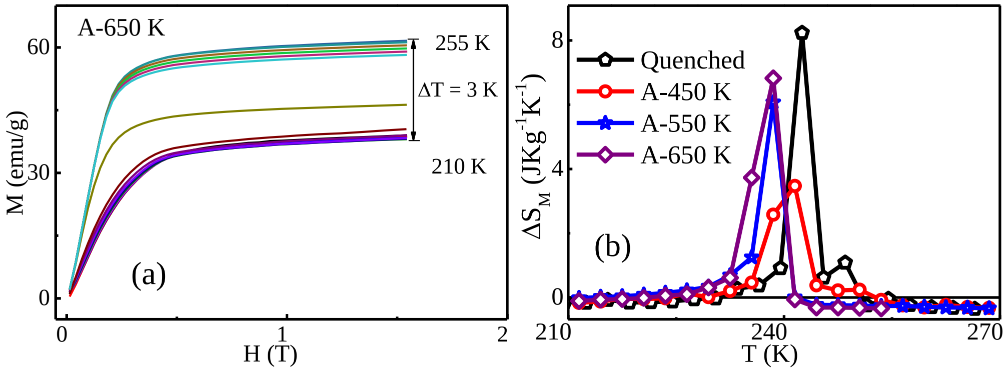

Figure 6.6 (a) M-H curves measured at a temperature interval of 3K for A-650 K, (b) ΔS_M for the field of 1.5 T in $Ni_2Mn_{1.36}Sn_{0.32}$ $Al_{0.32}$ samples annealed at various temperatures.

In section 5.1.1 the magnetic state of the martensitic phase of quenched

$Ni_2Mn_{1.36}Sn_{0.32}Al_{0.32}$ showed freezing of spins as temperature was lowered. Frequency dependent susceptibility showed that this freezing was most probably cluster spin glass type. It was further found that magnetic cluster size showed a dependence on the Al content, decreasing as Al content increased. This was reported to occur due to weakening of FM and AFM interaction in the martensitic phase. As we have seen above that the post quenching annealing influenced the FM and AFM interaction in the martensitic phase, we expect that the various freezing parameters and magnetic cluster size of the system must undergo changes too. Thus we have studied the dynamics of the system using linear and nonlinear ac susceptibilities as mentioned in Chapter 5.

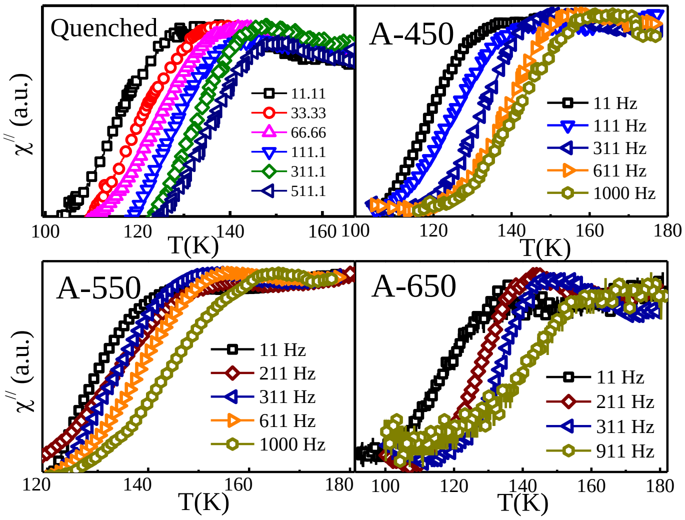

Figure 6.7 Imaginary part ($\chi^{//}$) of ac susceptibility as a function of temperature for quenched and annealed samples.

The in phase ($\chi^{/}$) and out of phase ($\chi^{//}$) components of liner parts of ac susceptibility measurement were performed on the quenched sample and PQA samples in low temperature region below M_F at different frequencies. The $\chi^{/}$ and $\chi^{//}$ data for quenched samples are shown in Figure 5.1 (Chapter 5). The $\chi^{//}$ showed peaks and temperatures corresponding to these were denoted by T_f. The $\chi^{//}$ curves for quenched and annealed samples are shown in Figure 6.7. The peaks of $\chi^{//}$ of annealed samples also shifted to higher temperature as we increased the measurement frequency, indicating that magnetic glassy phase was present in these systems. The frequency depended shifts were analyzed mentioned before in section 5.1.1.The parameter Φ was obtained using the equation

(5-1) and the values are shown in Table 6-1. The values show that after heat treatment the systems were still most probably in spin glass state. The frequency dependence of T_f was analyzed using the dynamic scaling law of equation (5-3). The fittings are shown in the Figure 6.8 and the values obtained are given in Table 6-1. The values obtained for $z\nu$ for annealed samples also lies in the range of spin glass. The large value of $\tau*$ implies that the contribution to freezing comes from the clusters rather than individual spins [35,164]. The $\tau*$ also increased as the post quenching annealing temperature was increased, showing that as the heat treatment temperature was increased the cluster size increased. As the ac susceptibility measurement technique detects response of magnetic moments, the increase in cluster size shows that with heat treatment the size of magnetic cluster increased. Further the electron microscope images of the austenitic phase showed that the grain size did not change upon annealing, thus the increase in magnetic cluster size must be happening due to change in magnetic interaction within a grain.

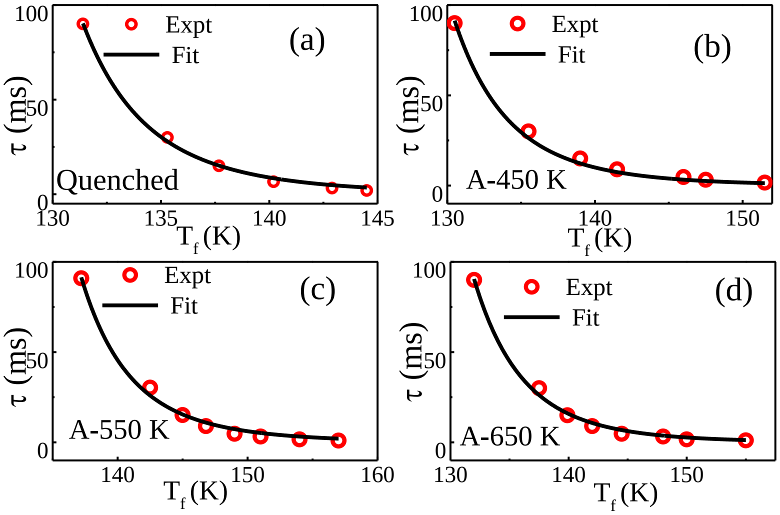

Figure 6.8 Fits to scaling law as a function of temperature for quenched and annealed samples.

Non-liner ac susceptibility measurement was performed to further investigate the changes bought in magnetic state of martensitic phase by heat treatment. Third harmonic of ac susceptibility was measured at different frequencies. The results of χ_3 measurements are given in Figure 6.9. All samples showed shifts in χ_3 with increasing frequency. The frequency dependent shift was small in case of quenched sample. The natures of curves for quenched and annealed samples at low frequency were similar but the natures of curves in case of annealed samples were very different from that of the quenched sample at higher frequencies. χ_3 showed a negative peak at higher frequency and the depth of peak increased as frequencies of measurements were increased in annealed samples. The presence of negative peak in χ_3 is an indication of presence of spin glass in the system [158,165]. But the absence of negative divergence at low frequency and the frequency dependent shift of the χ_3 indicate that the spin glass was not present in the sample and the freezing in these samples are also most probably coming from the progressive blocking of the clusters.

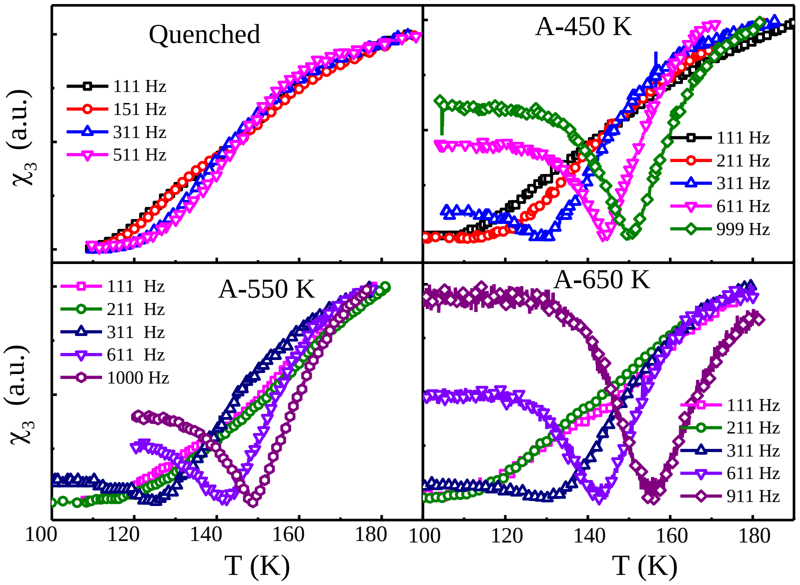

Figure 6.9 Third harmonic (χ_3) of ac susceptibility as the function of temperature for quenched sample and samples annealed at 450 K, 550 K and 650 K.

Quenched sample did not show negative peak even at higher frequencies. In ac susceptibility technique as the measurement frequency is increased, the time scale of relaxation process that can be detected decreases, thus with increasing frequencies we probe regions with smaller relaxation times and smaller spin-spin correlation lengths. As the presence of spin glass is ruled out the negative divergence in the χ_3 may possibly come from the region of random spins without frustration [165]. The presence of the negative divergence only at higher frequencies shows that such regions are smaller in size and their presence in only annealed samples shows that the annealing process helped in the growth of regions with random spins without frustration. On the other hand the nature of low frequency curve remained almost unaltered for quenched and annealed samples, showing that interaction among the cluster of larger size hardly underwent any change with increasing annealing temperature. This results shows that secondary annealing may promote the growth of regions with random spins.

Table 6-1 The martensitic start temperature (M_S), parameter Φ defined by equation (5-1), and τ^* the macroscopic relaxation time and zυ the exponent in equation (5-3) are given here.

Sample	*M_S(K)*	*Φ*	*τ* (s)*	*zν*
Quenched	237.0	0.057	1.8×10^{-6}	5.6
A-450	235.5	0.087	4.9×10^{-6}	7.4
A-550	232.5	0.066	5.2×10^{-6}	6.2
A-650	229.5	0.079	1.4×10^{-5}	8.1

6.2 Effect of High temperature heat treatment

The post quenching heat treatment was performed by cutting some more small pieces from the original sample of composition $Ni_2Mn_{1.36}Sn_{0.28}Al_{0.36}$, and sealing them in quartz tubes. Samples were heat treated at 900 K and 1000 K for 24 hours and slowly cooled down in furnace at 20 K/hr.

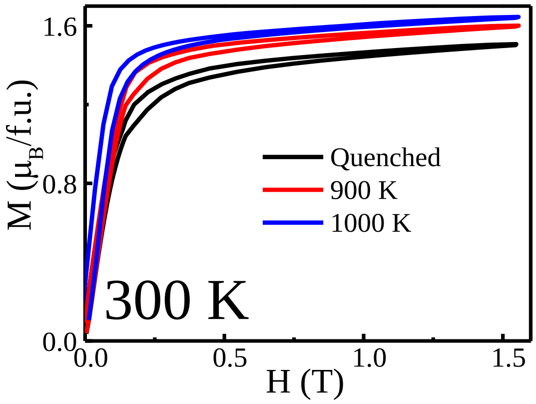

Figure 6.10 M-H of samples of composition $Ni_2Mn_{1.36}Sn_{0.28}Al_{0.36}$ measured at 300 K in μ_B/ f.u.

Figure 6.10 shows data for the magnetization measured till the field of 1.5 T for quenched and samples annealed at 900 K and 1000 K. In Figure 6.10 we see that the magnetization of the sample increased as the post quenching annealing temperature was increased [181]. The saturation magnetization measured for quenched sample, sample annealed at 900 K and 1000 K were 1.50 μ_B/f.u., 1.60 μ_B/f.u. and 1.64 μ_B/f.u.

respectively. The increase in magnetization of the austenitic phase may be attributed to increase in the ordering in the system. The quenched sample was cooled suddenly form 1273 K to room temperature, whereas in post quenching heat treatment sample were slowly cooled form 900 K and 1000 K to room temperature. It is apparent that when sample was slowly cooled the system trends to stabilize into $L2_1$ phase and higher the temperature better was ordering in the system.

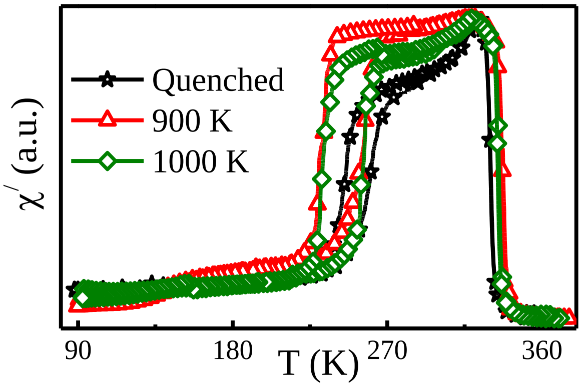

Figure 6.11 $\chi^/$ as function of temperature for quenched and annealed samples of composition $Ni_2Mn_{1.36}Sn_{0.28}Al_{0.36}$.

The real part of ac susceptibility was measured for the samples annealed at 900 K and 1000 K, these are shown in the Figure 6.11 along with that of quenched sample. The $\chi^/$ fell in quenched sample for $M_S < T < T_C$. This was assumed due to higher amount of AFM interaction present in the sample as a result of larger disorder in the quenched sample as mentioned in section 3.1.3. With lowering of temperature the AFM regions pin the FM regions and thus magnetic clusters were not able to respond to the ac driving field leading to fall in $\chi^/$. As the sample was annealed at higher temperature and slowly cooled we find that the fall in the $\chi^/$ of sample for $M_S < T < T_C$ decreased, thus showing that the AFM interaction in the sample was reduced.

The ZFC, FC and FH curves were measured for the samples in a field of 100 Oe and are shown in the Figure 6.12. We see that as the annealing temperature increased the magnetization also increased in the austenitic phase, also the change in magnetization upon structural transformation increased. It can further be seen that with increasing annealing temperature the curve around MT shifted to lower temperature. The M_F was found to be 226 K, 219 K and 215 K for quenched, sample annealed at 900 K and 1000 K respectively. The M_F fell with increasing annealing temperature as the magnetism of austenitic phase increased and it became more stable. As the annealing temperature was increased the bifurcation between ZFC and FC in the austenitic phase decreased. This further shows that the AFM interaction in the austenitic phase in the sample decreased. Apart from these the ΔM value across the phase transformation which was found to be 14 emu/g for quenched sample increased to 15 emu/g for sample annealed at 900 K and to 32 emu/g for the sample annealed at 1000 K. As the sample shows drastic change in ΔM it is expected that MCE in the sample would increase.

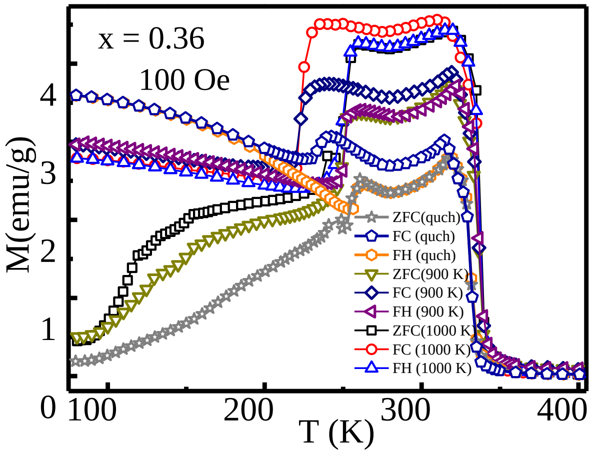

Figure 6.12 ZFC, FC, and FH curves at the field of 100 Oe as a function of temperature for $Ni_2Mn_{1.36}Sn_{0.28}Al_{0.36}$ quenched and annealed samples.

To test this hypothesis, MC effect was measured in these samples using the same protocol as mentioned in Chapter 4 and results are shown in Figure 6.13 along with that of quenched sample. It can be seen that the maximum of ΔS_M increased to more than twice for the sample annealed at 900 K (from 2.4 J kg^{-1} K^{-1} to 6.6 J kg^{-1} K^{-1}) and then fell slightly for the 1000 K annealed sample at 5.1 J kg^{-1} K^{-1}, but the area under the curve increased as the heat treatment temperature was increased. The RC value which was 12.9 J kg^{-1} increased to 15.6 J kg^{-1} for sample annealed at 900 K and to 26.3 J kg^{-1} for sample annealed at 1000 K. These show that even at higher percentage of Al it is possible to get better functional property with a secondary heat treatment performed at much higher temperature than in Ni_2Mn-Al system [64]. It is expected that further work by varying composition may lead to a ductile alloy with large functional properties.

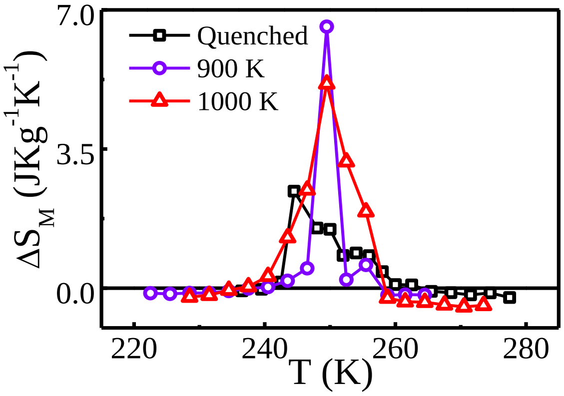

Figure 6.13 Entropy changes of $Ni_2Mn_{1.36}Sn_{0.28}Al_{0.36}$ samples measured after various secondary heat treatments under magnetic field of 1.5 T.

6.3 Discussion

We investigated the effect of low temperature post quenching annealing on the magnetism, structural transformation, magnetocaloric effect and relaxation phenomenon of $Ni_2Mn_{1.36}Sn_{0.32}Al_{0.32}$. The structural transformation temperature of the system decreased as the annealing temperature was increased. The magnetization, peak value of the entropy change and the value of RC initially decreased and then increased as the annealing temperature was increased. Though the ΔS_M fell, and it fell drastically for A-450 sample the peak became wider, that for the RC for A-650 was even more than quenched sample. Frequency dependent susceptibility showed that sample underwent freezing at low temperature and the size of the magnetic cluster increased as the annealing temperature was increased. The frequency dependence of χ_3 further shows that the annealing promotes the growth of AFM regions in the samples.

On the other hand when a high temperature heat treatment was performed on the $Ni_2Mn_{1.36}Sn_{0.28}Al_{0.36}$ sample, the magnetization of the austenitic phase in the sample increased as the annealing temperature was increased and as the result of it the MT temperature of the system fell. It was found that the high temperature heat treatment can increase the MCE in the sample almost two times of the quenched samples. The above effects were found to occur due to increase in the ordering in the sample. Therefore we see that higher temperature annealing promotes ordering, leading to higher MCE.

Chapter 7

Comparison of effect of Sn and Sb on physical properties

We have replaced Al partially with Sb and Sn in Ni-Mn-Al system and investigated effect on magnetism, entropy change and magnetoresistance in the vicinity of martensitic transformation. Both the samples had identical lattice parameters and the Mn contents, that are mostly responsible for magnetism in these systems, yet there is marked change in magnetic and functional properties of these systems. It was found that the magnetization increased in Sb alloy, while entropy change and magnetoresistance decreased compared to Sn alloy. These changes are attributed to the change in antiferromagnetic interaction as a result of variation in the Ni d - Mn d hybridization arising due to presence of different sp element.

In the present chapter we shall compare $Ni_2Mn_{1.36}Sn_{0.40}Al_{0.24}$ and $Ni_2Mn_{1.36}Sb_{0.40}Al_{0.24}$ systems. We will refer to them as Sn and Sb systems further on. The identical composition and lattice parameter of the system make these systems ideal to study the effect of Z atom (Sn and Sb in present case) on the magnetic and functional properties of these systems.

As mentioned in section 1.3.3, main contribution to magnetism in Ni-Mn-Z alloys comes from the magnetic interaction between the Mn atoms. The interaction is sensitive to the distance, is predominantly FM in austenitic phase and is competing FM/AFM in martensitic phase. Recent experimental and theoretical work on Ni_2Mn-In system indicates that the origin of AFM interaction in martensitic phase is superexchange in nature, these interactions mediate through Ni-3d orbital. It is AFM between an Mn atom in regular Mn site and another Mn atom in Z site, but is ferromagnetic when Z is present at its site [29,31]. Khan et al. has shown that replacement of Cr with Mn in $Ni_{50}Mn_{37-x}Cr_xSb_{13}$ (x= 1 to 6) lowers the AFM interaction and argued that it occurs because of weakening of Ni-Mn hybridization [59]. But decrease in Mn content along with increasing Cr content and chances of Cr occupying Ni, Mn and Z site leaves other possibilities which can affect magnetism, wide open. For example previous study by the same author on Ni-Mn-Sb system showed that exchange bias effect increases with increased in Mn content, showing that change in AFM interaction in Cr replaced system could possibly be outcome of decreasing Mn content [37]. To avoid confusion, here we have studied systems with Sn and Sb system, where Mn and Ni content both remained the same and system had almost identical lattice parameters. Hence such study will make comparison of Ni-Mn hybridization more pertinent and may lead to better understanding of magnetism in Ni-Mn-Z system.

Usually the comparison of magnetic property of the system with different fractions of Z element is hindered by the fact that the electron concentration and Mn-Mn distance (lattice parameter) both changes with change in composition. Since these are kept same here, our study will help better understand the underlying mechanism of the functional capabilities thus may pave the way for development of better FSMA.

7.1 Comparison

The resistivity measurements were performed using four probe techniques in 10 T and 14 T setup from Cryogenics.

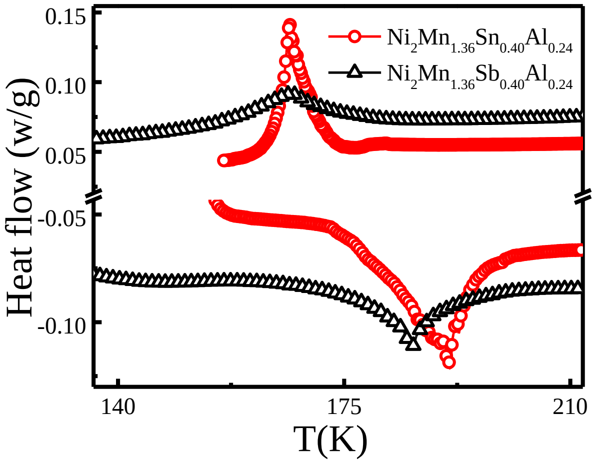

Figure 7.1 DSC curves obtained for Sn and Sb based samples in cooling and heating cycles performed at the rate of 10 K/min.

The XRD patterns obtained at room temperature for Sn and Sb samples were given in the Chapter 3. Rietveld refinement of the sample showed that it was in austenitic phase with L2$_1$ structure and lattice parameter of 0.593 nm for both samples [35]. Structural transformation temperatures were determined form DSC curves which are shown together in Figure 7.1 for comparison. The M_s, M_F, A_S and A_F temperatures were found to be 189 K, 154 K, 158 K and 207 K respectively for $Ni_2Mn_{1.36}Sb_{0.40}Al_{0.24}$ and were 171K, 158 K, 168K, and 196K, respectively for $Ni_2Mn_{1.36}Sn_{0.40}Al_{0.24}$. The M_S of the Sb alloy is slightly higher than that of Sn alloy [35]. This was consistent with the fact that with increase in electron concentration the transformation temperature increases.

As per a phenomenological theory of martensitic transformation, thermal hysteresis at MT with higher slope indicates presence of boundary friction, elastic strain energy and interfacial energy [98,134]. It was found that thermal hysteresis at MT in case of Sn system was 10 K ($\Delta T_H = A_S - M_F$) where as it was 4 K for Sb system. Narrower thermal hysteresis in case of Sb alloy indicates that there is lesser boundary friction compared to Sn alloy. The slope of transformation was found to be greater in case of Sb alloy. The larger elastic strain energy and interfacial energy resist the martensitic and reverse transformation, thus increasing the slope of transformation. This indicates that Sb system will have better phase transition response time and more strain energy across MT [98,134].

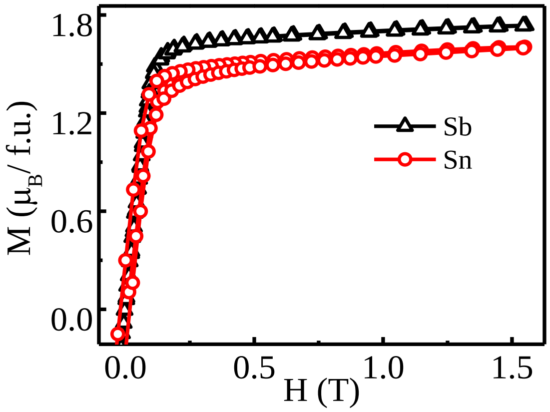

Figure 7.2 M-H measured at 300 K for Sn and Sb samples.

The T_C of Sb alloy was determined to be 355 K, whereas that of Sn alloy was 326 K [35] (Sections 3.1 and 3.2). Higher T_C in case of Sb alloy shows that Sb in the system enhanced ferromagnetic exchange. M-H measurements were performed at 300 K up to a field of 1.5 T for both the samples and the obtained results are shown in Figure 7.2. It can be seen that the magnetic moment of Sn system is 1.60 μ_B /f .u. and that of Sb system is 1.73 μ_B /f .u., which is higher in case of Sb system. As mentioned earlier in Ni_2Mn-Z system magnetism is mostly carried by Mn atom. Both the systems were in ordered $L2_1$ structures with the same Mn-Mn distances and contents of Ni and Mn were same for both, so only difference is that they have different atoms at the Z sites. The presence of different atoms at Z site affected p-d hybridization between Ni and Z (also Ni and Mn) differently, which in turn affected the interaction among the different Mn atoms. This possibly gave rise to different magnetizations in these two systems.

These samples transform from a predominantly FM state (austenitic) to a state with lower magnetization state (martensitic) within a window of few Kelvins. This results in large change in magnetization (ΔM) across martensitic transformation giving rise to properties like magnetocaloric effect and giant magnetoresistance. The magnetocaloric effect was calculated from isothermal magnetization measurement using modified Maxwell's relation as given in the Section 4.1.1 and 4.1.2 for these samples. The obtained value of entropy change (ΔS_M) is given in Figure 7.3 for Sn and Sb alloys. The maximum of ΔS_M

obtained in case of Sn alloy was 5.6 $Jkg^{-1}K^{-1}$ and was 0.365 $Jkg^{-1}K^{-1}$ in Sb alloy. The refrigerant capacity (RC) values for the field of 1.5 T were 25.2 and 6.8 J kg^{-1} respectively for Sn and Sb alloys as shown in Section 4.1.1and 4.1.2.

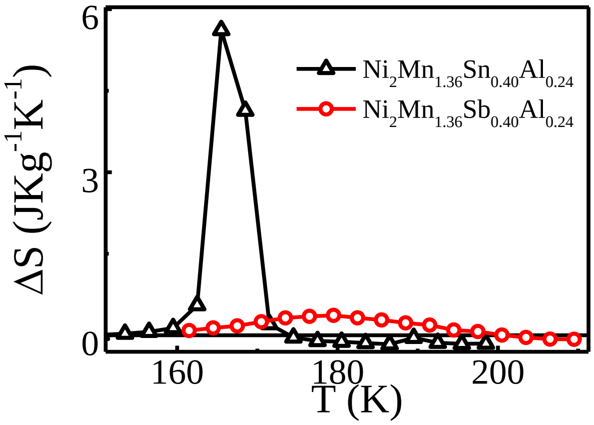

Figure 7.3 Entropy changes due to application of field of 1.5 T calculated from modified Maxwell relation.

The ΔM obtained from the M-H curve in Sn alloy was 19.5 emu/g and in the other case was only 4 emu/g (Section 4.1.1 and 4.1.2), it can be seen that even though magnetization was higher in case of Sb system the value of ΔM was much smaller. As mentioned earlier increased Ni-Mn hybridization leads to AFM interaction, between the Mn atoms occupying Mn site and Z site, in martensitic phase. The replacement of Sn with Sb most probably weakens the hybridization between the Mn-Ni-Mn thus resulting in enhancement of ferromagnetism in the Sb alloy compared to the Sn alloy. The effect is more pronounced in the martensitic phase and as a result of it the value of ΔM is lower in case of Sb alloy. The lower value of ΔM thus results in lower value of ΔS_M and RC in the Sb sample.

To throw some more light in this matter, transport measurements on these samples were done next. The resistivity measurements were performed in cooling and heating cycles for these samples. Figure 7.4 (a) and (b) shows the curves obtained when resistivity measurements performed in zero applied dc magnetic field for both, and in fields of 10 T and 14 T for Sn and Sb alloy respectively. The resistivity showed sharp changes upon structural transformations. Resistivity of the martensitic phase is higher than austenitic phase by 37 % and 32 % for Sn and Sb alloy. The structural transformation to martensitic phase enhanced the AFM interaction, this changes the density of state at Fermi surface. The different magnetic ordering (AFM) and crystal structure in the martensitic phase compared to austenitic phase established different type of electronic band structures. This gives rise to super zone gap upon martensitic transformation thus leading to increase in resistance [59,183,184]. The lower value of change in resistivity across MT ($\Delta\rho_{M-A}$) in Sb alloy shows that change in AFM interaction upon MT is small in this system. The resistivity curve measured under non zero field, shifted to lower temperature. The shift is large in Sn alloy compared to Sb alloy. The lowering of transformation temperature with field can be understood from Clausius-Clapeyron relation [18]. As the magnetization change in Sb alloy was much smaller than Sn alloy, the resulting shift in transformation temperature is also lower. The change in MT temperature with field also results is large magnetoresistance (MR= $[\rho(H, T) - \rho(0, T]/\rho(0, T))$ [185,186]. The MR obtained for both samples are given in the Figure 7.4 (c) and (d). For Sn alloy the maximum MR of 36 % is observed for the applied field of 10 T whereas the maximum for Sb alloy much lower at 5 % for the field of 14 T, even though both alloys have slightly different change of $\Delta\rho_{M-A}$ upon MT. Therefor the MR results are consistent with the magnetic measurements.

So, we see that upon substituting Sn with Sb, the overall magnetization of austenitic phase increased but the change in magnetization across MT decreased. The effect of substitution is even more pronounced on the functional properties like MCE and MR where they decreased by an order of magnitude. The increase in magnetization of Sb alloy shows that the AFM interaction in the sample weakened in austenitic phase. The lowering of ΔM, MCE and MR further shows that the decrease in AFM interaction was more pronounced in martensitic phase than in austenitic phase. The AFM interaction in martensitic phase had been attributed to Ni 3*d* - Mn 3*d* hybridization, which was sensitive to distance. The XRD results showed that the lattice parameters did not change upon substitution of Sn with Sb. The replacement of Sn with Sb led to increase in the density of electrons in conduction band, it was argued by Khan et al. that change in electron concentration influenced metallic radii of Mn [59,187]. The radii of Mn decreased with increase in electron concentration which would reduce the Ni-Mn distance compared to

Sn system then in Sb system, thus the Mn-Ni-Mn hybridization decreased, reducing the AFM interaction in the Sb sample.

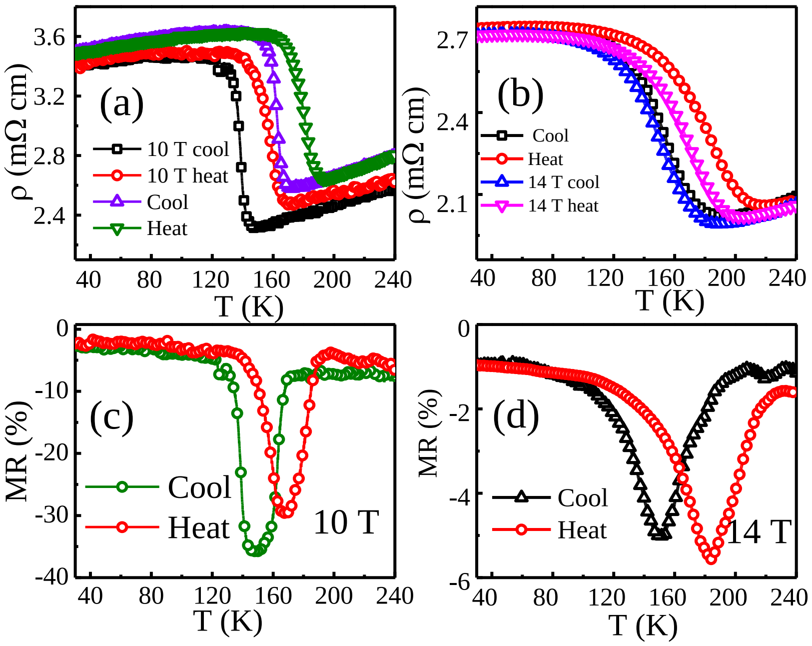

Figure 7.4 (a) and (b) shows resistivity measurement performed in the zero applied dc magnetic field and field of 10 T and 14 T for Sn and Sb alloy respectively. (c) and (d) shows MR obtained for respective alloys.

7.2 Discussion

In summary, we have shown that it is possible to obtain large fraction $L2_1$ phase by replacing Al with other *sp* elements having larger radii. Such replacement also offers us a way to control the magnetic and functional properties of these systems. We have also shown that the different s*p* element can change the Ni-Mn and Ni-Z hybridization and thus effect the magnetism and related properties. The presence of Sb weakens the AFM interaction (hybridization) in sample leading to increase in magnetism of both austenitic and martensitic phase, the effect being more pronounced in martensitic phase, leading to decrease in magnitude of ΔM, MCE and MR by more than an order of magnitude.

Chapter 8

Conclusion

In this chapter we summarize all the findings in the previous chapters and conclude. We also indicate some of the areas where future work can be continued.

8.1 Conclusion

We have investigated in the present thesis the effect that the Al replacement has on the Ni-Mn-Z (Z is Sn, Sb and In) class of ferromagnetic shape memory alloys. We prepared alloys with composition of $Ni_2Mn_{1.36}Z_{0.64-x}Al_x$, where x was varied from 0.24 to 0.40 in step of 0.04 depending on Z. Our aim was to develop a system intermediate to pure Z and Al based systems so that the resultant system had the better functional capabilities.

We prepared our samples using a tri-arc melting furnace and they were characterized using various techniques as mentioned in the Chapter 2. The X-ray diffraction patterns showed that the replacement of Al with Z lead to stabilization of $L2_1$ phase in the system. All samples showed martensitic transformations thus showing that Al replacement did not suppress it. It was further found that the replacement shifted the MT temperature towards room temperature. The substitution was found to affect the magnetism differently in various systems. In the Sn based system the magnetism of the austenitic phase fell as the Al content was increased and was also found that with increase in the Al, the undesirable B2 phase in the system increased.

The functional properties of the system like magnetocaloric effect, magnetoresistance and exchange bias effect were studied in the Chapter 4. The MCE effect was measured in a field of 1.5 T. The replacement of Al by the Sn was found to enhance the MCE in the sample to almost twice of that of the pure Sn system. We also showed that the measurement of ΔS_M using an indirect method of magnetization measurement agreed with more direct method of calorimetric measurements in our samples, so showing that there was no over-estimation of the ΔS_M. The Sb replacement system did not display the large inverse MCE as observed in Sn replaced system but nevertheless the conventional MCE observed in the former system was found to have better RC values then the Sn based system. The system also displayed the EB effect which may find application in future spintronic devices. Thus overall the Al replacement in the system enhanced the functional capabilities of the system.

The dynamics of the low temperature martensitic phase was studied in the Chapter 5, using both ac and dc magnetization measurement techniques. The linear ac susceptibility measurements showed that the system most probably froze in the spin glass state and the frozen entities were magnetic clusters rather than individual spins. It was also observed that the cluster size showed dependence on the concentration of Al for Sn based system, decreasing with increase in Al content. The nonlinear third harmonic measurements in the Sb and In based systems did not show the typical signature of the spin glass. Thus the freezing in the systems most probably came from progressive blocking of the magnetic clusters rather than due to spin glass.

The dynamical study with dc magnetization in Sn and Sb based system showed similar behavior where the (H, T) phase diagram of the system broke down above internal exchange bias field. It was found that above and below the breakdown the system had different dynamics. The Sn based system was found to unfreeze along the transverse line in the low field below the breakdown point whereas the In based system did not display any such behavior even at higher field and the cluster in these cases relaxed along the longitudinal line.

The magnetocaloric effect was found to decrease as the Al content increased in the Sn based system. To enhance the MCE we performed low and high temperature secondary heat treatments on $Ni_2Mn_{1.36}Sn_{0.32}Al_{0.32}$ and $Ni_2Mn_{1.36}Sn_{0.28}Al_{0.36}$ respectively. It is reported in the Chapter 6. While the low temperature annealing in $Ni_2Mn_{1.36}Sn_{0.32}Al_{0.32}$ decreased the peak value of entropy change, the refrigerant capacity of the sample was found to increase as compared to quenched sample. Frequency dependent susceptibility showed that samples underwent freezing at low temperature and the sizes of the magnetic clusters increased as the annealing temperatures were increased. The frequency dependence of χ_3 further showed that the dependency most probably came from the random freezing of clusters without frustration. The high temperature heat treatment on the other hand of $Ni_2Mn_{1.36}Sn_{0.28}Al_{0.36}$, increased the MCE in the sample almost two times of that of quenched samples. The effects arising due to secondary heat treatments were reported to occur due to increase in the ordering in the sample. It was thus shown that the better functional properties can be obtained even at higher concentration of Al in Sn based system.

We have compared the nature of structural transformation, magnetism, magnetocaloric effect and magnetoresistance for the samples with composition of $Ni_2Mn_{1.36}Sn_{0.40}Al_{0.24}$

and $Ni_2Mn_{1.36}Sb_{0.40}Al_{0.24}$ in Chapter 7. We have shown the effect a *sp* element can have on the magnetism and properties like MCE and MR. The presence of Sb weakened the AFM interaction in sample leading to increase in magnetism of both austenitic and martensitic phase. This effect being more pronounced in martensitic phase, led to decrease in magnitude of ΔM, MCE and MR by more than an order of magnitude.

Thus we found that Al replacement in Ni-Mn-Z based system gave a system which has better properties than the parent system. The Al replacement provided a cheaper alternative to the costly Z elements (Sn, Sb and In). The properties of systems and there transformation temperatures can be easily controlled by changing Al content and also by giving proper heat treatment. Thus overall we get systems which have superior properties to Ni-Mn-Al system. The dynamic studies offer us insight into the possible origin of magnetism in Ni-Mn-Z systems and further showed that freezing in the system in martensitic phase was mostly outcome of progressive blocking of the magnetic cluster and not of spin glass nature.

8.2 Future scope

In our investigations we measured mostly the dynamics and functional properties of the systems prepared. The effect of substitution of Al on the mechanical property of the system could not be studied for the lack of the facilities and time. Further the substitution was only carried out in the $Ni_2Mn_{1.36}Z_{0.64}$ alloy with Z as Sn, Sb and In. While the substitution in Sn and Sb system gave systematic and desirable results, the properties of In system was inferior owing to structural transition taking place above the magnetic transition. Thus different composition of In system may be tried for substitution of Al to achieve better functional properties in them.

References

[1] K. Ullakko, J. K. Huang, V. V. Kokorin, and R. C. O'Handley, Scr. Mater. **36**, 1133 (1997).

[2] K. Otsuka and C. Wayman, editors, *Shape Memory Materials* (Cambridge University Press, Cambridge, 1999).

[3] D. C. Lagoudas, *Shape Memory Alloys: Modeling and Engineering Applications* (Springer, 2008).

[4] Q. Pan and R. D. James, J. Appl. Phys. **87**, 4702 (2000).

[5] Y. W. Lai, N. Scheerbaum, D. Hinz, O. Gutfleisch, R. Schäfer, L. Schultz, and J. McCord, Appl. Phys. Lett. **90**, 192504 (2007).

[6] T. W. Duerig, K. N. Melton, D. Stöckel, and C. M. Wayman, *Engineering Aspects of Shape Memory Alloys* (Elsevier, 1990).

[7] H. Morito, A. Fujita, K. Fukamichi, R. Kainuma, K. Ishida, and K. Oikawa, Appl. Phys. Lett. **81**, 1657 (2002).

[8] P. Molnar, P. Sittner, V. Novak, J. Prokleska, V. Sechovsky, B. Ouladdiaf, S. P. Hanulla, and O. Heczko, J. Phys. Condens. Matter **20**, 104224 (2008).

[9] H. Morito, K. Oikawa, A Fujita, K. Fukamichi, R. Kainuma, and K. Ishida, J. Phys. Condens. Matter **21**, 256002 (2009).

[10] S. Aich, S. Das, I. A. Al-Omari, P. Alagarsamy, S. G. Chowdhury, M. Chakraborty, J. E. Shield, and D. J. Sellmyer, J. Appl. Phys. **105**, 07A943 (2009).

[11] K. Ullakko, J. Mater. Eng. Perform. **5**, 405 (1996).

[12] J. Enkovaara, A. Ayuela, A. T. Zayak, P. Entel, L. Nordström, M. Dube, J. Jalkanen, J. Impola, and R. M. Nieminen, Mater. Sci. Eng. A **378**, 52 (2004).

[13] P. K. Mukhopadhyay, M. Karmakar, B. Rajini Kanth, and S. N. Kaul, J. Alloys Compd. **577**, S119 (2013).

[14] K. Ullakko, J. K. Huang, C. Kantner, R. C. O'Handley, and V. V. Kokorin, Appl. Phys. Lett. **69**, 1966 (1996).

[15] A. Planes, L. Mañosa, and M. Acet, J. Phys. Condens. Matter **21**, 233201 (2009).

[16] H. Chopra, C. Ji, and V. Kokorin, Phys. Rev. B **61**, R14913 (2000).

[17] O. Heczko, A. Sozinov, and K. Ullakko, IEEE Trans. Magn. **36**, 3266 (2000).

[18] R. Kainuma, Y. Imano, W. Ito, Y. Sutou, H. Morito, S. Okamoto, O. Kitakami, K. Oikawa, A. Fujita, T. Kanomata, and K. Ishida, Nature **439**, 957 (2006).

[19] J. Kim, F. Inaba, T. Fukuda, and T. Kakeshita, Acta Mater. **54**, 493 (2006).

[20] X. Moya, L. Mañosa, A. Planes, T. Krenke, E. Duman, M. Acet, and E. F. Wassermann, J. Magn. Magn. Mater. **316**, e572 (2007).

[21] T. Krenke, M. Acet, E. Wassermann, X. Moya, L. Mañosa, and A. Planes, Phys. Rev. B **73**, 1 (2006).

[22] A. P. Kazakov, V. N. Prudnikov, A. B. Granovsky, A. P. Zhukov, J. Gonzalez, I. Dubenko, A. K. Pathak, S. Stadler, and N. Ali, Appl. Phys. Lett. **98**, 131911 (2011).

[23] R. Ranjan, S. Singh, H. Boysen, D. Trots, S. Banik, A. M. Awasthi, P. K. Mukhopadhyay, and S. R. Barman, J. Appl. Phys. **106**, 033510 (2009).

[24] S. Aksoy, M. Acet, E. F. Wassermann, T. Krenke, X. Moya, L. Mañosa, A. Planes, and P. P. Deen, Philos. Mag. **89**, 2093 (2009).
[25] M. Khan, N. Ali, and S. Stadler, J. Appl. Phys. **101**, 053919 (2007).
[26] E. Şaşıoğlu, L. Sandratskii, and P. Bruno, Phys. Rev. B **77**, 064417 (2008).
[27] Y. Noda and Y. Ishikawa, J. Phys. Soc. Japan **40**, 690 (1976).
[28] K. Tajima, Y. Ishikawa, P. J. Webster, M. W. Stringfellow, D. Tocchetti, and K. R. A. Zeabeck, J. Phys. Soc. Japan **43**, 483 (1977).
[29] K. R. Priolkar, D. N. Lobo, P. A. Bhobe, S. Emura, and A. K. Nigam, EPL Europhysics Lett. **94**, 38006 (2011).
[30] V. Buchelnikov, P. Entel, S. Taskaev, V. Sokolovskiy, A. Hucht, M. Ogura, H. Akai, M. Gruner, and S. Nayak, Phys. Rev. B **78**, 184427 (2008).
[31] K. R. Priolkar, P. A. Bhobe, D. N. Lobo, S. W. D'Souza, S. R. Barman, A. Chakrabarti, and S. Emura, Phys. Rev. B **87**, 144412 (2013).
[32] E. Şaşıoğlu, L. Sandratskii, and P. Bruno, Phys. Rev. B **70**, 1 (2004).
[33] P. J. Brown, A. P. Gandy, K. Ishida, R. Kainuma, T. Kanomata, K. U. Neumann, K. Oikawa, B. Ouladdiaf, and K. R. A. Ziebeck, J. Phys. Condens. Matter **18**, 2249 (2006).
[34] P. Lázpita, J. M. Barandiarán, J. Gutiérrez, J. Feuchtwanger, V. A. Chernenko, and M. L. Richard, New J. Phys. **13**, 033039 (2011).
[35] S. Agarwal, S. Banerjee, and P. K. Mukhopadhyay, J. Appl. Phys. **114**, 133904 (2013).
[36] H. C. Xuan, Q. Q. Cao, C. L. Zhang, S. C. Ma, S. Y. Chen, D. H. Wang, and Y. W. Du, Appl. Phys. Lett. **96**, 202502 (2010).
[37] M. Khan, I. Dubenko, S. Stadler, and N. Ali, Appl. Phys. Lett. **91**, 072510 (2007).
[38] S. Chatterjee, S. Giri, S. De, and S. Majumdar, Phys. Rev. B **79**, 092410 (2009).
[39] E. Wachtel, F. Henninger, and B. Predel, J. Magn. Magn. Mater. **38**, 305 (1983).
[40] T. Miyamoto, W. Ito, R. Y. Umetsu, R. Kainuma, T. Kanomata, and K. Ishida, Scr. Mater. **62**, 151 (2010).
[41] R. Kainumal, (2000).
[42] R. W. Overholser, M. Wuttig, and D. a. Neumann, Scr. Mater. **40**, 1095 (1999).
[43] V. V. Khovailo, T. Takagi, A. N. Vasilev, H. Miki, M. Matsumoto, and R. Kainuma, Phys. Status Solidi **183**, R1 (2001).
[44] V. Sánchez-Alarcos, V. Recarte, J. I. Pérez-Landazábal, C. Gómez-Polo, and J. a. Rodríguez-Velamazán, Acta Mater. **60**, 459 (2012).
[45] V. Sánchez-Alarcos, V. Recarte, J. I. Pérez-Landazábal, and G. J. Cuello, Acta Mater. **55**, 3883 (2007).
[46] H. C. Xuan, D. H. Wang, C. L. Zhang, Z. D. Han, B. X. Gu, and Y. W. Du, Appl. Phys. Lett. **92**, 102503 (2008).
[47] R. L. Wang, J. B. Yan, L. S. Xu, V. V. Marchenkov, S. S. Chen, S. L. Tang, and C. P. Yang, Solid State Commun. **151**, 1196 (2011).
[48] A. K. Pathak, I. Dubenko, J. C. Mabon, S. Stadler, and N. Ali, J. Phys. D. Appl. Phys. **42**, 045004 (2009).
[49] S. Chatterjee, S. Giri, S. De, and S. Majumdar, J. Alloys Compd. **503**, 273 (2010).
[50] Z. H. Liu, S. Aksoy, and M. Acet, J. Appl. Phys. **105**, 033913 (2009).
[51] A. C. Abhyankar, Y. T. Yu, Y. K. Kuo, G. W. Huang, and C. S. Lue, Intermetallics **18**, 2090 (2010).

[52] L. Ma, H. W. Zhang, S. Y. Yu, Z. Y. Zhu, J. L. Chen, G. H. Wu, H. Y. Liu, J. P. Qu, and Y. X. Li, Appl. Phys. Lett. **92**, 032509 (2008).
[53] R. Kainuma, Y. Imano, W. Ito, H. Morito, Y. Sutou, K. Oikawa, A. Fujita, K. Ishida, S. Okamoto, O. Kitakami, and T. Kanomata, Appl. Phys. Lett. **88**, 192513 (2006).
[54] S. J. Murray, M. Marioni, S. M. Allen, R. C. O'Handley, and T. A. Lograsso, Appl. Phys. Lett. **77**, 886 (2000).
[55] W. Ito, R. Y. Umetsu, R. Kainuma, T. Kakeshita, and K. Ishida, Scr. Mater. **63**, 73 (2010).
[56] X. Xu, W. Ito, M. Tokunaga, R. Y. Umetsu, R. Kainuma, and K. Ishida, Mater. Trans. **51**, 1357 (2010).
[57] R. Y. Umetsu, K. Ito, W. Ito, K. Koyama, T. Kanomata, K. Ishida, and R. Kainuma, J. Alloys Compd. **509**, 1389 (2011).
[58] A. K. Nayak, K. G. Suresh, and A. K. Nigam, Appl. Phys. Lett. **96**, 112503 (2010).
[59] M. Khan, I. Dubenko, S. Stadler, J. Jung, S. S. Stoyko, A. Mar, A. Quetz, T. Samanta, N. Ali, and K. H. Chow, Appl. Phys. Lett. **102**, 112402 (2013).
[60] A. Fujita, K. Fukamichi, F. Gejima, R. Kainuma, and K. Ishida, Appl. Phys. Lett. **77**, 3054 (2000).
[61] R. Kainuma, F. Gejima, Y. Sutou, I. Ohnuma, and K. Ishida, Mater. Trans. - JIM **41**, 943 (2000).
[62] H. E. Karaca, I. Karaman, B. Basaran, Y. Ren, Y. I. Chumlyakov, and H. J. Maier, Adv. Funct. Mater. **19**, 983 (2009).
[63] X. Moya, L. Mañosa, A. Planes, T. Krenke, M. Acet, M. Morin, J. Zarestky, and T. Lograsso, Phys. Rev. B **74**, 024109 (2006).
[64] M. Acet, E. Duman, E. F. Wassermann, L. Mañosa, and A. Planes, J. Appl. Phys. **92**, 3867 (2002).
[65] Y. Sutou, I. Ohnuma, R. Kainuma, and K. Ishida, Metall. Mater. Trans. A **29**, 2225 (1998).
[66] E. Wachtel, F. Henninger, and B. Predel, J. Magn. Magn. Mater. **38**, 305 (1983).
[67] Y. Sutou, Y. Imano, N. Koeda, T. Omori, R. Kainuma, K. Ishida, and K. Oikawa, Appl. Phys. Lett. **85**, 4358 (2004).
[68] D. L. Schlagel, W. M. Yuhasz, K. W. Dennis, R. W. McCallum, and T. a. Lograsso, Scr. Mater. **59**, 1083 (2008).
[69] D. L. Schlagel, R. W. McCallum, and T. A. Lograsso, J. Alloys Compd. **463**, 38 (2008).
[70] P. Y. Z. Vitalij K. Pecharsky, *Fundamentals of Powder Diffraction and Structural Characterization of Materials* (Springer US, Boston, MA, 2009).
[71] *FULLPROF [http://www.ill.eu/sites/fullprof/]*.
[72] K. R. A. Ziebeck and P. J. Webster, J. Phys. Chem. Solids **35**, 1 (1974).
[73] Y. Takamura, R. Nakane, and S. Sugahara, J. Appl. Phys. **107**, 09B111 (2010).
[74] Y. Leng, *Materials Characterization: Introduction to Microscopy and Spectroscopic Methods* (JohnWiley & Sons (Asia) Pte Ltd, Singapore, 2008).
[75] P. Gabbott, editor, *Principles and Applications of Thermal Analysis* (John Wiley & Sons, 2008).
[76] H. K. D. H. Bhadeshia, [http://www.uzaktanegitimplatformu.com].

[77] J. Marcos, F. Casanova, X. Batlle, A. Labarta, A. Planes, and L. Mañosa, Rev. Sci. Instrum. **74**, 4768 (2003).

[78] M. Youssif, A. Bahgat, and I. Ali, Egypt. J. Solids (2000).

[79] R. A. Hein, T. L. Francavilla, and D. H. Liebenberg, *Magnetic Susceptibility of Superconductors and Other Spin Systems* (Springer, 1991).

[80] [http://en.wikipedia.org/wiki/Vibrating_sample_magnetometer].

[81] B. D. Cullity and C. D. Graham, *Introduction to Magnetic Materials* (Wiley, 2009).

[82] M. McElfresh, *Fundamentals of Magnetism and Magnetic Measurements: Featuring Quantum Design's Magnetic Property Measurement System* (Quantum Design, USA, 1994).

[83] J. Clarke and A. I. Braginski, *The SQUID Handbook: Fundamentals and Technology of SQUIDs and SQUID Systems, Volume 1* (John Wiley & Sons, 2006).

[84] *Low Level Measurements Handbook*, 6th ed. (Keithley Instruments, USA, 2004).

[85] K. T. Jacob, S. Raj, and L. Rannesh, Int. J. Mater. Res. **98**, 776 (2007).

[86] A. Denton and N. Ashcroft, Phys. Rev. A **43**, 3161 (1991).

[87] L. Chen, F. X. Hu, J. Wang, J. Shen, J. R. Sun, B. G. Shen, J. H. Yin, L. Q. Pan, and Q. Z. Huang, J. Appl. Phys. **109**, 07A939 (2011).

[88] T. Inoue, S. Morito, Y. Murakami, K. Oda, and K. Otsuka, Mater. Lett. **19**, 33 (1994).

[89] L. Mañosa, X. Moya, A. Planes, O. Gutfleisch, J. Lyubina, M. Barrio, J. L. Tamarit, S. Aksoy, T. Krenke, and M. Acet, Appl. Phys. Lett. **92**, 012515 (2008).

[90] V. A. Chernenko, Scr. Mater. **40**, 523 (1999).

[91] M. Khan, I. Dubenko, S. Stadler, and N. Ali, Appl. Phys. Lett. **91**, 072510 (2007).

[92] X. H. Huang, J. F. Ding, Z. L. Jiang, Y. W. Yin, Q. X. Yu, and X. G. Li, J. Appl. Phys. **106**, 083904 (2009).

[93] T. Bitoh, K. Ohba, M. Takamatsu, T. Shirane, and S. Chikazawa, J. Phys. Soc. Japan **64**, 1305 (1995).

[94] J. Barandiarán, V. Chernenko, P. Lázpita, J. Gutiérrez, and J. Feuchtwanger, Phys. Rev. B **80**, 104404 (2009).

[95] P. A. Lee, Rev. Mod. Phys. **57**, 287 (1985).

[96] V. Sechovský, L. Havela, K. Prokeš, H. Nakotte, F. R. de Boer, and E. Brück, J. Appl. Phys. **76**, 6913 (1994).

[97] V. K. Srivastava, R. Chatterjee, and R. C. O'Handley, Appl. Phys. Lett. **89**, 222107 (2006).

[98] J. Dubowik, K. Załęski, I. Gościańska, H. Głowiński, and a. Ehresmann, Appl. Phys. Lett. **100**, 162403 (2012).

[99] V. K. Sharma, M. K. Chattopadhyay, R. Kumar, T. Ganguli, P. Tiwari, and S. B. Roy, J. Phys. Condens. Matter **19**, 496207 (2007).

[100] P. J. Brown, A. P. Gandy, K. Ishida, W. Ito, R. Kainuma, T. Kanomata, K. U. Neumann, K. Oikawa, B. Ouladdiaf, A. Sheikh, and K. R. a Ziebeck, J. Phys. Condens. Matter **22**, 096002 (2010).

[101] S. Agarwal and P. K. Mukhopadhyay, in *PROCEEDING Int. Conf. Recent TRENDS Appl. Phys. Mater. Sci. RAM 2013* (AIP Publishing, 2013), p. 977.

[102] S. Chatterjee, S. Giri, S. Majumdar, A. K. Deb, S. K. De, and V. Hardy, J. Phys. Condens. Matter **19**, 346213 (2007).
[103] N. V Rama Rao, R. Gopalan, V. Chandrasekaran, and K. G. Suresh, J. Phys. D. Appl. Phys. **42**, 065002 (2009).
[104] H. C. Xuan, Y. X. Zheng, S. C. Ma, Q. Q. Cao, D. H. Wang, and Y. W. Du, J. Appl. Phys. **108**, 103920 (2010).
[105] C. Seguí, V. A. Chernenko, J. Pons, E. Cesari, V. Khovailo, and T. Takagi, Acta Mater. **53**, 111 (2005).
[106] S. Chatterjee, S. Giri, S. Majumdar, and S. K. De, J. Magn. Magn. Mater. **320**, 617 (2008).
[107] Y. Noda, S. Shapiro, G. Shirane, Y. Yamada, and L. Tanner, Phys. Rev. B **42**, 10397 (1990).
[108] J. Pons, V. A. Chernenko, R. Santamarta, and E. Cesari, Acta Mater. **48**, 3027 (2000).
[109] J. L. Sánchez Llamazares, T. Sanchez, J. D. Santos, M. J. Pérez, M. L. Sanchez, B. Hernando, L. Escoda, J. J. Suñol, and R. Varga, Appl. Phys. Lett. **92**, 012513 (2008).
[110] B. M. Wang, Y. Liu, L. Wang, S. L. Huang, Y. Zhao, Y. Yang, and H. Zhang, J. Appl. Phys. **104**, 043916 (2008).
[111] V. Sharma, M. Chattopadhyay, and S. Roy, Phys. Rev. B **76**, 3 (2007).
[112] P. A. Bhobe, K. R. Priolkar, and A. K. Nigam, J. Phys. D. Appl. Phys. **41**, 235006 (2008).
[113] R. Y. Umetsu, A. Fujita, W. Ito, T. Kanomata, and R. Kainuma, J. Phys. Condens. Matter **23**, 326001 (2011).
[114] A. K. Pathak, B. R. Gautam, I. Dubenko, M. Khan, S. Stadler, and N. Ali, J. Appl. Phys. **103**, 07F315 (2008).
[115] L. Mañosa, D. González-Alonso, A. Planes, E. Bonnot, M. Barrio, J.-L. Tamarit, S. Aksoy, and M. Acet, Nat. Mater. **9**, 478 (2010).
[116] Z. D. Han, D. H. Wang, C. L. Zhang, H. C. Xuan, B. X. Gu, and Y. W. Du, Appl. Phys. Lett. **90**, 042507 (2007).
[117] V. K. Sharma, M. K. Chattopadhyay, K. H. B. Shaeb, A. Chouhan, and S. B. Roy, Appl. Phys. Lett. **89**, 222509 (2006).
[118] S. Giri, M. Patra, and S. Majumdar, J. Phys. Condens. Matter **23**, 073201 (2011).
[119] A. M. Tishin and Y. I. Spichkin, *The Magnetocaloric Effect and Its Applications* (Institute of Physics, Bristol, 2003).
[120] X. Moya, L. Mañosa, A. Planes, S. Aksoy, M. Acet, E. Wassermann, and T. Krenke, Phys. Rev. B **75**, 184412 (2007).
[121] E. Brück, Handb. Magn. Mater. **17**, 235 (2007).
[122] J. Liu, T. Gottschall, K. P. Skokov, J. D. Moore, and O. Gutfleisch, Nat. Mater. **11**, 620 (2012).
[123] T. Krenke, E. Duman, M. Acet, E. F. Wassermann, X. Moya, L. Mañosa, and A. Planes, Nat. Mater. **4**, 450 (2005).
[124] V. K. Pecharsky and K. A. Gschneidner, J. Appl. Phys. **86**, 565 (1999).
[125] K. A. Gschneidner and V. K. Pecharsky, Int. J. Refrig. **31**, 945 (2008).
[126] X. Moya, L. Mañosa, A. Planes, T. Krenke, E. Duman, M. Acet, and E. F. Wassermann, J. Magn. Magn. Mater. **316**, e572 (2007).

[127] L. Mañosa, X. Moya, A. Planes, T. Krenke, M. Acet, and E. F. Wassermann, Mater. Sci. Eng. A **481-482**, 49 (2008).
[128] B. Emre, S. Yüce, E. Stern-Taulats, A. Planes, S. Fabbrici, F. Albertini, and L. Mañosa, J. Appl. Phys. **113**, 213905 (2013).
[129] S. Chatterjee, S. Giri, S. Majumdar, and S. K. De, J. Phys. D. Appl. Phys. **42**, 065001 (2009).
[130] H. C. Xuan, P. D. Han, D. H. Wang, and Y. W. Du, J. Alloys Compd. **582**, 369 (2014).
[131] X. G. Zhao, M. Tong, C. W. Shih, B. Li, W. C. Chang, W. Liu, and Z. D. Zhang, J. Appl. Phys. **113**, 17A913 (2013).
[132] D. H. Wang, C. L. Zhang, H. C. Xuan, Z. D. Han, J. R. Zhang, S. L. Tang, B. X. Gu, and Y. W. Du, J. Appl. Phys. **102**, 013909 (2007).
[133] L. H. Yang, H. Zhang, F. X. Hu, J. R. Sun, L. Q. Pan, and B. G. Shen, J. Alloys Compd. **588**, 46 (2014).
[134] W.-H. Wang, J.-L. Chen, Z. Liu, G.-H. Wu, and W.-S. Zhan, Phys. Rev. B **65**, 012416 (2001).
[135] J. Marcos, L. Mañosa, A. Planes, F. Casanova, X. Batlle, and A. Labarta, Phys. Rev. B **68**, 094401 (2003).
[136] W. Ito, K. Ito, R. Y. Umetsu, R. Kainuma, K. Koyama, K. Watanabe, A. Fujita, K. Oikawa, K. Ishida, and T. Kanomata, Appl. Phys. Lett. **92**, 021908 (2008).
[137] V. Sharma, M. Chattopadhyay, and S. Roy, Phys. Rev. B **76**, 3 (2007).
[138] J. S. Amaral and V. S. Amaral, Appl. Phys. Lett. **94**, 042506 (2009).
[139] G. J. Liu, J. R. Sun, J. Shen, B. Gao, H. W. Zhang, F. X. Hu, and B. G. Shen, Appl. Phys. Lett. **90**, 032507 (2007).
[140] S. Das, J. S. Amaral, and V. S. Amaral, J. Phys. D. Appl. Phys. **43**, 152002 (2010).
[141] J. Du, Q. Zheng, W. J. Ren, W. J. Feng, X. G. Liu, and Z. D. Zhang, J. Phys. D. Appl. Phys. **40**, 5523 (2007).
[142] A. K. Nayak, K. G. Suresh, and A. K. Nigam, J. Phys. D. Appl. Phys. **42**, 035009 (2009).
[143] J. Nogués and I. K. Schuller, J. Magn. Magn. Mater. **192**, 203 (1999).
[144] W. H. Meiklejohn and C. P. Bean, Phys. Rev. **102**, 1413 (1956).
[145] S. Senoussi, J. Phys. **45**, 315 (1984).
[146] S. Agarwal, S. Banerjee, and P. K. Mukhopadhyay, **133904**, (2013).
[147] R. Singh, B. Ingale, L. K. Varga, V. V. Khovaylo, and R. Chatterjee, Phys. B Condens. Matter (2014).
[148] S. Chatterjee, S. Giri, S. K. De, and S. Majumdar, J. Phys. Conf. Ser. **200**, 032011 (2010).
[149] V. K. Pecharsky and K. A. Gschneidner, Jr., Phys. Rev. Lett. **78**, 4494 (1997).
[150] V. K. Pecharsky and K. A. Gschneidner, Appl. Phys. Lett. **70**, 3299 (1997).
[151] L. Ma, W. H. Wang, J. B. Lu, J. Q. Li, C. M. Zhen, D. L. Hou, and G. H. Wu, Appl. Phys. Lett. **99**, 182507 (2011).
[152] D. Y. Cong, S. Roth, J. Liu, Q. Luo, M. Pötschke, C. Hürrich, and L. Schultz, Appl. Phys. Lett. **96**, 112504 (2010).
[153] D. Y. Cong, Q. Luo, S. Roth, J. Liu, O. Gutfleisch, M. Pötschke, C. Hürrich, and L. Schultz, J. Magn. Magn. Mater. **323**, 2519 (2011).

[154] K. Manna, D. Samal, A. K. Bera, S. Elizabeth, S. M. Yusuf, and P. S. Anil Kumar, J. Phys. Condens. Matter **26**, 016002 (2014).

[155] G. V. Lecomte, H. V. Lohneysen, E. F. Wassermann, and H. v. Lohneysen, Zeitschrift Fur Phys. B Condens. Matter **50**, 239 (1983).

[156] J. Mydosh and T. Barrett, *Spin Glasses: An Experimental Introduction* (1993).

[157] K. Binder, Rev. Mod. Phys. **58**, 801 (1986).

[158] D. Kumar and A. Banerjee, J. Phys. Condens. Matter **25**, 216005 (2013).

[159] H. Vogel, Phys. Z **22**, 645 (1921).

[160] G. S. Fulcher, J. Am. Ceram. Soc. **8**, 789 (1925).

[161] A. Mauger, J. Ferré, M. Ayadi, and P. Nordblad, Phys. Rev. B **37**, 9022 (1988).

[162] J. Souletie and J. Tholence, Phys. Rev. B **32**, 516 (1985).

[163] D. Y. Cong, S. Roth, J. Liu, Q. Luo, M. Pötschke, C. Hürrich, and L. Schultz, Appl. Phys. Lett. **96**, 112504 (2010).

[164] C. Djurberg, P. Svedlindh, P. Nordblad, M. Hansen, F. Bødker, and S. Mørup, Phys. Rev. Lett. **79**, 5154 (1997).

[165] S. Fujiki and S. Katsura, Prog. Theor. Phys. **65**, 1130 (1981).

[166] Y. T. Wang, H. Y. Bai, M. X. Pan, D. Q. Zhao, and W. H. Wang, Phys. Rev. B **74**, 064422 (2006).

[167] J. R. L. de Almeida and D. J. Thouless, J. Phys. A. Math. Gen. **11**, 983 (1978).

[168] G. Toulouse, J. Phys. Lettres **41**, 447 (1980).

[169] M. Gabay and G. Toulouse, Phys. Rev. Lett. **47**, 201 (1981).

[170] J. Rajchenbach and N. Bontemps, J. Phys. Lettres **44**, 799 (1983).

[171] D. Fiorani, J. Tholence, and J. L. Dormann, J. Phys. C Solid State Phys. **19**, 5495 (1986).

[172] J. Dormann, D. Fiorani, and M. El Yamani, Phys. Lett. A **120**, 95 (1987).

[173] L. Wenger and J. Mydosh, Phys. Rev. B **29**, 4156 (1984).

[174] J. I. Pérez-Landazábal, V. Recarte, V. Sánchez-Alarcos, C. Gómez-Polo, and E. Cesari, Appl. Phys. Lett. **102**, 101908 (2013).

[175] H. Zheng, D. Wu, S. Xue, J. Frenzel, G. Eggeler, and Q. Zhai, Acta Mater. **59**, 5692 (2011).

[176] L. González-Legarreta, W. O. Rosa, J. García, M. Ipatov, M. Nazmunnahar, L. Escoda, J. J. Suñol, V. M. Prida, R. L. Sommer, J. González, M. Leoni, and B. Hernando, J. Alloys Compd. **582**, 588 (2014).

[177] R. L. Wang, L. S. Xu, H. B. Xiao, L. F. Xu, J. X. Zhang, R. J. Chen, S. Guo, and C. P. Yang, J. Appl. Phys. **113**, 17A936 (2013).

[178] L. Chen, F. X. Hu, J. Wang, J. L. Zhao, J. R. Sun, B. G. Shen, J. H. Yin, and L. Q. Pan, J. Phys. D. Appl. Phys. **44**, 085002 (2011).

[179] X. G. Zhao, C. C. Hsieh, J. H. Lai, X. J. Cheng, W. C. Chang, W. B. Cui, W. Liu, and Z. D. Zhang, Scr. Mater. **63**, 250 (2010).

[180] H. C. Xuan, Y. Deng, D. H. Wang, C. L. Zhang, Z. D. Han, and Y. W. Du, J. Phys. D. Appl. Phys. **41**, 215002 (2008).

[181] S. Agarwal and P. K. Mukhopadhyay, J. Alloys Compd. **608**, 329 (2014).

[182] W. Ito, M. Nagasako, R. Y. Umetsu, R. Kainuma, T. Kanomata, and K. Ishida, Appl. Phys. Lett. **93**, 232503 (2008).

[183] B. Zhang, X. X. Zhang, S. Y. Yu, J. L. Chen, Z. X. Cao, and G. H. Wu, Appl. Phys. Lett. **91**, 012510 (2007).

[184] V. Antonov, A. Perlov, P. Oppeneer, A. Yaresko, and S. Halilov, Phys. Rev. Lett. **77**, 5253 (1996).

[185] S. Banik, S. Singh, R. Rawat, P. K. Mukhopadhyay, B. L. Ahuja, A. M. Awasthi, S. R. Barman, and E. V. Sampathkumaran, J. Appl. Phys. **106**, 103919 (2009).

[186] S. Banik, R. Rawat, P. Mukhopadhyay, B. Ahuja, A. Chakrabarti, P. Paulose, S. Singh, A. Singh, D. Pandey, and S. Barman, Phys. Rev. B **77**, 224417 (2008).

[187] W. B. Pearson, *The Crystal Chemistry and Physics of Metals and Alloys* (Wiley-Interscience, 1972).